INFORMATION TO USERS

This manuscript has been reproduced from the microfilm master. UMI films the text directly from the original or copy submitted. Thus, some thesis and dissertation copies are in typewriter face, while others may be from any type of computer printer.

The quality of this reproduction is dependent upon the quality of the copy submitted. Broken or indistinct print, colored or poor quality illustrations and photographs, print bleedthrough, substandard margins, and improper alignment can adversely affect reproduction.

In the unlikely event that the author did not send UMI a complete manuscript and there are missing pages, these will be noted. Also, if unauthorized copyright material had to be removed, a note will indicate the deletion.

Oversize materials (e.g., maps, drawings, charts) are reproduced by sectioning the original, beginning at the upper left-hand corner and continuing from left to right in equal sections with small overlaps. Each original is also photographed in one exposure and is included in reduced form at the back of the book.

Photographs included in the original manuscript have been reproduced xerographically in this copy. Higher quality 6" x 9" black and white photographic prints are available for any photographs or illustrations appearing in this copy for an additional charge. Contact UMI directly to order.

UMI

A Bell & Howell Information Company
300 North Zeeb Road, Ann Arbor MI 48106-1346 USA
313/761-4700 800/521-0600

Reproduced with permission of the copyright owner. Further reproduction prohibited without permission.

Reproduced with permission of the copyright owner. Further reproduction prohibited without permission.

H

Defect identification using analysis of core-electrons contribution to Doppler broadening of the positron annihilation line and measurements of positron lifetime

by

Stanislaw Szpala

A dissertation submitted to the Graduate Faculty in Physics in partial fulfillment of the requirements for the degree of Doctor of Philosophy, The City University of New York

1999

Reproduced with permission of the copyright owner. Further reproduction prohibited without permission.

UMI Number: 9917703

Copyright 1999 by
Szpala, Stanislaw

All rights reserved.

UMI Microform 9917703
Copyright 1999, by UMI Company. All rights reserved.

This microform edition is protected against unauthorized
copying under Title 17, United States Code.

UMI
300 North Zeeb Road
Ann Arbor, MI 48103

Reproduced with permission of the copyright owner. Further reproduction prohibited without permission.

© 1999

STANISLAW SZPALA

All Rights Reserved

Reproduced with permission of the copyright owner. Further reproduction prohibited without permission.

This manuscript has been read and accepted for the Graduate Faculty in Physics in satisfaction of the dissertation requirements for the degree of Doctor of Philosophy.

1/22/99
Date

Leonard O. Roellig
Chair of Examining Committee

1/26/99
Date

Louis Celenza
Executive Officer

Marten L. denBoer

Martin Kramer

Kelvin G. Lynn

Myriam Sarachik

Frederick W. Smith
Supervisory Committee

THE CITY UNIVERSITY OF NEW YORK

Reproduced with permission of the copyright owner. Further reproduction prohibited without permission.

Abstract

Defect identification using analysis of core-electrons contribution to Doppler broadening of the positron annihilation line and measurements of positron lifetime

by

Stanislaw Szpala

Advisors: Professor Martin Kramer and Professor Leonard O. Roellig

Positron lifetime and Doppler broadening of the positron annihilation line are well recognized techniques capable of characterization of small open-volume defects (0.1 nm to 5 nm) in buried layers. Due to high level of background, the Doppler broadening measured with a single-detector setup contains information only on the dominating annihilation events, mostly the annihilation with the conduction and valence band electrons. The observability of the contribution of the core electrons to the annihilation can be enhanced upon reduction of the background obtained with the use of coincidence techniques. For the first time, the analysis of the contribution of the core electrons of various elements to the function describing the annihilation line was used to investigate the microstructure of foreign-atom decorated open volume defects. An antimony atom tied to a vacancy in the silicon lattice was identified as the acceptor-behaving defect responsible for the doping saturation in Sb-doped Si grown using low-temperature

Reproduced with permission of the copyright owner. Further reproduction prohibited without permission.

molecular beam epitaxy. The ground state of the DX center in Si-doped AlGaAs was shown to consist of a vacancy with one Si and one As atom at the nearest-neighbor sites. This is consistent with the theoretical model of the defect in which a small vacancy is formed by the shift of the Si atom away from the As atom.

A prototype of variable-energy positron lifetime spectrometer was built and tested. The timing resolution was characterized by FWHM of 470 ps. The new spectrometer was applied to characterize the defects in a novel material of low dielectric constant (methylsilsesquioxane custom-altered by IBM) intended to replace silicon dioxide in the integrated circuits of the next generation. Dielectric constant reducing voids of the radius of 1.4 nm were found in the foamed specimen in addition to the voids of the radius of 0.65 nm present in the base material.

Reproduced with permission of the copyright owner. Further reproduction prohibited without permission.

Acknowledgements

I would like to express appreciation to Prof. Kelvin G. Lynn for his superior guidance over my research towards the Ph.D. degree. Suggestions of Prof. Lynn allowed me to feel the beauty of the physics I was exploring. I would like to thank Dr. Csaba Szeles who introduced me to the magical word of experimentation with positrons and dedicated tremendous amount of time to answer my numerous questions. I am grateful to Prof. Leonard. O. Roellig, Prof. Kelvin G. Lynn, Dr. Thomas Gessmann, Dr. Marc Weber and Russel Tjossem for their detailed comments to this manuscript. I would like to thank Prof. Kelvin G. Lynn, Prof. Leonard Roellig and Prof. Marty Kramer for providing the financial support without which I would not be able to dedicate my time to research. I would like to thank Prof. Marty Kramer for encouraging me to hard work. Dr. P. Asoka-Kumar, Dr. Bent Nielsen, Dr. Fin Jacobsen are thanked for their time spent on the discussion of my data. J. P. Peng is thanked for performing the 2D-ACAR measurements and analysis of the voids in Si. Dr. Vinita Ghosh is thanked for her comments on the usage of the Vepfit program. Dr. M. Hakala is thanked for providing the theoretical calculations of the annihilation line shapes in Si divacancies. Dr. David Adler is thanked for his EXAFS measurements of Sb-doped Si samples. Dr. Mihail Petkov and Dr. Marc Weber are thanked for providing stimulating data of traditional Doppler broadening spectroscopy in low-k films and for many discussions on the research projects. Assistance of Prof. Gary Collins in developing the routine for fitting the lifetimes of positrons is greatly appreciated. Excellent craftsmanship of the crew of the Instrumentation Shop in Washington State Univ. (George Henry, Steve Watson, Doug Benson, Lauren Frei, Bill Alspach) is acknowledged for machining the parts used in the

Reproduced with permission of the copyright owner. Further reproduction prohibited without permission.

construction of the variable-energy positron beam and the lifetime spectrometer. Help of Harry Hacker and the employees of the Instrumentation Shop in Brookhaven National Laboratory is acknowledged for manufacturing the parts necessary in many experiments. My fellow students, Satoshi Hayakawa, Stefano Rassiga, Cesare Frecassi, Nemanja Krsmanovic, Russel Tjossem, Masahiro Seki, Yue Y. Shan are thanked for help in these jobs when two hands are not enough. I would like to thank Dr. Hans –J. Gossmann for supplying the samples of Sb-doped Si, Dr. O. W. Holland and Dr. Bent Nielsen for the samples containing Si divacancies, Dr. Kenneth Rodbell for the samples of low dielectric constant material. At last but not least, I would like to express appreciation to my parents and my sister Hanna for their loving, across-the-miles support.

Reproduced with permission of the copyright owner. Further reproduction prohibited without permission.

Preface

In spite of the development of numerous experimental techniques for defect identification in solids, positron annihilation spectroscopy (PAS) is one of a few which are capable of nondestructive characterization of open-volume defects of the size ranging from about 0.1 nm to 5 nm at the concentration from 10^{16} cm^{-3} to 10^{20} cm^{-3}. Good control of the sampling depth adds to the list of advantages of the method. From measurements of the Doppler broadening of the positron annihilation line, the integrated momentum density of the electrons in the solid at the positron-electron annihilation site may be obtained. The density of the momentum is determined by the overlap of the wave functions of the positron and the electrons. The distribution of the momentum constitutes a "finger print" of the defect at which the annihilation takes place. In a commonly used single-detector setup, the level of background is high and only the dominating annihilation events can be analyzed. These are mostly the annihilations with the valence and conduction electrons. Reduction of the background with a coincidence-detector allows investigating rare events of positron annihilation with the core electrons. The wave functions of the core electrons depend on the element and are independent on the neighborhood of the atom. Therefore, the information on the chemical vicinity of the positron at the open-volume defect is contained in the distribution of the momentum of the core electrons at the annihilation site. The annihilation of the positrons with neighborhood-independent core electrons contributes to the shape of the annihilation line and can be described by an element-specific function. A linear combination of these element-specific functions may be used to characterize the investigated defect. The coefficients of the linear combination reflect the fractions of positron annihilation with

Reproduced with permission of the copyright owner. Further reproduction prohibited without permission.

the electrons of the given elements. This extended analysis was not possible in a single-detector spectrometer due to insufficient domain of the function describing the annihilation line.

This method was, for the first time, applied to characterize foreign-atom decorated open-volume defects. A technologically important issue of the doping saturation in Sb-doped Si, grown with low-temperature molecular beam epitaxy, was researched. The complex of a vacancy tied to an Sb atom was identified as the acceptor-behaving defect preventing the increase of the concentration of the electrons in the conduction band over 7×10^{20} cm^{-3}. The analysis of the DX center in Si-doped AlGaAs revealed the existence of a small vacancy with one Si and one As atom at the nearest-neighbor sites in the ground configuration of the defect. These results are consistent with the theoretical model describing the defect as a vacancy created by a shift of the Si atom away from the As atom.

Positron lifetime is another aspect of PAS. The technique is based on the fact that the positron annihilation lifetime depends on the density of momentum of the electrons at the annihilation site. The density depends on the size of the open-volume defect trapping the positron. Therefore, quantitative information on the size of the defects can be extracted. Although positron lifetime spectrometers are quite common, most of them are not sensitive to defects in shallow films. A prototype design of a depth-resolved positron lifetime spectrometer was constructed and tested. The timing resolution of 470 ps at full width at half maximum (FWHM) was obtained.

The new lifetime spectrometer was employed in characterization of a novel material intended to replace silicon dioxide in the integrated circuits of the next

Reproduced with permission of the copyright owner. Further reproduction prohibited without permission.

generation. A new dielectric of a lower dielectric constant k is actively being searched. Porous materials with a low value of k due to the presence of air trapped in the pores, are considered. In this research, methylsilsesquioxane was investigated. The base material was shown to contain voids of the radius of 0.65 nm. Additional, k-reducing pores were created during the foaming process and their radius was found to be 1.4 nm.

The measurements described in section 2 were performed on the positron beam in Brookhaven National Laboratory (BNL), NY. The lifetime spectrometer was attached to the positron beam in Washington State University, WA, which was a rebuilt and modified version of the beam from BNL.

The highlights of the thesis are as follows: After the introduction (section 1), Doppler broadening spectroscopy is reviewed with emphasis put on the core-electrons contribution to the annihilation line (section 2.1). Elemental specificity of the annihilation line is given in section 2.2. The overlap of the positron and the core-electrons wave functions is analyzed in undecorated open-volume defects in Si and selected metals (section 2.3). The identification of the acceptor-behaving defect in Sb-doped Si is presented in section 2.5.2. Section 2.5.3 is dedicated to the analysis of the chemical composition of the DX center in Si-doped AlGaAs. The construction and applications of the prototype variable-energy positron lifetime spectrometer are described in section 3. Motivation to the construction of the spectrometer is sketched in section 3.1, the current status of positron lifetime spectrometers is reviewed in section 3.3 and physics behind the design of the prototype spectrometer is described in section 3.4. The design is described in section 3.5.1.1. The simulation of the performance of the lifetime spectrometer is presented in sections 3.5.1.3 and 3.5.1.4. The actual functioning of the spectrometer was

Reproduced with permission of the copyright owner. Further reproduction prohibited without permission.

tested on undecorated open-volume defects in Si (section 3.5.1.5). The results of the investigation of the low-*k* material are given in section 3.5.1.6. The research projects are summarized in section 4.

Reproduced with permission of the copyright owner. Further reproduction prohibited without permission.

Table of Contents

Abstract....iv

Acknowledgements....vi

Preface....viii

List of Tables....xv

List of Figures....xvi

1 Introduction....1

2 Doppler broadening of the positron annihilation line....5

2.1 Introduction....5

2.1.1 Reduced-background Doppler-broadening spectroscopy of positron annihilation radiation....13

2.2 Elemental specificity....17

2.3 Undecorated open-volume defects....21

2.3.1 Si....21

2.3.1.1 Samples....22

2.3.1.2 Characterization....23

2.3.2 Other materials....29

2.4 Influence of the surface....31

2.5 Defects related to foreign atoms....34

2.5.1 Moderately-doped Si....34

2.5.2 LT-MBE Si doped with Sb....35

2.5.2.1 Motivation....35

2.5.2.2 Samples....39

Reproduced with permission of the copyright owner. Further reproduction prohibited without permission.

2.5.2.3 Characterization 40

2.5.3 DX centers in Si-doped AlGaAs 50

2.5.3.1 Motivation 50

2.5.3.2 Characterization 54

2.6 Advantages and disadvantages of the method 59

3 Construction and applications of a prototype positron-lifetime spectrometer on a variable-energy positron beam 62

3.1 Motivation 62

3.2 Positron lifetime spectrometers - introduction 65

3.3 Review of existing lifetime setups 66

3.3.1 "Bulk" lifetime techniques 67

3.3.1.1 Gamma-gamma coincidence 67

3.3.1.2 Positron-gamma coincidence 69

3.3.2 Variable-energy beams 69

3.3.2.1 Secondary-electron triggered setup #1 70

3.3.2.2 Secondary-electron triggered setup #2 71

3.3.2.3 Pulsed beams 73

3.4 Physical background of the design of the positron lifetime spectrometer 75

3.4.1 Processes stimulated by positrons hitting specimen 75

3.4.2 Secondary electron emission 77

3.4.2.1 Consequences of the nature of secondary electrons 77

3.4.2.2 Emission of secondary electrons induced by positrons - theory and experiment 78

Reproduced with permission of the copyright owner. Further reproduction prohibited without permission.

3.4.3 Backscattered positrons 83

3.5 The designs of the present work 88

3.5.1 Design #1, ExB deflector type 88

3.5.1.1 Description of the system 88

3.5.1.2 Experimental 91

3.5.1.3 Influence of the spread of the time of flight of secondary electrons on the time resolution: simulations and experiment 94

3.5.1.4 Background effects due to backscattered positrons: simulation and experiment 99

3.5.1.5 System test: positron lifetime in defect-free and defective Si 105

3.5.1.5.1 Brief review of selected published works on positron lifetime in Si 105

3.5.1.5.2 Analysis 106

3.5.1.6 Application to low-k dielectric films 112

3.5.1.6.1 Motivation 112

3.5.1.6.2 Characterization 114

3.5.1.7 Discussion 119

3.5.2 Design #2, magnetic-dipole trap 119

3.5.2.1 Description of the system 119

3.5.2.2 Testing 120

4 Summary 124

Bibliography 125

Reproduced with permission of the copyright owner. Further reproduction prohibited without permission.

List of Tables

Table I. Results of the fitting of the ratio curves of Sb-doped Si films 43

Table II. Results of the fitting of the ratio curves of the DX center in Si-doped AlGaAs.57

Table III. The total yield of the secondary electrons 80

Table IV. Fitted lifetimes of defects in Si... 109

Table V. Parameters of the instrumental resolution of the lifetime spectrometer 110

Table VI. Countrate in the lifetime spectrometer 112

Table VII. Lifetime components found in low-k films... 116

Reproduced with permission of the copyright owner. Further reproduction prohibited without permission.

List of Figures

Figure 1. Comparison of selected defect-characterization techniques........................ 2

Figure 2. Annihilation line shape.. 8

Figure 3. S and W parameters.. 10

Figure 4. Simulated positron implantation profiles in Al..................................... 12

Figure 5. Doppler broadening setup.. 14

Figure 6. Schematic of a reduce-background Doppler broadening spectrometer......... 16

Figure 7. Annihilation line shapes and ratio curves as signatures of defects.............. 19

Figure 8. Ratio curves of undecorated open-volume defects in Si.......................... 24

Figure 9. S parameter vs. positron implantation energy in undecorated open volume defects in Si.. 25

Figure 10. Theoretical and experimental ratio curve of Si divacancy........................ 28

Figure 11. Pure open-volume defects in selected metals.. 30

Figure 12. Ratio curves of Si surfaces... 32

Figure 13. Ratio curves of moderately-doped Si... 35

Figure 14. Saturation of the doping in LT-MBE Si... 37

Figure 15. Ratio curves of Sb-doped Si for various dopant concentrations............... 40

Figure 16. Anticipated chemical components of the defects in Sb-doped Si.............. 41

Figure 17. Transition of the DX center in Si-doped AlGaAs between the ground and metastable configuration.. 51

Figure 18. Position of the DX level in the band structure for various mole fractions x in Si-doped $Al_xGa_{1-x}As$... 52

Figure 19. Effect of light illumination on DX center in Si-doped and

Reproduced with permission of the copyright owner. Further reproduction prohibited without permission.

undoped AlGaAs.. 55

Figure 20. Chemical contributors to the ratio curves of DX center in AlGaAs........... 56

Figure 21. Fit of the relaxed-sustitutional transition in DX center in AlGaAs............ 58

Figure 22. Decay scheme of ^{22}Na.. 67

Figure 23. A typical "bulk" lifetime spectrometer.. 68

Figure 24. Secondary-electron triggered positron lifetime spectrometer #1............... 70

Figure 25. Lifetime spectrometer with channel plates with a hole......................... 72

Figure 26. Diagram of a secondary-electron triggered positron lifetime spectrometer... 76

Figure 27. Yield of secondary electrons for various incident energies..................... 81

Figure 28. Energy distribution of secondary electrons....................................... 82

Figure 29. Total yield of backscattered positrons for various targets...................... 84

Figure 30. Energy distribution of positrons backscattered from gold...................... 86

Figure 31. Dependence of the energy spectrum of backscattered electrons on the target.. 87

Figure 32. Schematic of E×B based positron lifetime spectrometer......................... 89

Figure 33. Electronic part of the positron lifetime spectrometer............................ 94

Figure 34. Simulated and fitted resolution function in the lifetime spectrometer......... 96

Figure 35. Simulation of the landing spot of positrons backscattered onto the sample... 98

Figure 36. Simulated and experimental background in the lifetime spectrometer...... 101

Figure 37. Simulation of the time-position correlation for backscattered positrons..... 103

Figure 38. Reduction of background of backscattered positrons with a gamma shield. 105

Figure 39. Experimental lifetime spectra of defect-free Si, Si divacancy and Si void.. 107

Reproduced with permission of the copyright owner. Further reproduction prohibited without permission.

Figure 40. Molecular structure of methylsilsequioxane..................................... 113

Figure 41. Lifetime spectra of low-k porous films... 115

Figure 42. Magnetic-dipole trap positron lifetime spectrometer.......................... 120

Figure 43. Lifetime spectrum obtained with magnetic-dipole trap spectrometer........ 122

Reproduced with permission of the copyright owner. Further reproduction prohibited without permission.

1 Introduction:

Invention of the transistor in 1947 by Bardeen and Brattain initiated the semiconducting industry. It was soon realized that replacement of vacuum tubes with transistors could lead to a dramatic miniaturization of complex devices as well as reduction of the power necessary to make them running. Portable radio receivers appeared and several years later work on first microcomputers began. The first transistors were quite large by today's standards, several millimeters long. They were slow and unreliable. Further progress was limited by not sufficient knowledge of the properties of semiconducting materials used for the construction of the devices. Defect characterization became the main issue for semiconducting industry. Many techniques have been developed for this purpose, including electrical methods (resistivity and Hall effect measurements), optical (light absorption, photoluminescence and x-ray diffraction) or nuclear (nuclear magnetic resonance and nuclear reaction analysis). Each of the techniques has its advantages and disadvantages. Areas of expertise for several techniques are shown in Figure 1. When it comes to the detection of negatively charged or neutral subnanometer open volume defects in the concentrations ranging between 10^{16} cm^{-3} and 10^{20} cm^{-3}, positron annihilation spectroscopy is one of the best methods. Over the years positron annihilation spectroscopy (PAS) has been used in numerous applications. Examples include determination of the cause limiting the thickness of single-crystalline layer grown by means of molecular beam epitaxy[1] and study of metal-oxide-semiconductor structures.[2]

Reproduced with permission of the copyright owner. Further reproduction prohibited without permission.

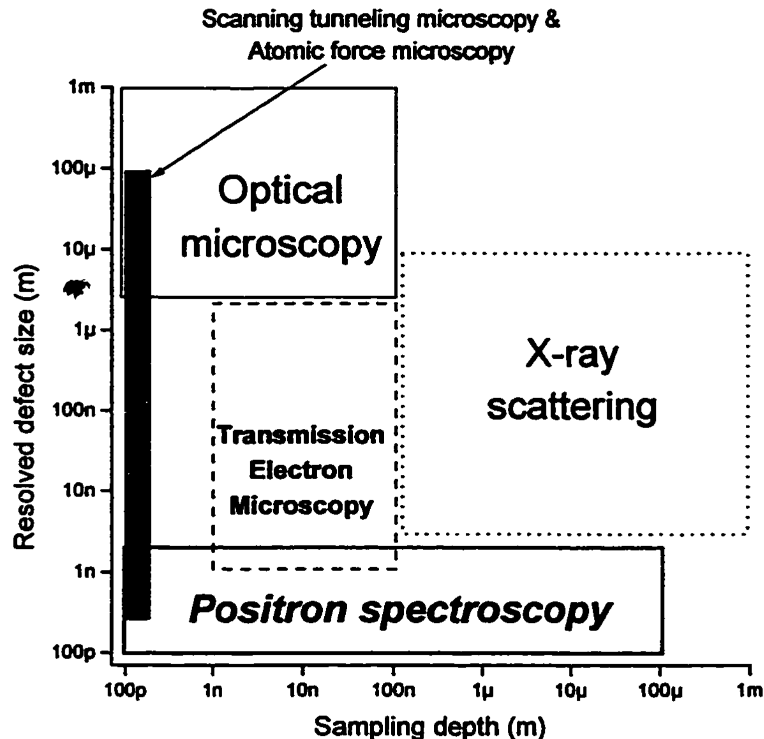

Figure 1. Resolved defect size vs. sampling depth in selected defect-characterization techniques.

PAS relies on the collection of information from positron-electron annihilation events.[3] Although positrons live indefinitely in vacuum, in solids they annihilate with electrons. In the absence of other particles, each annihilation event produces at least two gamma rays. The probability of the production of two gamma rays is the highest and goes down with the number of emitted gammas. The energy of the rays is determined by the principles of conservation of momentum and energy. In the center of mass frame, for the two-gamma process, energy of each gamma is equal 511 keV, corresponding to the rest mass of electron or positron. In the lab frame, the energy of each gamma is shifted by the amount proportional to the momentum of the electron-positron pair. This is called

Reproduced with permission of the copyright owner. Further reproduction prohibited without permission.

Doppler shift. The positrons implanted into the solids quickly thermalize. At the instant of the annihilation, the positron momentum is small compared to the momentum of the electrons and its contribution to the momentum of the electron-positron pair can be neglected. Consequently, the Doppler shift is proportional to the momentum of the annihilating electron. Therefore, the analysis of the distribution of energy of gamma rays can provide information about momentum distribution of electrons at the positron-electron annihilation site. This aspect of PAS is called Doppler broadening of positron annihilation radiation.

As determined by conservation of momentum and energy, the angle between emitted gamma rays depends on the momentum of electron-positron pair. These angles can by measured through precise positioning of the gamma detectors with respect to the sample. Using detector arrays and collecting many annihilation gamma rays, it is possible to obtain two-dimensional maps of the density of momentum of electrons in the specimen. Such maps can be used as "finger prints" of defects. This technique is referred as two-dimensional angular correlation radiation (2D-ACAR).

A positron trapped at an open-volume defect does not annihilate immediately. The delay depends on the size of the open volume as well as on the kind of atoms decorating the vacancy. This is because the annihilation rate is proportional to the overlap of the electron and positron wavefunctions. Analysis of the lifetime of positrons in the sample provides a convenient way of defect identification.

Other aspects of PAS can be identified, like positronium formation or the centroid shift of the annihilation line, which is dependent on the binding energy of the electron-

Reproduced with permission of the copyright owner. Further reproduction prohibited without permission.

positron pair. Nevertheless, Doppler broadening, 2D-ACAR and lifetime are the most commonly used.

All PAS techniques require positrons. The simplest way of providing them is from a naturally decaying source, usually ^{22}Na isotope. The energy of the emitted positrons varies from zero to several hundred keV. Because the positron penetration depth depends on its energy, the positrons penetrate the sample from the surface up to tens of microns deep. Therefore, the average properties of a layer extending from the surface of the specimen up to a few tens of microns are investigated. This is a cost-effective solution and works well in some cases. When depth resolution is required, variable-energy monoenergetic positrons are needed. Through a proper adjustment of the implantation energy, a layer buried at a well-defined distance from the surface may be analyzed. Apparatus used for this purpose is called a variable-energy positron beam. Positrons can be supplied in two ways. From a radioactive source or from electron-positron pair production from x-rays emitted during deceleration of electrons in high-energy accelerators. The energy spectrum of these positrons is very broad, up to several hundred keV. To obtain a monoenergetic source of positrons, the positrons are moderated to single eV energies and accelerated in electric field to well-defined energies. Variable-energy positron beams are rather complex systems and quite expensive. Nevertheless, the amount of information obtained in experiments justifies the expense.

Reproduced with permission of the copyright owner. Further reproduction prohibited without permission.

2 Doppler broadening of the positron annihilation line

This chapter is dedicated to applications of a modified positron annihilation spectrometer measuring the Doppler broadening of the positron-electron annihilation line.

2.1 Introduction

In vacuum positrons live indefinitely, however, this is not the case of positrons placed in a solid. Matter and antimatter cannot coexist in proximity. Within a short time, the positron annihilates with an electron from the solid, producing gamma rays. Emission of two gamma rays is the most probable channel of reaction. If the electron and the positron were at rest at the instant of the annihilation, the gamma rays would be emitted in the opposite directions and each gamma would carry the energy equal $m_e c^2 - E_B / 2$, where E_B is the binding energy of the electron and positron pair, m_e is the electron rest mass and c is the speed of light. The movement of the electron-positron pair causes the gamma energies to shift. The relativistic change of the energy of a photon caused by the movement of the source follows:

$$E_{listener} = \frac{c + \upsilon_{listener}}{c + \upsilon_{source}} E_{source}, \tag{1}$$

where $\upsilon_{source} = p_z / (2m_e)$ and p_z is the projection of the momentum of the electron-positron pair onto the gamma ray direction. Because the momentum of the positron at the instant of the annihilation is small compared to the momentum of the electrons, p_z is, approximately, the projection of the momentum of the annihilating electron. For

Reproduced with permission of the copyright owner. Further reproduction prohibited without permission.

stationary detectors $\upsilon_{listener} = 0$. Therefore, after expanding into the Taylor series around $\upsilon_{source} = 0$, the energy of each gamma ray is approximately:

$$E_{\gamma} = m_e c^2 - \frac{1}{2} E_B \pm \frac{1}{2} p_z c, \tag{2}$$

The energy of one gamma ray is red-shifted while of the other – blue-shifted. This phenomenon is similar to the energy shifts of acoustic waves investigated by Doppler and hereafter will be termed as Doppler shift. The shift of the energy of the gamma ray depends on the momentum of the electron-positron pair. This momentum is determined by the properties of the medium in which the annihilation takes place. Consequently, one can obtain information about the medium through monitoring the energy of the annihilation photons.

Measurement of the Doppler shift of a single annihilation ray is of little use because the electrons in the medium do not have well defined momentum. Instead, the momenta follow a distribution. To reconstruct this distribution one may measure the Doppler shift for a large number of events. Following equation 2, the intensity vs. gamma energy is equal the density of the momentum of electron-positron pairs, p, integrated over the transverse momentum:

$$I(E_{\gamma}) = I(p_z) = \int\int \rho(\bar{p}) dp_x dp_y, \tag{3}$$

The momentum density, $\rho(p)$, can be expressed as the square of the Fourier transform of the electron-positron two-particle wave function. In the independent-particle scheme,

Reproduced with permission of the copyright owner. Further reproduction prohibited without permission.

$$\rho(\bar{p}) = \pi r_e^2 c \sum_i \left| \int d\bar{r} e^{i\bar{p}\bar{r}} \Psi_+(\bar{r}) \Psi_-(\bar{r}) \sqrt{\gamma_i(\bar{r})} \right|^2 , \tag{4}$$

where Ψ_+ and Ψ_- are the positron and electron wave functions, respectively, γ_i is the enhancement factor taking into account the pileup of the electrons at the positron site and r_e is the classical electron radius. The contribution from all electronic shells, *i*, are summed. In solids, positrons reside as delocalized particles or become trapped at open-volume defects. The corresponding wave functions differ substantially. Delocalized positrons can be described as Bloch wave functions, while positrons trapped at defects have localized wave functions. These variations between the positron wave functions induce changes in the corresponding momentum densities and the annihilation line shapes, $I(E_\gamma)$. This phenomenon, together with variations of electron wave functions, is the ground principle of defect identification in Doppler broadening of positron annihilation line shape spectroscopy.

The relation described by equation 3 can by measured experimentally using a high-purity Ge detector. In a real experiment, $I(E_\gamma)$ is a peak-like function centered at 511 keV – ½ E_B. If the electron and positron were stationary at the annihilation site, the Dirac delta could be used to describe the function. Due to non-zero momentum of the particles, the peak is broadened by the Doppler shift of the gamma-ray energy, see equation 2. In a solid, positrons predominantly annihilate with the outer electrons, i.e. from the valence and conduction bands. Since these electrons carry little momentum, less than 5×10^{-3} m_ec, their contribution is observed near the centroid of the peak. There is a non-negligible overlap of the positron and core electrons wavefunctions. The momentum of the core

Reproduced with permission of the copyright owner. Further reproduction prohibited without permission.

electrons is higher, i.e. between 5×10^{-3} m_ec and 50×10^{-3} m_ec. Their share to the annihilation line shows up in the tails of the line, see Figure 2.

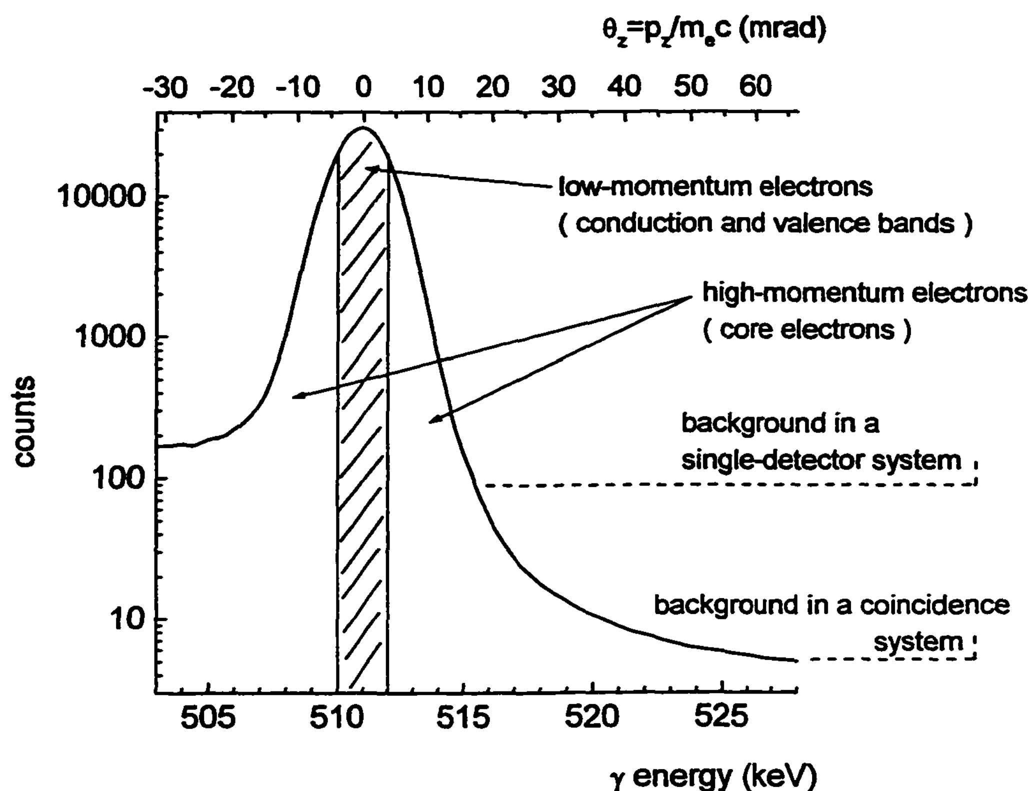

Figure 2. Typical shape of the annihilation line. The γ energy is related to the momentum of electron-positron pair, p_z, as given in equation 2. θ_z is a measure of the momentum of the electron-positron pairs in the units of m_ec and is often used in literature ($\theta_z = p_z / m_ec$). The actual line shape of Si with voids was used, with the total of 1×10^7 counts. Typical levels of background are indicated.

There has been a considerable interest in theoretical calculations of the line shape. In 1979 Lynn *et al* calculated the contribution of the core electrons to the annihilation line in aluminum target.[4] Excellent agreement with experimental data was obtained within independent-particle model for momentum values over 19.5×10^{-3} m_ec. In 1995

Reproduced with permission of the copyright owner. Further reproduction prohibited without permission.

Alatalo *et al* calculated the enhancement factor $\gamma_i(r)$ to take into account the short-range electron pileup at the positron.[5] Free-atom electronic wave functions were used and the positron wave functions were calculated within the linear-muffin-tin orbital method. The authors derived core-electron contribution to the annihilation line for several important semiconductors, including: Si, GaAs, InP. The study was not limited to perfect crystals. Selected open-volume defects were considered, e.g. P and In vacancy InP. The calculations agree very well with the experimentally found tails of the line shapes. Similar calculations, for several undecorated open volume defects and vacancy-oxygen defects, were performed by Kuriplach *et el.*[6] Relaxation of atoms surrounding the open volume containing a trapped positron was taken into account. In 1998, Hakala *et al* added the contribution of the valence electrons to the annihilation line.[7] Agreement between theory and experiment for bulk Si for momentum ranging from 0 to 40×10^{-3} m_ec is outstanding. Calculations for vacancy clusters in Si are included, too. This is probably the most complete calculation of positron annihilation line shape in Si and Si containing subnanometer vacancy clusters published so far.

The research on the core-electron contribution to annihilation radiation presented in this chapter has been published.[8] Several months later other papers on the subject were published. Asoka-Kumar rebuilt the two-detector Doppler broadening spectrometer previously described by Lynn *et al.*[9,4] It allowed the authors to analyze elemental specificity of positron annihilation line shapes at momentum values extending up to $40\text{x}10^{-3}$ m_ec.[10] Myler and Simpson used semi-empirical analysis to correlate the line shapes with the periodic table of the elements.[11] Alatalo *et al* continued his work on the calculations of the core-electron contribution to the annihilation line shape.[12]

Reproduced with permission of the copyright owner. Further reproduction prohibited without permission.

In the early days of applications of the Doppler broadening spectroscopy of positron annihilation spectroscopy, large amounts of background prevented physicists from analyzing the full shape of the annihilation line. To obtain quantitative information, integral parameters of the line were introduced. The most commonly used were the S and W parameters, as defined in Figure 3. The S parameter is the ratio of the counts in the centroid area to all counts in the peak. The W parameter denotes the ratio of the counts in

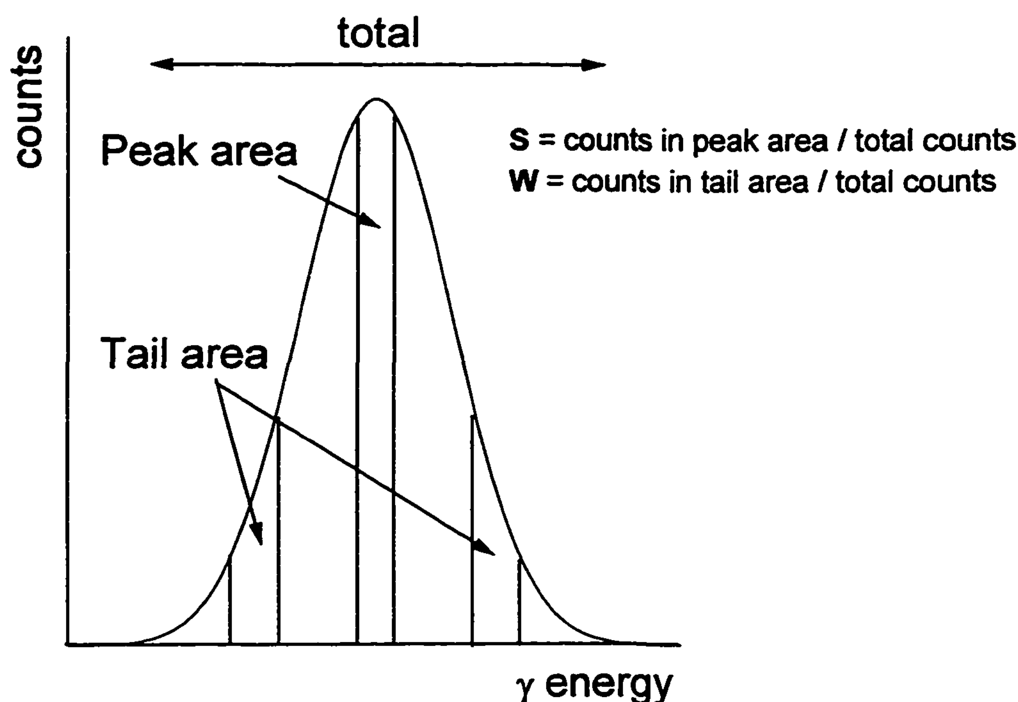

Figure 3. The line shape integral parameters are defined as the ratio of counts in the peak or tail area to all counts for S and W parameters, respectively. The choice of the integration limits is arbitrary.

the tail of the line to the total counts in the peak. The choice of the counts-integration limits is arbitrary and is usually optimized to get maximum sensitivity to changes in the

Reproduced with permission of the copyright owner. Further reproduction prohibited without permission.

investigated line shape. In the construction of the S parameter, the counts for low values of the electron-positron momentum are integrated. Therefore, the S parameter is sensitive to the contribution of conduction and valence electrons. The W parameter, on the other hand, emphasizes variations in the core-electron annihilation. Integral-type parameters are commonly used instead of other parameters such as FWHM, because they are additive. Additivity is a very convenient property because it lets one consider each additive parameter as a linear combination of defect-specific parameters. This feature allows one to extract the concentrations of the defects in the sample.

Recently, Dannefaer *et al* derived the values of the S and W parameters for selected defect-free semiconductors.[13] The authors tied the density of valence electrons to the momentum corresponding to the Fermi energy, which is approximately inversely proportional to the S parameter. Using fractions of core-electron to valence-electron annihilation rates calculated elsewhere, theoretical values fairly close to experimental ones were found.

Analysis of the line shape function, with emphasis on the tails, was a part of my Ph.D. research and will be presented in the following sections.

In order to use PAS to investigate defects in buried layers in solids, it is necessary to place probing positrons into the specimen. This is usually accomplished by shooting positrons of well-defined energy into the sample. A positron beam is used to do this. A positron in a solid undergoes a series of inelastic and elastic collisions. It quickly looses its kinetic energy and thermalizes. The distance from the surface where the positron stops, depends on its initial energy. The higher the energy, the deeper it goes on average. The stopping process was investigated experimentally through monitoring the fraction of

Reproduced with permission of the copyright owner. Further reproduction prohibited without permission.

positrons leaving a thin foil.[14] Extensive Monte Carlo simulations showed that the

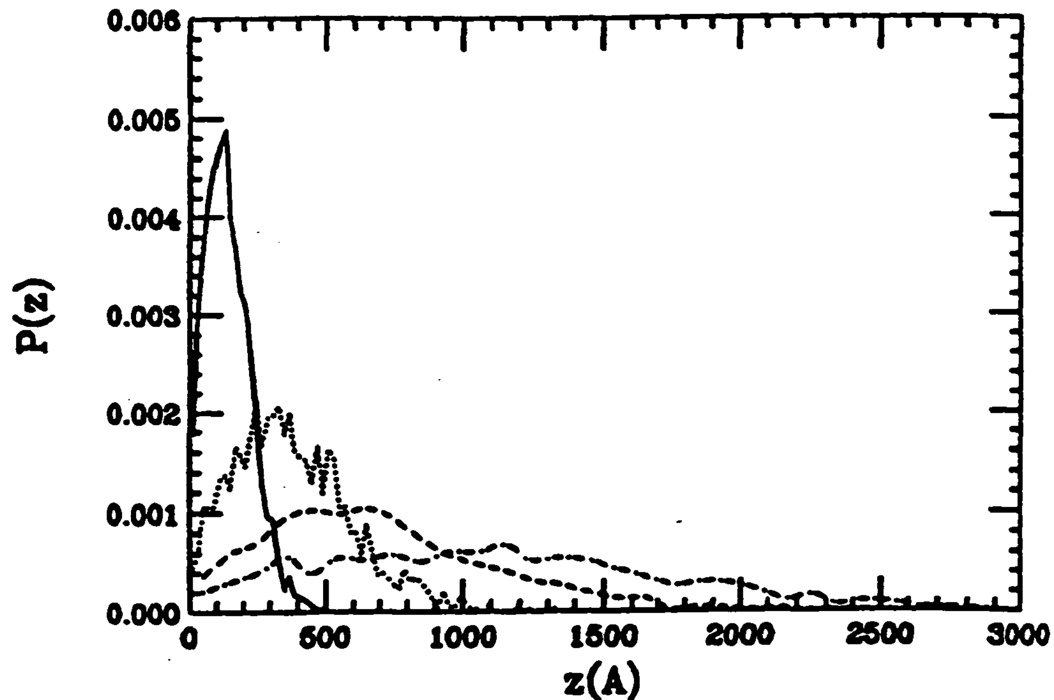

Figure 4. Implantation profiles in aluminum calculated by Ghosh *et al* using the Monte Carlo scheme.[15] Solid, dotted, dashed and dot-dashed lines denote positron implantation energies of 1 keV, 2 keV, 3 keV and 4 keV, respectively.

stopping profile[15], as a function of the penetration depth z, can be described using a Makhovian distribution:

$$P(z) = N_0 m \frac{z^{m-1}}{z_0^{\ m}} e^{-\left(z/z_0\right)^m}, \tag{5}$$

where N_0 is the normalization constant, m is an adjustable parameter and z_0 = $\langle z \rangle / \Gamma(1+1/m)$. $\Gamma()$ is the special function gamma. Mean penetration depth $\langle z \rangle$ is defined as:

Reproduced with permission of the copyright owner. Further reproduction prohibited without permission.

$$\langle z \rangle = \frac{A}{\rho} E^n, \tag{6}$$

where ρ is the density, A and n are adjustable parameters. Examples of implantation profiles are plotted in Figure 4. Further motion of the positrons obeys the equation of diffusion. The diffusion process depends on the concentration of the positron trapping defects. Hence, analysis of the Doppler broadening of positron annihilation line for various implantation energies[16] provides an effective way of extracting defect-concentration profiles.[1]

2.1.1 Reduced-background Doppler-broadening spectroscopy of positron annihilation radiation

Experimental measurements of Doppler broadening of the positron annihilation line, as described by equations 2 through 4, require use of a gamma detector with excellent energy resolution (FWHM below about 2 keV). For this reason and because of their high efficiency, high-purity germanium detectors are commonly used. Good detectors of this type are characterized by FWHM about 1.5 keV for 511 keV gamma rays. This is sufficient to observe some variations in the contribution of valence and conduction electrons to the annihilation line. It is customarily obtained through analysis of the S parameter defined in section 2.1. The W parameter can also be defined to extract the integrated contribution of core electrons to the annihilation. A typical setup is shown in Figure 5. The amplitude of the pulse from the germanium detector is proportional to the gamma energy. A spectroscopy amplifier is used to shape the signal. The amplitude of each pulse is converted to digital form using an analog to digital converter (ADC).

Reproduced with permission of the copyright owner. Further reproduction prohibited without permission.

Counts as a function of amplitude are then stored in the memory of a multi-channel analyzer (MCA).

Although this setup has been used by scientists for years, it is far from perfect. The level of background is large enough to shade all but a tiny fraction of the contribution of core electrons to the tails of the annihilation line. The background counts

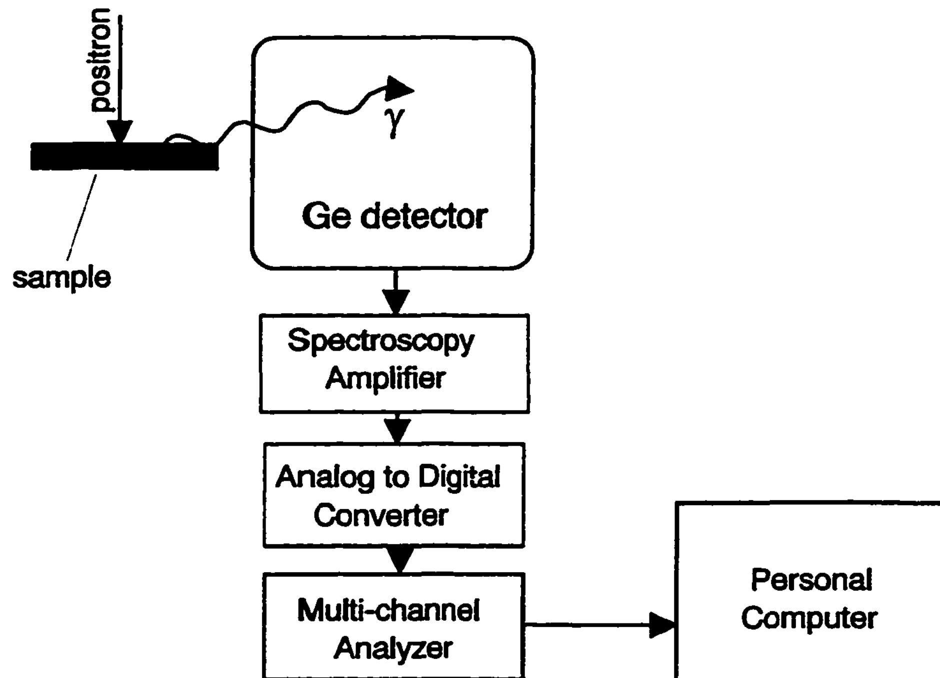

Figure 5. A typical setup used in the measurements of the Doppler broadening of the annihilation line.

are caused by the gamma rays produced by the radioactive source of positrons and by natural ambient radiation, and by pulse pile up events. The first two problems can be fixed with the aid of another gamma detector responding to the other annihilation gamma. Exclusive detection of the gamma rays accompanied by the other quanta allows substantial decreasing of the level of background. Counts from natural background are lonesome and do not qualify. The gamma rays from the positron annihilation inside the source are excluded as well. Both annihilation rays are emitted in the opposite directions

Reproduced with permission of the copyright owner. Further reproduction prohibited without permission.

and cannot be simultaneously recorded by the two detectors unless the annihilation takes place between the detectors. This is not the case for the majority of positron beams, where the positron source is located a meter or more from the sample. This method was successfully tested by Lynn and Goland in 1976.[17] Conveniently, the two annihilation rays are emitted almost colinearily and the deviation does not exceed 2 degrees. It allows placing the other detector on the opposite side of the sample. In this case, the count-rate loss is limited only by the efficiency of the second detector. The setup used in the experiments described in the next sections of chapter 2 was based on this design. The schematic of the system used is shown in Figure 6. A high-efficiency BiGeO (BGO) scintillator coupled to a photomultiplier tube (PMT) was used as the second detector. Timing relationship of the pulses recorded in the two detectors was analyzed in a time to amplitude converter (TAC). When the pulses were separated by no more than 70 ns, they were considered to originate from the same annihilation event and were accepted. Counts found in only one detector were ignored. The logical function was implemented through gating the ADC.

Occasionally, a gamma ray would enter the germanium detector before the detector completed the charge collection corresponding to the previous gamma. This undesirable event is called pulse pile-up. The charge collected as a result of the detection of two gamma rays is summed yielding a pulse of a higher amplitude. Such a pulse cannot be distinguished from an event corresponding to positron annihilation with high-momentum electron. To prevent pulse pile-up, the positron beam was gated. After a successful detection of a pulse, a blocking signal was applied to the E×B energy selector[18] mounted in the source chamber of the beam. The blocking signal was

Reproduced with permission of the copyright owner. Further reproduction prohibited without permission.

preventing the arrival of positrons to the target before the signal of the germanium detector would be restored to equilibrium level. The duration of the blocking signal was selected to be 20 μs. This procedure is advantageous over standard pile-up rejection (PUR) systems used in nuclear instrumentation modules. It makes it possible to discard

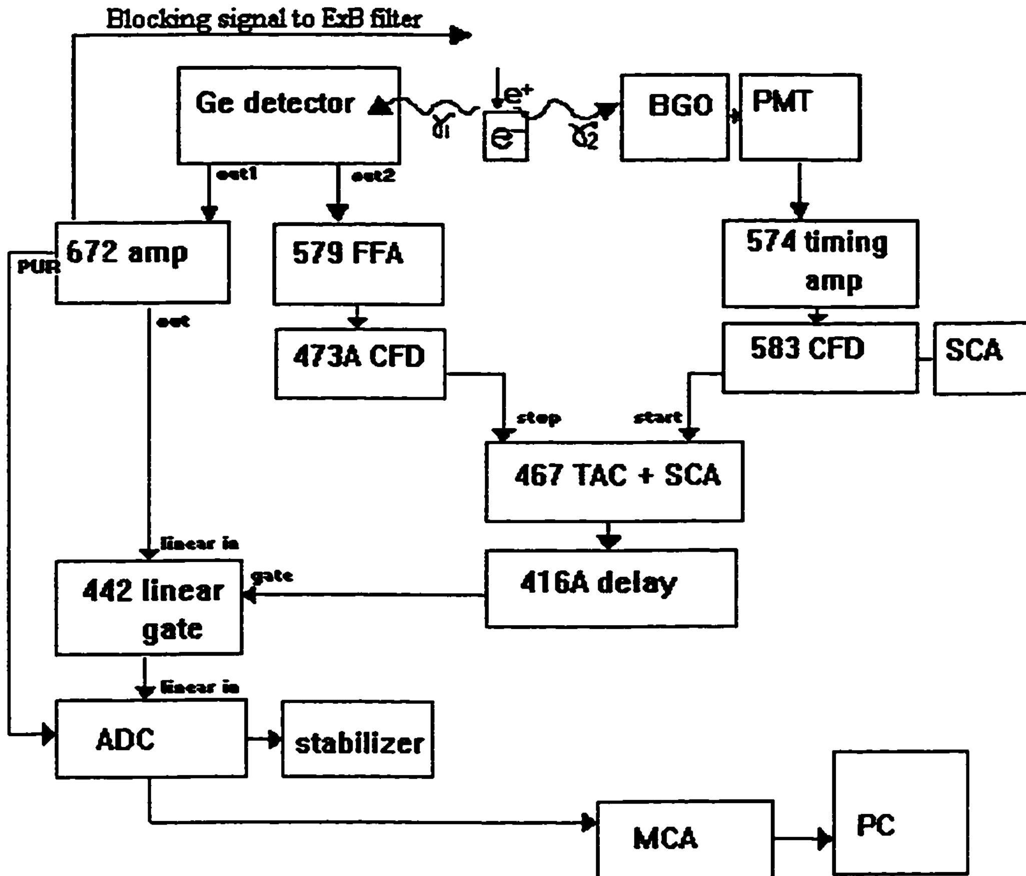

Figure 6. Reduced-background Doppler broadening spectrometer used in our experiments. γ_1 is used for the energy-resolved analysis. The pulse is accepted only when the second annihilation ray, γ_2, is detected within the acceptance-time interval.

the counts corresponding to a positron almost immediately following another one. The natural limitation of the method comes from the non-zero time of flight of a positron

Reproduced with permission of the copyright owner. Further reproduction prohibited without permission.

from E×B selector to the target. This kind of gating cannot stop positrons, which already passed the gating device. The method also eliminates permanent detector dead time caused by the generation of a continuous PUR signal.

Further reduction of pulse pile-up is possible with the aid of two germanium detectors. It turns out that two-dimensional mapping of the gamma-energy counts of the two detectors makes it possible to separate pile-up events from legitimate counts. Two germanium detector system was proposed and tested by Lynn *et al*,[4] however, this system was not used in this research.

2.2 Elemental specificity

Examples of annihilation line shapes of selected elements are shown in Figure 7(a). These are line shapes of defect-free specimens, as seen by positrons. The data was collected using reduced-background Doppler-broadening spectrometer described in section 2.1.1. Only the right side of the peak is depicted. This is done for two reasons: First, to eliminate the high level of background for gamma energies below 511 keV. Such background is an intrinsic feature of the detector and is caused by incomplete charge collection (see Figure 2). Incomplete charge collection does not contribute counts when $E_\gamma > 511$ keV. Second, part of the plot for energies below 511 keV contains counts corresponding to three-photon decay of positronium. Separation of these positronium counts from annihilation with high-momentum electrons is possible when only 511 keV and higher gamma energies are considered.

The useful range of interest of the momentum of electrons corresponds to gamma energies between 511 keV and 520 keV. Count-rate within this range varies by over three

Reproduced with permission of the copyright owner. Further reproduction prohibited without permission.

orders of magnitude. To emphasize small changes, it is convenient to scale the line-shape plots. Counts for each gamma energy are divided by the counts at the same gamma energy of a reference line shape. Hereafter, these kind of plots are termed as "ratio curves".[19] The choice of the reference line shape is arbitrary and the investigated line shape may produce drastically different ratio curves depending on the choice of the reference line shape. The choice of defect-free specimen is often convenient. This is because a unity line denotes a defect-free sample while any deviations from this line indicate a defective specimen. Prior to the division, counts in each line shape are normalized to the same integral value. In Figure 7(b) the ratio curves corresponding to the line shapes from Figure 7(a) are plotted. The counts are normalized to the total area extending from 505.12 keV to 516.77 keV. In order to show that the plots differ not only by amplitude but also by the shape, the ratio curves from Figure 7(b) were scaled to get the same amplitude of the main peak. The scaled ratio curves are plotted in Figure 7(c). Because investigation of defects in Si is a major part of this research, the line shape of high-quality float-zone (FZ) Si is used as the reference line shape. Hereafter, this specimen is called "defect-free" Si (as seen by positrons).

A smoothing routine was applied to Figure 7 and all subsequent ratio curves. It turned out to be necessary in order to investigate variations for gamma energies above 514 keV. The statistical error bars at these energies are large. To reduce the error bars, counts from the adjacent channels were averaged. The number of the channels used for the averaging was selected so that the error bars of the summed counts would not exceed 3%. A new data point was placed at the gamma energy calculated as the centroid of the channels taken for the averaging. As the gamma energy increases, so does the number of

Reproduced with permission of the copyright owner. Further reproduction prohibited without permission.

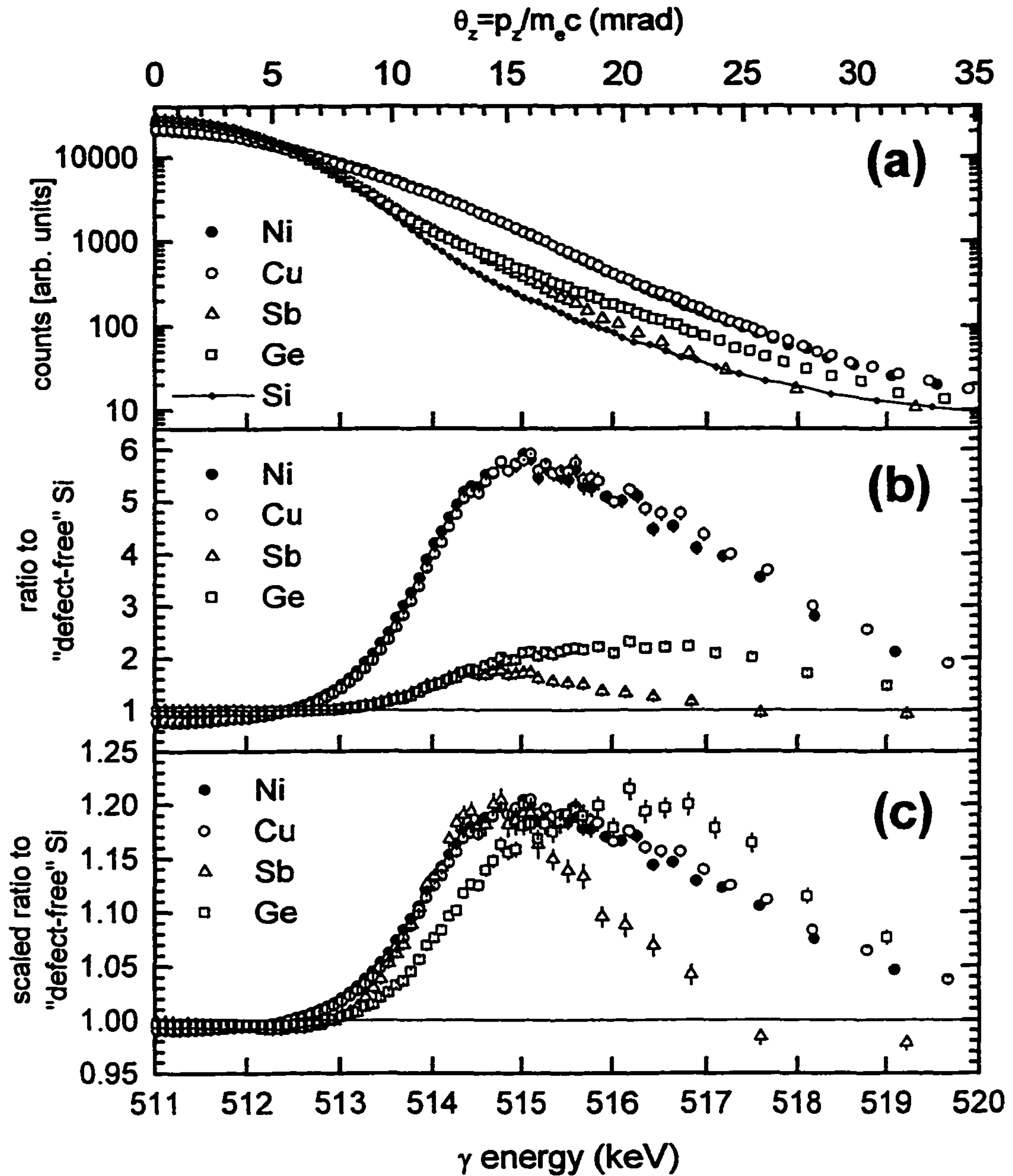

Figure 7. The annihilation line shape constitutes a signature of an element (a). To emphasize small variations at high values of E_γ, the plots can be presented as "ratio curves" (b), see text. To show the variations of the shape of the ratio curves, the plots can be scaled to have the same amplitude of the main peak (c). A smoothing routine was applied here and in subsequent figures.

Reproduced with permission of the copyright owner. Further reproduction prohibited without permission.

the averaged channels. This results in the apparent reduction of the density of the experimental points in the plot. The enlarged spacing between the points on the abscissa reflects the statistical errors of the counts on the ordinate. The routine will be termed as "variable-averaging", hereafter. Application of this smoothing routine hides subtle changes in the plot. It is advantageous over fixed-number-of-channels averaging because it performs averaging only when necessary, i.e. when the statistical error bars are too large. The variable-averaging routine, just like any averaging algorithm, can improve data presentation only when statistical errors dominate. It does not help when the systematic errors exceed the statistical ones. This is the case of the data points for gamma energy above about 520 keV. Above 520 keV, the background in the annihilation line shapes begins to exceed the rightful counts. At high values of the gamma energies, the plots of the ratio curves falsely converge to a constant value. The plots of the line shapes themselves also suffer from the background problems. When gamma energy is close to or above 520 keV, the variations between the plots are decreased. The background problem might be substantially reduced through a numerical deconvolution with an effective background function.[20,21] The reliability of the variable-averaging routine was tested by comparison to high-statistics data. A total of 1.5×10^7 counts were collected. The corresponding high-statistics ratio curve was compared to the plot constructed when only 2×10^6 counts had been collected and variable-energy algorithm applied. Agreement turned out to be excellent for $E_\gamma < 517$ keV (not shown).

Analysis of the line shapes and the corresponding ratio curves from Figure 7 indicates that this technique is very sensitive to the elemental specificity. Unfortunately,

Reproduced with permission of the copyright owner. Further reproduction prohibited without permission.

when the distribution of the momentum of the core electrons in samples is similar, the same is true for the ratio curves. This is the case of Cu and Ni, differing only in the configuration of conduction and valence electrons. These electrons carry little momentum and this method of data presentation is not appropriate. Other ways of data presentation, like difference spectra, could be useful. Different aspects of positron annihilation radiation, e.g. 2D-ACAR, might be applied too. Nevertheless, as demonstrated in the following sections, core analysis of the Doppler broadening can be successfully used in numerous applications.

2.3 Undecorated open-volume defects

2.3.1 Si

Positrons are well known for their ability of being trapped and annihilating in negatively-charged and neutral open-volume defects. Upon trapping, the wave function of a positron becomes localized in the open volume of the defect. In a specimen free of open-volume defects trapping positron, the positron wave function can be described as a delocalized Bloch state. The overlap of the positron wave function with the wave functions of the electrons of the neighboring-atoms is different in the two cases. According to equations 4 and 5, these variations are reflected in the shape of the annihilation line. Due to spatial localization of a trapped positron, its wave function rapidly decreases with the distance from the trap center. The wave function of a core electron, on average, decreases with the distance from the nucleus. Because the center of the positron trap is offset from the nucleus of the atoms, the overlap of these wave functions is small. On the other hand, delocalized Bloch functions of non-trapped

Reproduced with permission of the copyright owner. Further reproduction prohibited without permission.

positrons can penetrate atoms of the medium. The overlap of the Bloch positron and core electrons is measurable. The variations in the overlap of the wave functions are reflected in the changes of the shape of the annihilation line. Because core electrons carry high momentum, the decrease of the annihilation rate with core electrons for localized positrons transforms into lowering of the tails of the line. Since every non-escaping positron in a solid eventually annihilates, annihilation with low-momentum conduction and valence electrons becomes more dominant. Consequently, the annihilation line turns narrower. The exact nature of the change of the shape of the annihilation line depends on the contribution of atomic shells to annihilation. This contribution for various open-volume defects will be discussed next.

2.3.1.1 Samples

Several undecorated open-volume defects in Si were investigated. This includes divacancy, voids of various sizes and amorphous Si. Monovacancies were not examined due to technical difficulties. They anneal out well below room temperature. Transport of the sample from the vacancy-creating system to the positron facility would have been cumbersome.

Si divacancies were produced using high-energy Si ion irradiation. Irradiation with Si ions was selected in order to avoid binding the newly created vacancies with the foreign atoms. The defects were created in Czochralski-grown Si(100) at room temperature. Si ions of the energy of 5 MeV were irradiated to the total dose of 8×10^{13} cm^{-2}. By examining the annealing behavior of irradiated samples, Holland *et al* showed that irradiation at these conditions produces Si divacancies.[22] Larger open-volume defects do not form at these conditions. In addition, the defect was cataloged by the value of the

Reproduced with permission of the copyright owner. Further reproduction prohibited without permission.

S parameter equal 1.04, well established for Si divacancy.[23] The possibility of decoration of the divacancies with oxygen was ruled out by showing same value of S-parameter in float-zone and Czochralski-grown samples. Only the later method is known to introduce oxygen into silicon.

Si films with voids were found in low-temperature molecular-beam epitaxy (LT-MBE) layers. It is known that during epitaxial process, a single-crystalline layer is grown only up to a critical layer thickness, h_{epi}.[24] Further growth produces a highly defective layer. Such layers were previously investigated with transmission electron microscopy (TEM),[25] where voids of the size of several nm were found.

2.3.1.2 Characterization

Experimental ratio curves for selected undecorated open-volume defects in Si are shown in Figure 8. Divacancy, voids of different sizes and amorphous Si are plotted. To construct the ratio curves, high-purity FZ Si(111) was selected as the reference line shape. The spectrum was measured at high positron kinetic energies, i.e. from 20 to 40 keV. At these high energies, positrons penetrate Si up to about 4 μm. Because the positron diffusion length in Si is equal to 200 nm, positrons cannot diffuse back to the surface. Therefore, the reference spectrum can be considered free of the surface contribution.

The dependence of the S parameter on the positron implantation energy was measured for all tested samples in order to determine the best positron-implantation energies for the determination of the ratio curves. The plots are shown in Figure 9. The S parameter of Si divacancy is almost flat for positron kinetic energies between 12 keV to 20 keV. The flatness suggests that positrons of these energies do not diffuse to the

Reproduced with permission of the copyright owner. Further reproduction prohibited without permission.

surface. The measured value of the S parameter in the investigated range of positron energies is equal to 1.04. S = 1.04 is a well-established theoretical and experimental value for Si divacancy.[23] Therefore, it is justifiable to say that these positrons become trapped at the divacancies and annihilate there. Alternatively, the positrons could annihilate from

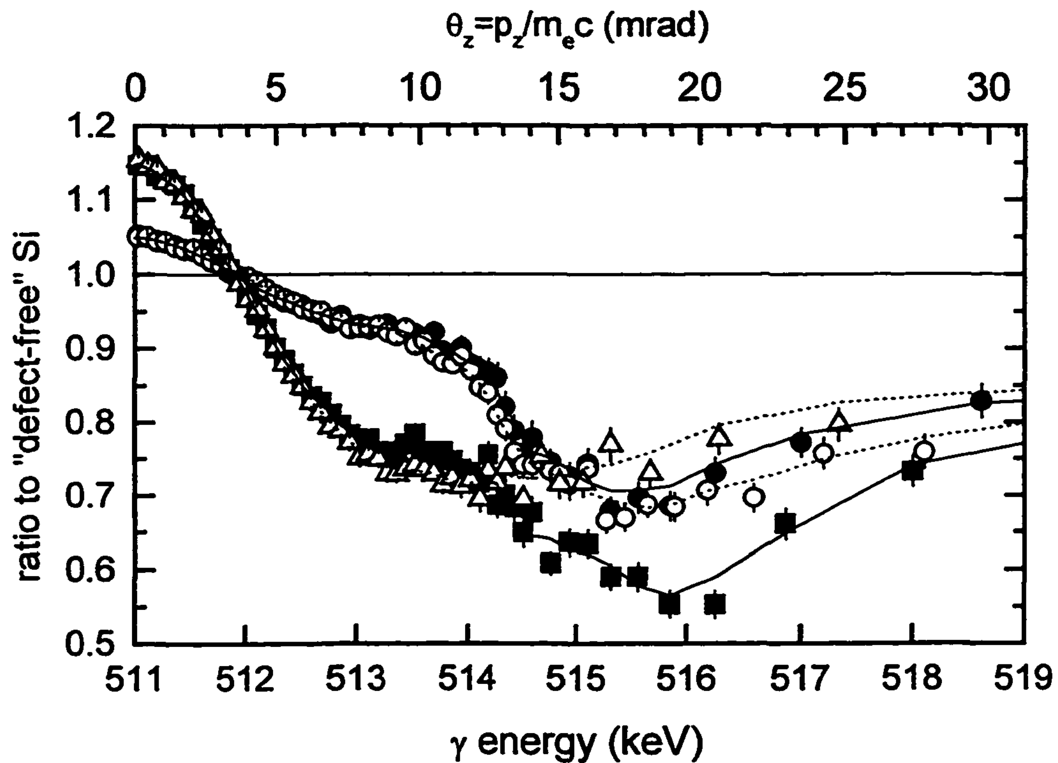

Figure 8. Ratio curves of undecorated open-volume defects in Si. Solid circles denote divacancy, open circles – amorphous Si, solid squares – void #1 (S = 1.09), open triangles – void #2 (S=1.11). The curve of void #2 contains the contribution of the annihilation from delocalized Bloch states. The lines serve as a guide for the eye only. The curves are referenced to defect-free Si. The ratio curves were calculated from the line shapes averaged for the positron implantation energies indicated in Figure 9.

delocalized Bloch states. This would influence the ratio curve.

Reproduced with permission of the copyright owner. Further reproduction prohibited without permission.

Two samples containing voids were analyzed. Void #1 was characterized by the S parameter equal 1.09. Its ratio curve was constructed for positron energies between 3 keV and 3.6 keV. The S parameter of void #2 was found 1.11. Positron energies from 5.4 keV to 6.6 keV were selected for the ratio curve. It was suspected that not all positrons in these samples were trapped in the voids. Some e^+ could annihilate from delocalized

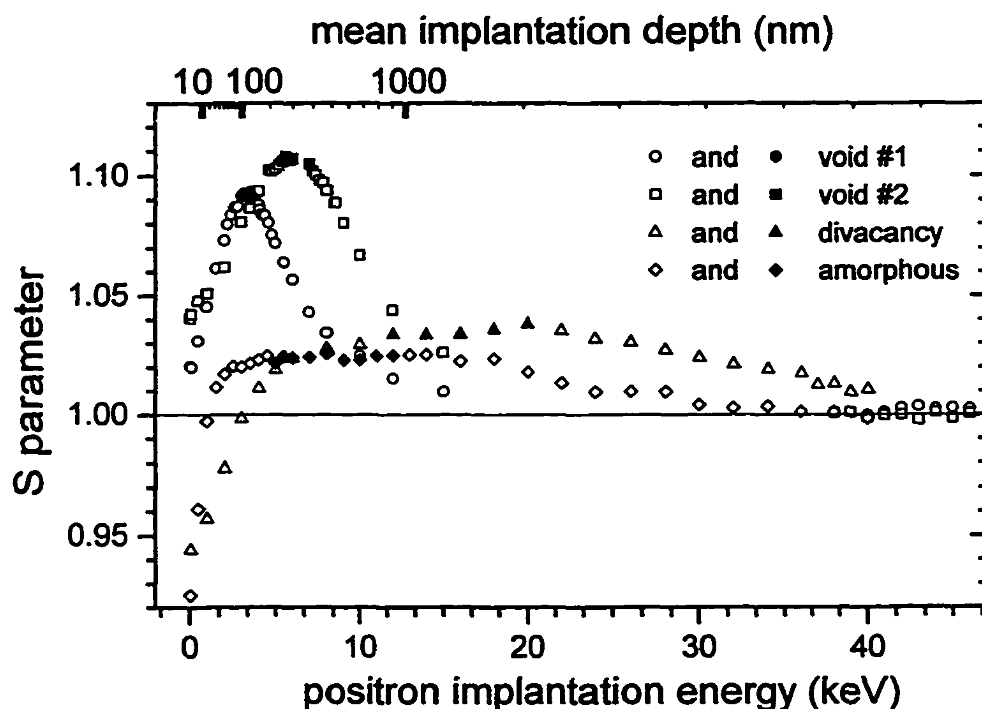

Figure 9. The S parameter vs. positron implantation energy in undecorated open-volume defects in Si. Mean positron implantation energy is shown. The S parameter was normalized so that S=1 denotes defect-free Si. The data points used in the construction of the ratio curves in Figure 8 are shown as solid symbols.

Bloch states. The corresponding ratio curves would have to be corrected according to the partial annihilation rates in the defects and from delocalized states:

Reproduced with permission of the copyright owner. Further reproduction prohibited without permission.

$$\frac{\text{"}\mathit{pure\ defect}\text{"}}{\text{"}\mathit{defect-free}\text{"}} = \frac{1}{b}\left(\frac{\text{"}\mathit{meased\ defect}\text{"}}{\text{"}\mathit{defect-free}\text{"}} - a\right), \tag{7}$$

where a and b denote the annihilation fractions corresponding to positrons that are delocalized and localized at defects, respectively. Since the characteristic value of the S parameter of voids varies depending on the size of the void, the dilemma could not be resolved from Doppler-broadening measurements only. Positron lifetime measurements could be helpful. Presence of 220 ps or shorter decay, the characteristic value in defect-free Si, would indicate positron annihilation from Bloch states. A reduction of the 220 ps lifetime would be expected due to positron trapping in the voids. A longer, several ns, lifetime component would be expected for the positrons annihilating in the voids. The corresponding partial annihilation rates for each channel of reaction could be extracted from fractional intensities of the characteristic lifetimes. Alternatively, similar information may be obtained from 2D-ACAR measurements. My colleague from Brookhaven National Laboratory, J. P. Peng, performed 2D-ACAR measurements and analysis. The 2D-ACAR spectrum in p_x and p_y momentum space contained two components (not shown). The first one was the well-known spectrum of delocalized positrons in single-crystalline, defect-free silicon. The second was the spectrum of a void. The spectrum of defect-free Si was gradually subtracted from the spectrum of the investigated sample until the characteristic features of the defect-free Si disappeared. The amount of the spectrum that was left corresponded to the fraction of positrons annihilating in defect-free Si. Peng performed the procedure for the sample with voids #1. He found that 13±2 % of the annihilation events corresponded to delocalilzed positrons and 87±2 % to the annihilation in the voids. The ratio curve shown in Figure 8

Reproduced with permission of the copyright owner. Further reproduction prohibited without permission.

was corrected according to equation 7 to remove the effect of the annihilation of nonlocalized positrons. The experimental ratio curve of Si divacancy exhibits a minimum at E_γ = 515.5 keV and a minimum-like change of the slope around 513 keV. The minimum and the minimum-like change of the slope indicate the reduction of the annihilation with the high-momentum core electrons. The value is elevated around 511 keV, i.e. around the centroid of the line shape. The elevated values reflect the characteristic value of the S parameter exceeding the unity (S=1.04 for Si divacancy). The theoretical ratio curve of Si divacancy, together with replotted experimental one, is shown in Figure 10. The theoretical curve is based on the data obtained from Hakala,[7] mentioned in section 2.1. The theoretical data of all three crystallographic directions, i.e. [100], [110] and [111], was averaged. In the experimental setup that was used, the gamma detector was quite large (the outer diameter of the crystal was 6 cm) and it was placed close to the sample (the front face of the detector was placed about 2.5 cm from the center of the sample). Therefore, the annihilation gamma rays emitted within a rather large solid angle were detected. No single crystallographic direction could be distinguished. Averaging of the directions was found the most appropriate procedure. The theoretical annihilation line shape was convoluted with a Gaussian (FWHM = 1.57 keV) to account for the instrumental resolution of the system used in the experimental setup. The agreement between the experimental ratio curve and the theoretical one is fair. The minimum-like change of the slope around 513.5 keV is seen in both the theory and experiment. The simulation underestimates the contribution of the high-momentum core electrons at the divacancy for $E_\gamma > 515.5$ keV. Nevertheless, the trend of the reduction of the core-electron annihilation is similar. The small inconsistency between the theory and

Reproduced with permission of the copyright owner. Further reproduction prohibited without permission.

experiment may also be explained by approximations used in the calculations. Ions surrounding the vacancy were not relaxed from their ideal lattice positions. In a more sophisticated scheme, relaxation of the ion positions due to missing atoms and the presence of a positron should be included.

The ratio curves of void #1 and void #2 look fairly similar to each other for gamma energies up to 514 keV. They differ from the divacancy spectrum. The plot of the

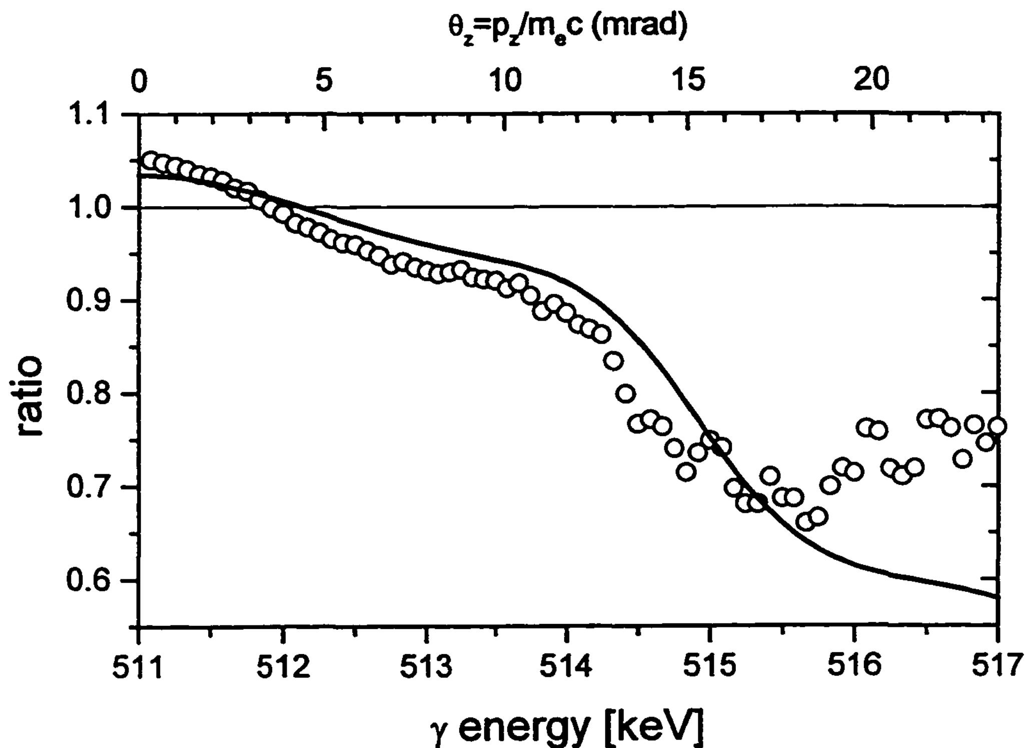

Figure 10. Theoretical (line) and experimental (circles) ratio curves of Si divacancy referenced to defect-free Si.

voids cannot be generated by simple scaling of the divacancy spectrum. The reduction of the core-annihilation is more pronounced in the voids. This is because the average distance between the positron and the core electrons is larger in voids. Consequently, the

Reproduced with permission of the copyright owner. Further reproduction prohibited without permission.

overlap of the wave functions is smaller. From the experimental point of view, the clear distinction between the ratio curves of voids and divacancies indicates a possibility of determining the size of the open volume through the inspection of the ratio curve. For undecorated open volumes, size cataloging could be done using the analysis of the S parameter only, provided the experimental setup is well characterized. Nevertheless, full study of the ratio curve can be much more powerful in the case of foreign-atom decorated open-volume defects.

Surprisingly, the ratio curve of amorphous Si looks similar to the one of Si divacancy. No theoretical calculations on this issue were found.

2.3.2 Other materials

Open-volume defects in materials other than Si were also investigated. The research included undecorated vacancy-like defects in aluminum, copper and antimony. Vacancy in Al were measured in 99.999% pure Al foil at 500 ^{0}C. Vacancies are believed to be a precursor of the melting process. Therefore, heating the specimen to the temperature close to the melting point should generate vacancies.[19] The vacancies disappear as soon as the temperature is lowered. Vacancies in copper were created by pulsed ion-beam melting and subsequent resolidification. Vacancy-like defects were obtained from Sb lumps obtained directly from the manufacturer (Alfa-Aesar[26]) and are growth-process specific. The defects were annealed out at 500 ^{0}C, equal approximately 80 % of the melting point.

The experimental ratio curves for the defects in Al, Cu and Sb are plotted in Figure 11. The corresponding defect-free specimen was selected as the reference specimen during the construction of the ratio curves, e.g. defect-free Al for Al defects.

Reproduced with permission of the copyright owner. Further reproduction prohibited without permission.

All three plots exhibit a reduction of the contribution of the high-momentum electrons (E_γ > 513 keV) compared to the defect-free specimen. The defect free specimen would be represented as a unity line. This is similar to undecorated open-volume defects in Si. It is consistent with the picture of diminished contribution of the core electrons to annihilation. The shape of the ratio curve of vacancies in aluminum closely resembles the one of Si divacancy. It can be explained by the identical core-electron configuration of Al

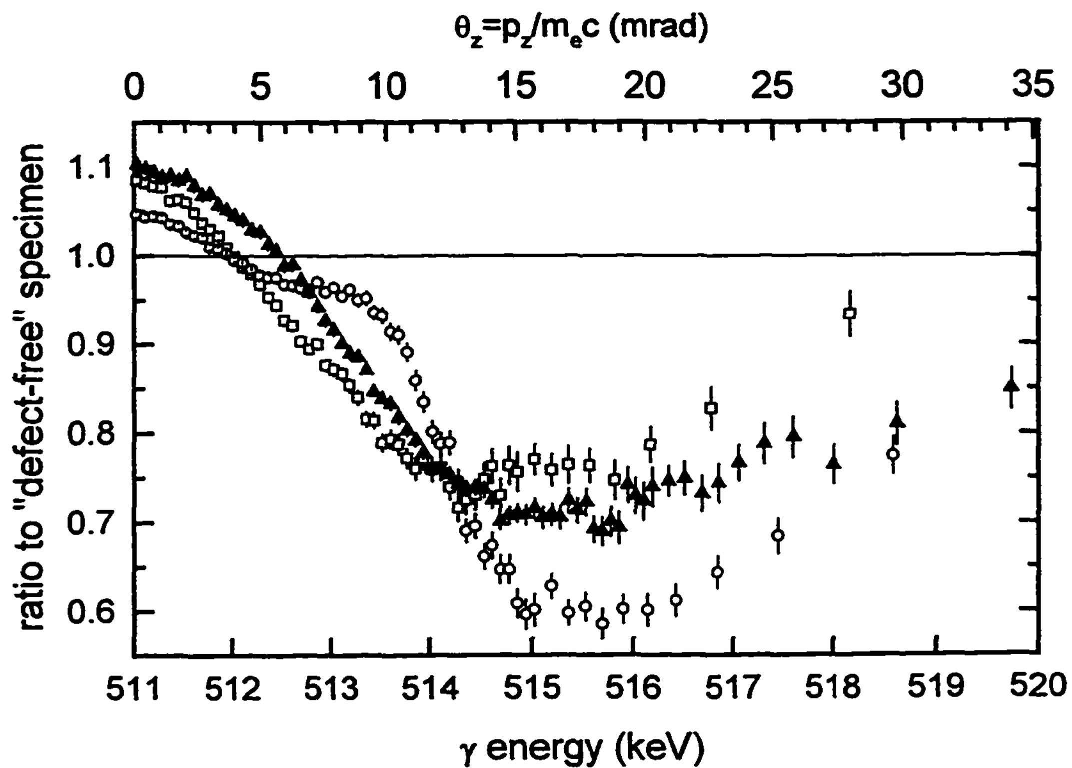

Figure 11. Pure open-volume defects in aluminum (open circles), antimony (open squares) and copper (solid triangles). The corresponding defect-free specimen was used as the reference line shape.

and Si. The core-electron configurations of copper and antimony are different than of silicon. The variations of the corresponding ratio curves of the defective specimen are a

Reproduced with permission of the copyright owner. Further reproduction prohibited without permission.

reflection of this fact. Similar reductions in the annihilation with core electrons are anticipated to be a general feature observed in undecorated open-volume defects.

2.4 Influence of the surface

Surface characterization is an important aspect of material research. Various techniques have been developed specifically for this purpose. Among most important are low-energy electron diffraction (LEED), Auger electron spectroscopy and recently invented scanning tunneling microscopy (STM). Some aspects of positron annihilation spectroscopy contribute to this field, too. Positron annihilation induced Auger electron emission is a powerful tool in surface research.[27] Due to positronium formation at surfaces, analysis of its annihilation may be used as a separate technique. In this research, however, characterization of buried layers was the objective. Positron annihilation at the surface was not specifically studied in this work. Nevertheless, the effect of positron annihilation at surfaces needs to be addressed: Supplying positrons with the energy of at least a few hundred eV allows them to pass through the surface. In spite of this, when the positron diffusion length is comparable to the positron implantation depth, the positrons may diffuse to the surface and annihilate there. The contribution of the positrons annihilating at the surface is reflected in the shape of the annihilation line and, consequently, in the ratio curves.

Like most materials, silicon oxidizes in air. Under normal condition several nanometer-thick oxide layer grows spontaneously on the Si surface. This layer can be removed through etching in aqueous hydrofluoric acid, followed by rinsing in water.[28,29] It has been established that during this process Si dangling bonds get terminated with

Reproduced with permission of the copyright owner. Further reproduction prohibited without permission.

hydrogen and hydroxide.[30] The oxide starts growing back within less than an hour, so the sample needs to be placed under vacuum immediately after the etching.[31]

To establish the surface contribution to positron annihilation in silicon, low-energy (below 100 eV) positrons were injected into the samples. Two Si(111) samples were examined. One was covered with the native oxide, while the other had the oxide removed through etching in HF acid. The corresponding ratio curves are shown in Figure 12. The curves were normalized to the line shape of positrons annihilating from

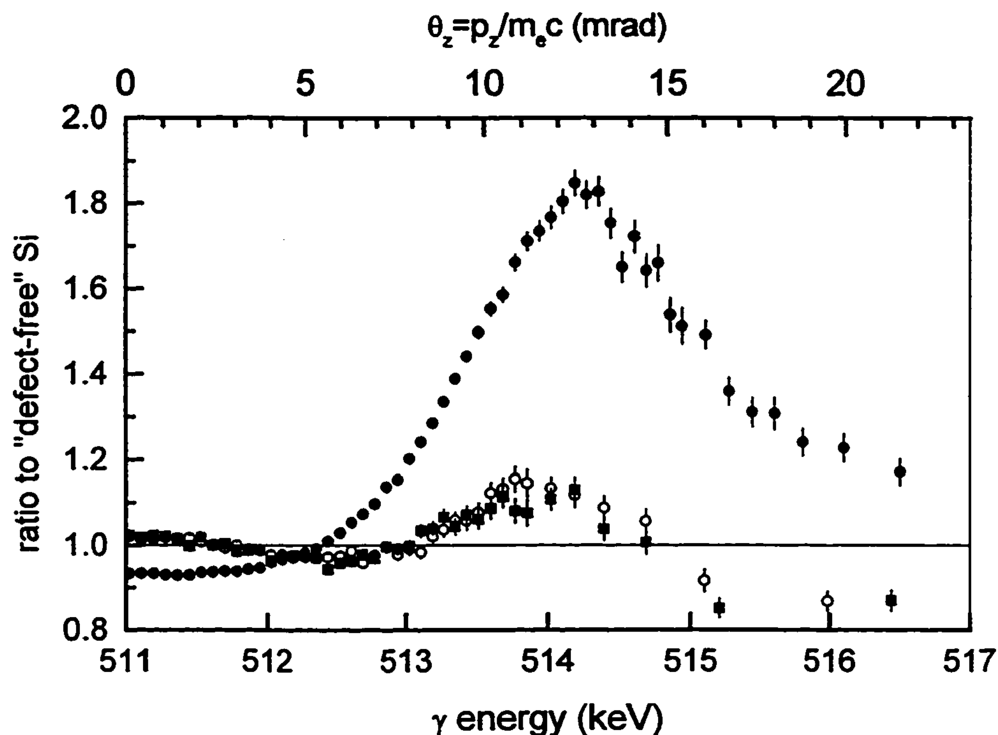

Figure 12. The ratio curves of Si surfaces for various orientation and surface termination. Shown are HF-etched Si(111) (open circles), HF-etched Si(100) (solid squares) and Si(111) covered with native oxide (solid circles).

delocalized states. The line shapes of both surfaces differ from the reference line shape. In the case of the native oxide, low-momentum contribution, i.e. for E_γ <512 keV, is

Reproduced with permission of the copyright owner. Further reproduction prohibited without permission.

observed. In addition, a large hump centered at 514 keV can be identified and it can be considered a signature of silicon oxides. The magnitude of this hump is large compared to the variations observed for open-volume defects. Investigation of a shallow layer in a sample covered with oxide would be very difficult. The ratio curve of the surface of HF-etched silicon resembles bulk Si much more closely, however, the remnant of the hump at 514 keV can be observed (Figure 12). Because the origin of the hump is believed to be oxygen related, the presence of the remnant may be explained by trace amounts of hydroxide covering the surface. Both OH and H terminated bonds were found through the analysis of infrared absorption in HF-etched Si.[30] HF-etched Si(100) was also measured and compared to etched Si(111), see Figure 12. No difference due to surface orientation was observed within experimental error. In most samples investigated hereafter, the native oxide was removed through etching in HF-acid.

Reproduced with permission of the copyright owner. Further reproduction prohibited without permission.

2.5 Defects related to foreign atoms

2.5.1 Moderately-doped Si

In materials that do not contain negatively charged or neutral open-volume defects, positrons annihilate from delocalized Bloch states. When the concentration of impurity atoms is low (less than about 1 %), the average wave function of core electrons is undistinguishable from the wave functions in the pure specimen. Therefore, the annihilation line shapes are expected to be identical in the two cases. This apparent insensitivity to the presence of dopants was checked for n-type Si doped with P, As and Sb. Commercially available wafers, made by Wacker,[32] were used. The dopant concentrations, estimated from the resistivity of the samples, are below 10^{19} cm^{-3}. The ratio curves, referenced to undoped Si, are plotted in Figure 13. In all cases, the ratio curves are almost identical to the unity line representing undoped Si. Small reductions around gamma energy of 514 keV, if any, might be due to vacancy-like behavior. Recently, Avalos and Dannefaer reported identification of trace amounts of vacancy clusters in Chochralski-grown moderately doped Si and FZ undoped Si.[33] The measurements were conducted with positron lifetime spectroscopy, which showed the annihilation rates at the vacancy clusters of several percent. This is consistent with the observation of a small reduction of the core-electron contribution to the annihilation found in our samples. Nevertheless, from now on, it will be assumed that within experimental error, substitutional placement of dopants in Si lattice does not influence the Doppler broadening of the annihilation line.

Reproduced with permission of the copyright owner. Further reproduction prohibited without permission.

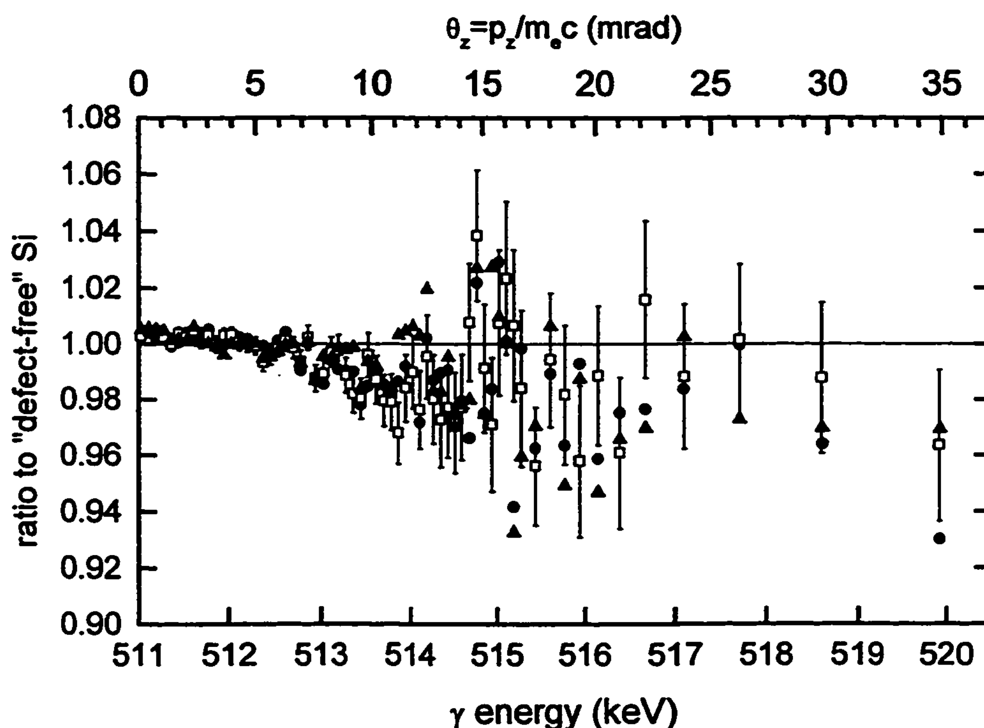

Figure 13. Commercially doped Si is virtually identical to undoped specimens. Sb (solid squares), As (open squares) and P (solid triangles) doped wafers, at dopant concentrations below 10^{19} cm^{-3}, are shown. For clarity, the error bars are plotted only in the case of doping with As.

2.5.2 LT-MBE Si doped with Sb

2.5.2.1 Motivation

Performance of currently manufactured computers is limited by the speed of operation and complexity of built in integrated circuits (IC). Each integrated circuit, e.g. Intel microprocessor Pentium II, consists of millions of small transistors. The speed of operation and the density of the transistors on a chip are some of the most important parameters determining the performance of the system. The number of transistors in a

Reproduced with permission of the copyright owner. Further reproduction prohibited without permission.

chip can be increased if the size of the individual transistors is decreased. Assuming unchanged density of the electrical current, reduction of the geometrical cross section of the transistors results in a reduction of the electrical current. This, in turn, means a decrease of the ratio of signal to electrical noise. Consequently, the total reliability goes down.

Increase of the current that runs through the transistors is a solution. In order to achieve it, the maximum allowed current density needs to be increased. The maximum current density is determined by the number of available electrical carriers in the conduction band of the semiconductors. These electrical carriers come from the doping atoms. Naturally, one would like to place as many dopants as possible. If the semiconductor is grown in equilibrium, the maximum dopant concentration is limited by the solid solubility. Further increase in the dopant concentration results in clustering of the foreign atoms. The atoms of the clusters do not contribute free electrical carriers. For silicon doped with antimony, the limit of solid solubility reaches the maximum value of 7×10^{19} cm^{-3} at 1300 ^{0}C and decreases to about 2×10^{19} cm^{-3} at 700 ^{0}C.[34] Placing more dopant atoms can be achieved if the material is not grown under equilibrium conditions. For this reason, low-temperature molecular beam epitaxy is considered. Increase of the dopant-atom concentration up to about $7x10^{20}$ cm^{-3} yields a linear increase of the number of free electrical carriers. Each doping atom contributes one electron to the conduction band or one hole to the valence band, for n and p-type doping, respectively. This critical value of dopant concentration is far above the limit of solid solubility. Further increase of the dopant concentration does not create more free electrical carriers. A saturation of doping is observed, see Figure 14.[35]

Reproduced with permission of the copyright owner. Further reproduction prohibited without permission.

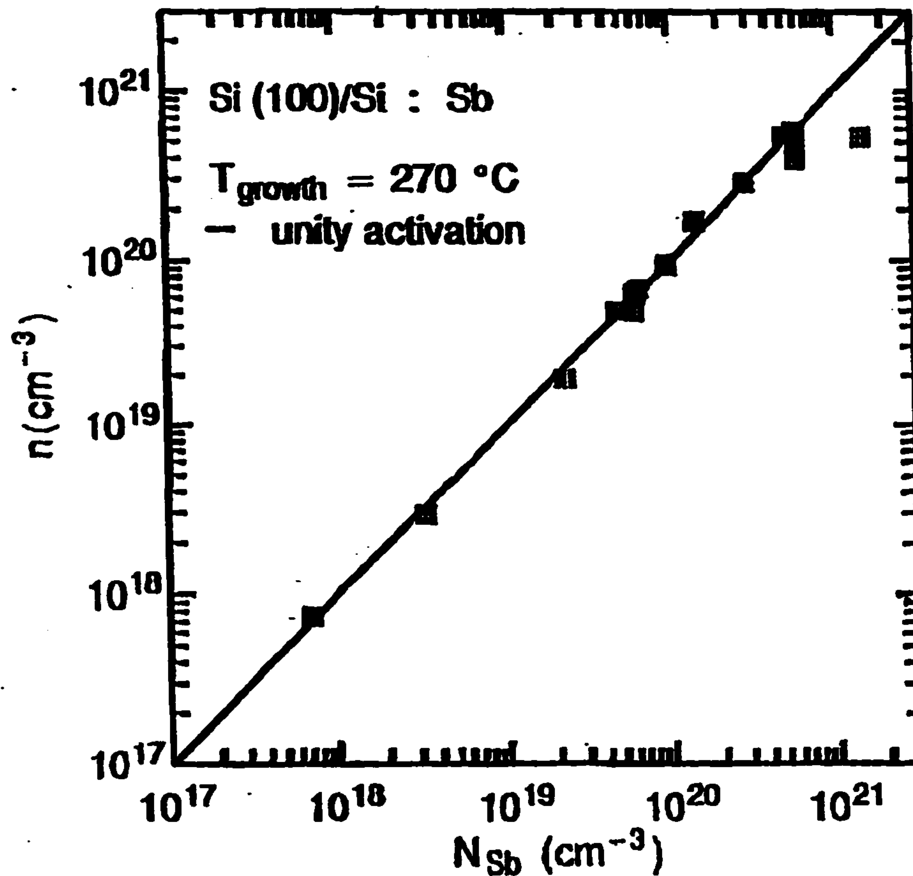

Figure 14. The concentration of the electrons in the conduction band of Si doped with Sb saturates at the level of about 7×10^{20} cm^{-3}. Unity activation of the donors is shown for comparison. After Gossmann *et al.*

Walukiewicz showed that the electron and hole gas is degenerated under high doping concentrations.[36] The degeneration lowers the formation energy of the deep-level defects. When activated, these defects can compensate shallow dopants. Adler *et al* proposed formation of a new defect, Sb tied to a monovacancy, in Sb doped Si.[37] The new defect acts as an acceptor. Sb is a donor in Si environment. When the new acceptor is active, i.e. at high concentrations of Sb, it compensates the dopants.

Reproduced with permission of the copyright owner. Further reproduction prohibited without permission.

There is evidence that the defect of vacancy tied to the dopant atom acts as a dopant-compensation center. Kawasuso *et al* showed this phenomenon for Si doped with P.[38] The samples were irradiated with electrons at various fluences. A reduction of free-electron density, measured using Hall effect, was observed upon the increase of the irradiation fluence. The electron irradiation of Si doped with P is known to produce divacancies and vacancy-phosphorus pairs. Variations of the Fermi level for various irradiation fluences were related to the energy levels of these defects. The authors concluded that vacancy tied to P behaves like an acceptor. Similar behavior could be expected in the case of Si:Sb.

The hypothesis of the formation of a defect of a vacancy tied to Sb at high doping concentrations can be verified using the analysis of the core-electron contribution to the Doppler broadening of the annihilation line. A positron trapped in a vacancy tied to Sb is expected to annihilate with Sb atoms and Si atoms surrounding the vacancy. Each of these scenarios is expected to occur with some finite probability determined by the overlap of the corresponding wavefunctions. The annihilation line of the defect of Sb tied to a vacancy in Si will exhibit momentum contribution of both Sb electrons and electrons from Si atoms surrounding the vacancy. Therefore, in the first approximation, the line shape of the new defect will be a superposition of the line shapes corresponding to the core electrons of Sb and Si surrounding the vacancy. Neglecting relaxation effects, the described defect differs from Si vacancy only by the replacement of one Si atom with Sb. Therefore, the vacancy in the defect can be modeled as Si vacancy. The structures of core-electron shells in Si and Sb are different and so are their momentum distributions. Consequently, the function describing the superposition of the line shapes will have a

Reproduced with permission of the copyright owner. Further reproduction prohibited without permission.

unique shape. The shape will be different from the shape of Sb, Si vacancy and bulk Si considered separately. This unique shape is a signature of the defect and is expected to be easily identifiable if the defect does form. It is important to notice that, as shown in section 2.5.1, positrons do not become trapped at substitutionally located Sb atoms. This is because an open volume is required to effectively trap a positron. In other words, positrons are blind to antimony donors. Therefore, the annihilation lines will be dramatically different when the new defects of Sb tied to a vacancy are present from the case of Sb acting as a substitutional donor.

The measurements of the annihilation line in Si doped with Sb described in the next sections were the first effort to experimentally determine the microstructure of the compensating defect proposed by Adler *et al.*[37]

2.5.2.2 Samples

LT-MBE Si samples with various levels of doping with Sb were grown and investigated. The samples were doped in-situ. Two samples, $n_{Sb} = 9.8\times10^{19}$ cm^{-3} and 5×10^{20} cm^{-3}, were expected to contain Sb atoms acting exclusively as donors. Ability of Sb atoms to contribute electrons to the conduction band would place the samples in the linear regime of the curve plotted in Figure 14. Two samples of higher concentration of Sb, 1.1×10^{21} cm^{-3} and 2.4×10^{21} cm^{-3}, were anticipated to contain the acceptor-like defect of Sb tied to a vacancy. These samples could be placed in the saturated part of the curve in Figure 14. All samples were deposited on Si substrate in a custom molecular beam epitaxy (MBE) system. 50 nm thick layers of Sb-doped Si were grown at the temperature of 220 ^{0}C at the growth rate of 0.02 nm/s. 5 nm thick caps of undoped Si were added to provide identical surface layers for all samples. The positron measurements were

Reproduced with permission of the copyright owner. Further reproduction prohibited without permission.

preceded by cleaning with methanol and 3 min etching in 0.5% HF-acid, followed by rinsing in water for 1 min to facilitate the native oxide removal.

2.5.2.3 Characterization

The ratio curves collected for these samples are plotted in Figure 15. The line shape of defect-free Si was selected for reference during the construction of the

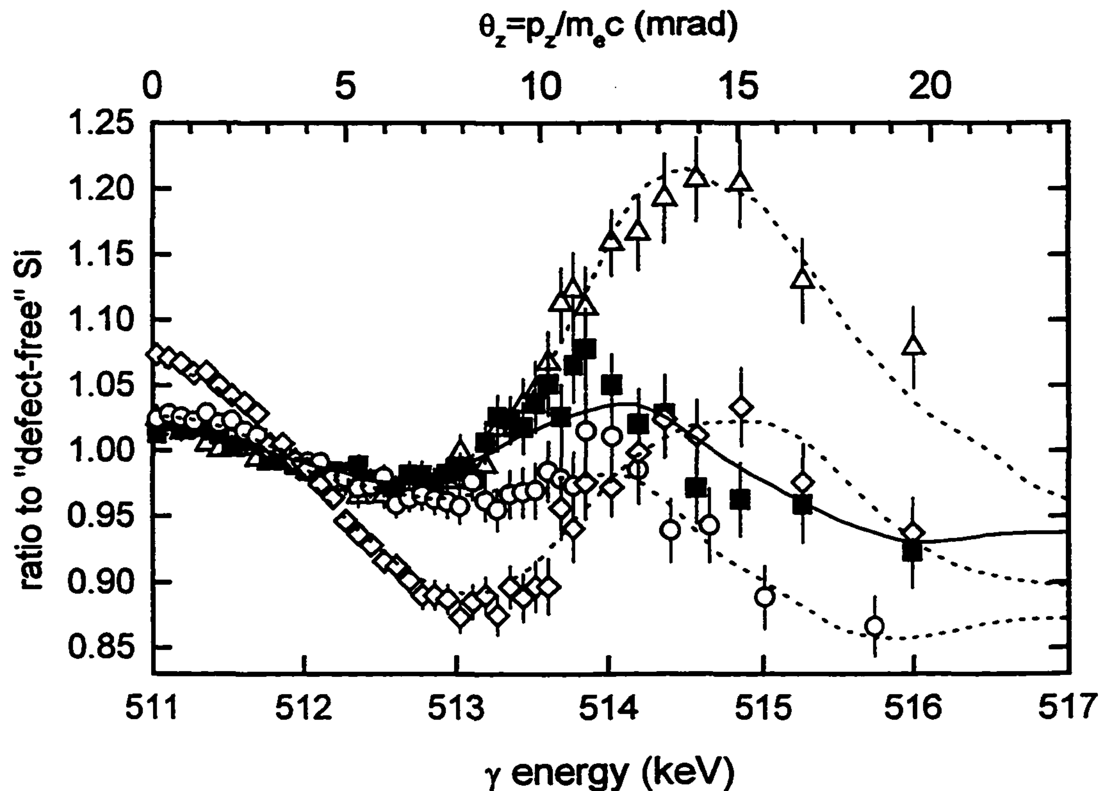

Figure 15. Sb-doped Si for various concentrations of Sb: 9.8×10^{19} cm^{-3} (open circles), 5×10^{20} cm^{-3} (solid squares), 1.1×10^{21} cm^{-3} (open triangles) and 2.4×10^{21} cm^{-3} (open diamonds). The corresponding fits, according to equation 8, are plotted as lines.

ratio curves. Any deviation from the unity line represents defective behavior. According to the model described in section 2.5.2.1, core electron contribution of Sb and Si vacancy

Reproduced with permission of the copyright owner. Further reproduction prohibited without permission.

was expected to shape the ratio curves of Si:Sb samples in the saturated regime of the doping (see Figure 14). The ratio curves of these anticipated contributors were measured in separate "calibration" experiments and are plotted in Figure 16. The plots of the defect-free and defective Sb are plotted and the difference will be explained later in this section. The ratio curve of Si divacancy is plotted to model the vacancy. In addition, the ratio curve of HF-etched Si surface is plotted. Due to small thickness and proximity

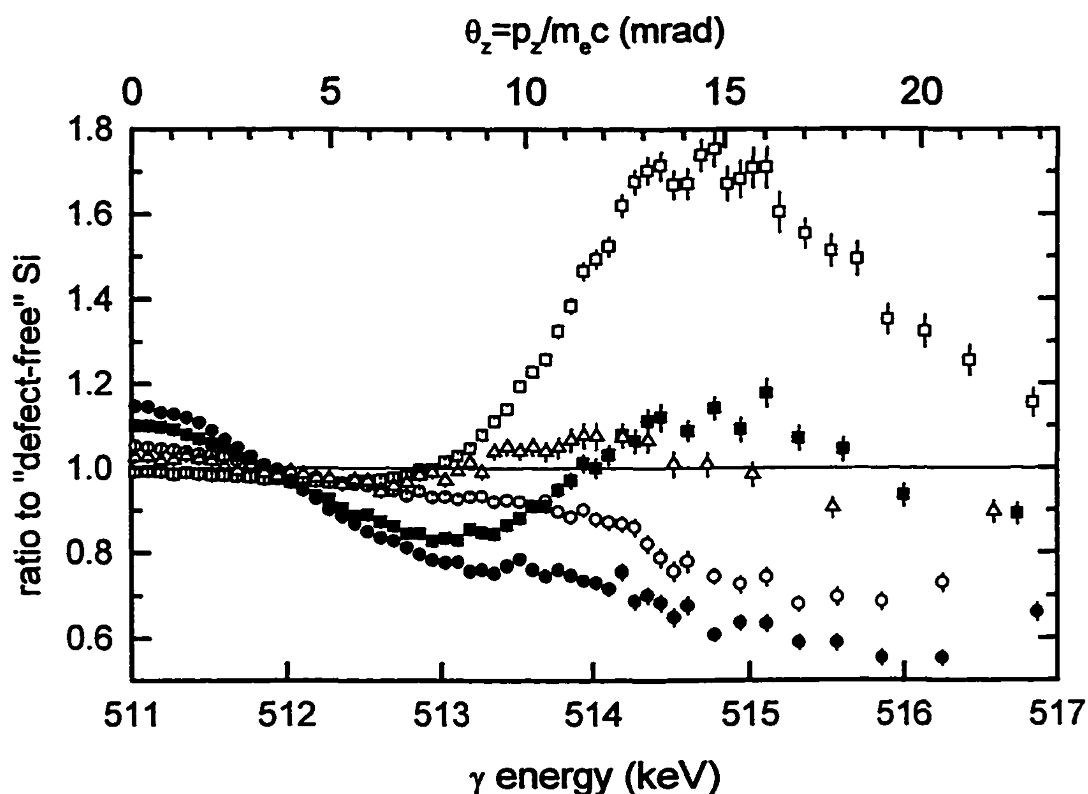

Figure 16. The anticipated components in Sb-doped Si: Si divacancy (open circles), Si void (solid circle), defect-free Sb (open squares), defective Sb (solid squares) and HF-etched surface of Si (open triangles).

Reproduced with permission of the copyright owner. Further reproduction prohibited without permission.

to the surface of the investigated layers, some positrons might diffuse back to the surface. The contribution of positrons annihilating at the surface might influence the ratio curves of Si:Sb layers.

Neither of the ratio curves plotted in Figure 15 closely resembles defect-free Si, Si surface or a combination of these. It means that all of the four samples are defective as seen by positrons. The shape of the ratio curves for antimony concentration of 9.8×10^{19} cm^{-3} and 5×10^{20} cm^{-3} looks similar to the curves of Si divacancy. Therefore, Si divacancy may be considered as the primary defect in these samples. A hump centered at $E_\gamma = 514.5$ keV is visible in the ratio curve of the sample containing Sb at the concentration of 1.1×10^{21} cm^{-3}. The position of this hump coincides with the position of the maximum in defect-free antimony (see Figure 16). Because of the insensitivity of the method to substitutional Sb, the presence of Sb contribution for the sample with $n_{Sb} = 1.1\times10^{21}$ cm^{-3} is in agreement with the model of the formation of the defect of Sb tied to Si vacancy. The lack of Sb contribution at lower Sb concentrations indicates the absence of this defect. Again, this is understandable because at low concentration of Sb, all antimony atoms form substitutional donors. The ratio curve of the highest-doped sample closely resembles the one of the defective Sb. This could be a sign of Sb clustering.

To prove these suggestions, the ratio curve, as a function of energy, of each Sb-doped Si sample was fitted as a linear combination of anticipated reference curves plotted in Figure 16. The fitting was performed using the following formula:

Reproduced with permission of the copyright owner. Further reproduction prohibited without permission.

$$r(E) = a\,Si_{vacancy}(E) + b\,Si_{void}(E) + c\,Si_{no\,defects}(E) + d\,Sb_{no\,defects}(E) + e\,Sb_{vacancy}(E) + f\,Si_{HF-etched\,surface}, \quad (8)$$

where $r(E)$ is the experimental value of the ratio curve at gamma energy E. The fitting coefficients satisfy the normalization constraint: $a + b + c + d + e + f = 1$. The term $Si_{no\,defects}(E)$ was added to accommodate positron annihilation from delocalized Bloch states. The Marquadt-Levenberg least-squares nonlinear fitting routine was applied to experimental data points weighted by statistical errors. No variable averaging routine was applied to the data used for fitting, although the experimental data was averaged prior to plotting. The fitted curves are plotted in Figure 15 as lines. All fitted curves exhibit good qualitative agreement with the experimental data. The fitted coefficients for all four samples are listed in Table I. The entries NA, not applicable, mean that the corresponding

Table I. Results of the fitting of the ratio curves of Sb-doped Si films according to equation 8. NN denotes not needed, i.e. a satisfactory fit could be obtained when this coefficient was set to zero.

Sb concentration (cm^{-3})	a (Si divacancy)	b (Si void)	c (defect-free Si)	d (atoms of defect-free Sb)	e (atoms of defective Sb)	f (surface of HF-etched control Si)
9.8×10^{19}	.51(7)	NN	.26(14)	.06(4)	NN	.17(12)
5×10^{20}	.10(7)	NN	.35(14)	.03(4)	NN	.52(12)
1.1×10^{21}	.38(4)	NN	.20(5)	.42(2)	NN	NN
2.4×10^{21}	NN	.14(9)	.35(16)	.01(6)	.50(12)	NN

Reproduced with permission of the copyright owner. Further reproduction prohibited without permission.

component was not needed in order to get a satisfactory fit. In such a case, the coefficient was set to zero and the fit was repeated to reduce the uncertainties of the other fitted coefficients. The coefficients in each row add to unity and they denote fractions of positron annihilations with electrons of atoms corresponding to the given defect or specimen. Presence of some defects requires a nonzero value of more than one coefficient. This is the case of the defect of Sb tied to Si vacancy. For this defect, "a" and "d" must be simultaneously greater than zero. The ratio a / d is characteristic for this defect and is determined by the ratio of the partial annihilation rates of the positrons annihilating with Si electrons surrounding the vacancy to the annihilation with the electrons belonging to Sb at the defect. This value may be calculated theoretically. It cannot be found experimentally using this method only, because the coefficient "a" may also contain the fraction of annihilations in Si divacancy. This is the ambiguity of the method.

The coefficients found in equation 8 should not be confused with positron trapping rates at defects, although they are related to them. To extract the absolute value of the defect concentration, the corresponding coefficient should be multiplied by the total number of defects seen by positrons. The total number of defects per unit of volume, n, can be derived when the positron diffusion length in the samples is known:

$$n = \frac{\lambda}{\mu}\left[\left(\frac{L_0}{L_{eff}}\right)^2 - 1\right], \tag{9}$$

where λ is the bulk annihilation rate, $(220\ \mathrm{ps})^{-1}$ in Si, μ is the specific trapping rate of the defect, L_0 is bulk diffusion length, 200 nm in Si, and L_{eff} is the effective diffusion length

Reproduced with permission of the copyright owner. Further reproduction prohibited without permission.

in the sample. In the absence of electric fields, presence of defects trapping positrons decreases the effective diffusion length. The positron diffusion length may be found through solving the diffusion-annihilation equation.[3] The sample is conceptually divided into several layers, each characterized by the value of the S parameter. L_{eff} is obtained from fitting the model to experimentally found relation between S and the positron implantation energy. A computer program developed by van Veen *et al*, known as VEPFIT, was used to do it.[16]

All analyzed samples turned out to be defective. Such a conclusion can be made based on the analysis of the coefficients from Table I. For a defect-free sample, only coefficients "*c*" and "*f* should be non zero. This is because in defect-free sample positrons annihilate from delocalized Bloch states or diffuse to the surface and annihilate there. Presence of defects in all samples is in agreement with the results of Szeles *et al.*[1] They proved the formation of open-volume defects in LT-MBE Si films during the early stage of the growth, well before reaching h_{epi}, the limit of epitaxial growth. For samples doped with Sb at concentrations of 9.8×10^{19} cm^{-3} and 5×10^{20} cm^{-3} Si, divacancy is the dominating defect, see coefficient "a". Little or no contribution of antimony was found, see coefficients "d" and "e". This clearly demonstrates the absence of the defect of Sb tied to a vacancy in this range of doping concentrations. These samples were grown in the linear regime of doping and the absence of the defect is in agreement with the model of Adler.[37] The concentration of divacancies was found to be between 8×10^{17} cm^{-3} and 1.6×10^{18} cm^{-3} for both of these samples. The concentration was determined based on equation 9 using the fitted value of the diffusion length of 40±5 nm. The large error in the concentration results from the big uncertainty of the specific trapping rate. The specific

Reproduced with permission of the copyright owner. Further reproduction prohibited without permission.

trapping rate of the double-negatively charged Si divacancy, $(3.5 \text{ to } 7)\times10^{15}$ s^{-1}, was used.[39] Si divacancy may exist in four charge states: single-positive, neutral, single- and doubly-negative. For Sb concentration over 9.8×10^{19} cm^{-3} all donors are activated and the Fermi level is much higher than the activation energy of all charge states of the divacancies.[38] All charge states are activated. Nevertheless, the positron-trapping rate of the double-negative state is the highest. In the first approximation, other charged states can be neglected. The measurements of S vs. implantation energy were performed at elevated temperature (100 ^{0}C) to reduce the internal electric fields in the samples.

The ratio curve of the sample doped to the level of 1.1×10^{21} cm^{-3} differs dramatically from the curves of the samples doped at lower levels. This is reflected in the fitting coefficients listed in Table I. The most striking is the large value of "d", i.e. the contribution of core electrons of antimony. Transmission electron microscopy (TEM) pictures of a similar sample, $n = 1.5\times10^{20}$ cm^{-3}, revealed no evidence of Sb clusters. In addition, extended x-ray absorption fine structure (EXAFS) measurements did not reveal Sb-Sb bonding. Therefore, the contribution of Sb atoms originating from antimony clusters to the coefficient "d" can be excluded. In section 2.5.1, it was shown that positrons are insensitive to substitutionally placed dopants. Contribution of Sb in Si lattice to positron annihilation may be observed only if there is an open volume next to Sb. The defect of monovacancy, divacancy and even larger open volume tied to Sb satisfies these requirements. The non-zero value of the coefficient "a", i.e. Si divacancy, supports this interpretation. Core-electron contribution of Si atoms surrounding the open volume is necessary for a satisfactory fit. The size of the open volume was not determined with this method. The annihilation line shape of Si monovacancy was not

Reproduced with permission of the copyright owner. Further reproduction prohibited without permission.

measured, however, it is believed that its ratio curve closely resembles the one of Si divacancy. Therefore, using positron annihilation techniques only, we cannot determine whether the open volume tied to Sb is of the size of a mono or divacancy. Tri- and quad-vacancies were not measured either. Because no antimony clustering was observed using EXAFS measurements of a similar sample, only one Sb atom is believed to be tied to the open volume in the defect. The number of Sb atoms tied to the defect cannot be currently established through the analysis of the ratio curves. Experimental knowledge of the fractions of annihilation, i.e. of the fitted coefficients of equation 8, is not sufficient. The rates of positron annihilation with electrons of Sb and Si atoms at the Sb-vacancy defect are not known. Theoretical calculations are not available at this point. The analysis becomes even more complex when the presence of undecorated Si divacancies is assumed. The divacancies may be present in the system together with Sb-vacancy complexes. The fitted coefficient “a” may contain the contribution of both defects. In spite of the difficulties encountered during the analysis of the core electron contribution to annihilation line, it is fair to say that formation of the complex of single Sb atom tied to a small vacancy for $n_{Sb} = 1.1\times10^{21}$ cm^{-3} is believed to be the acceptor-like defect responsible for the saturation of doping.

The sample doped at $n_{Sb} = 2.4\times10^{21}$ cm^{-3} is the highest-doped sample in the batch. The dopant concentration places it in the saturated regime of the electrical carrier concentration, see Figure 14. The corresponding ratio curve and the linear-decomposition fit are plotted in Figure 15. The ratio curve of this sample is drastically different than of the $n_{Sb} = 1.1\times10^{21}$ cm^{-3} sample. The high-momentum core-electron contribution, characteristic of defect-free Sb and identified as due to Sb tied to vacancy complex, is

Reproduced with permission of the copyright owner. Further reproduction prohibited without permission.

substantially reduced. This indicates that Sb tied to vacancy is not the dominating defect in this sample. The decomposition analysis did not allow for a proper fit to equation 8 using the components of Si surface, defect-free Si, Si divacancy and void in Si lattice. A good fit was obtained when the component of defective, but high-purity, antimony was added. This behavior may be understood if epitaxy breakdown is considered. Radamson *et al* showed that doping LT-MBE Si with Sb reduces the limit of epitaxial growth.[40] When Sb concentration is increased from 2×10^{20} to 2×10^{21} cm^{-3}, h_{epi} decreases from 100 nm to 2.5 nm. The former Sb concentration is close to the concentration in the sample of $n_{Sb} = 2.4\times10^{21}$ cm^{-3}. The thickness of the layer in this sample, 50 nm, is well above the 2.5 nm limit. Since h_{epi} is strongly dependent on the growth conditions, results of Radamson cannot be directly applied to our samples. It is also known that voids are created in doped LT-MBE Si films when the film thickness exceeds h_{epi}.[41] In the presence of foreign atoms, the value of h_{epi} is slightly different. Epitaxy breakdown in the sample of $n_{Sb} = 2.4\times10^{21}$ cm^{-3} may be deduced from reflection high-energy electron diffraction (RHEED) data. RHEED patterns were collected in-situ for all our samples. The patterns were well defined for the three lowest concentrations of Sb. The patterns disappeared for the highest concentration. This indicates that the last sample exceeded the limit of epitaxial growth. The presence of voids was detected in the sample $n_{Sb} = 2.4\times10^{21}$ cm^{-3}, see coefficient "b" in Table I. The necessity of adding the component of defective antimony to the fit indicates a new defect. Open volume defects in Sb may resemble defects at the interface of Si and Sb. Such interfaces may be found at Sb precipitates in Si lattice. The presence of Sb precipitates is understandable, considering the huge amount of Sb in Si lattice in the sample (5% atomic fraction). This interpretation of the fitted

Reproduced with permission of the copyright owner. Further reproduction prohibited without permission.

coefficient "e" is not unique. Another defect of large open volume tied to several Sb atoms should be considered. Certainly, the size of the open volume is quite large since no Si divacancy – like component was found. The presence of Si voids, see coefficient "b", supports this hypothesis.

Reproduced with permission of the copyright owner. Further reproduction prohibited without permission.

2.5.3 DX centers in Si-doped AlGaAs

2.5.3.1 Motivation

Performance of Si based semiconductor devices is limited by the properties of the base material. Wide band gap compound semiconductors are gaining increasing attention. For several years there have been available devices made of III-V and II-VI compounds, e.g. light emitting diodes (LED) and bipolar transistors made of GaAs. Considerable problems due to native-defect formation have been encountered in the fabrication of devices made of compound semiconductors. One of them is the DX center found in many III-V semiconductors. The DX level is believed to be the electronic ground state of an isolated substitutional donor in a distorted lattice configuration. The DX center introduces an electronic level close to the center of the band gap of the semiconductor. This is often an undesirable phenomenon because n-type doping of a semiconductor is achieved through pinning the Fermi level near a shallow donor level. The presence of a level deep in the band gap causes trapping of electrons from the conduction band and shifts the Fermi level towards the deep level. Consequently, the electrical conductivity of the material is reduced and the doping process is very inefficient. DX centers have been recognized to create serious problems in field-effect transistors and heterojunctions.

A microscopic model of the center in $Al_xGa_{1-x}As$ and GaAs alloys was proposed by Chadi and Chang in 1989.[42] With small corrections, this model can be applied to DX centers in other materials. DX center in Si-doped $Al_xGa_{1-x}As$, $x \geq 0.22$, is formed by a Si

Reproduced with permission of the copyright owner. Further reproduction prohibited without permission.

atom placed at a Ga site. The defect can exist in two configurations. In the first one,

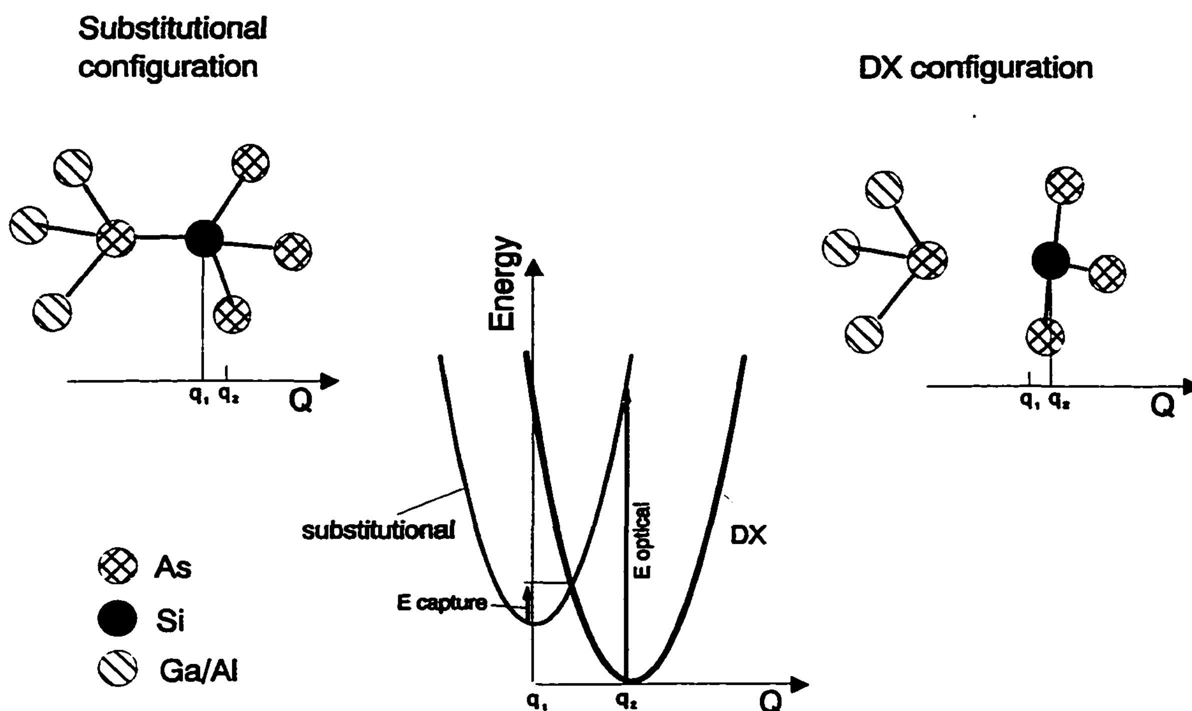

Figure 17. In the DX ground state, the Si atom moves outwards (from the position $Q = q_1$ to q_2) from As creating a small vacancy. Light illumination of the energy over $E_{optical}$ excites the defect. The Si atom goes to the substitutional site ($Q = q_1$). The configuration is stable as long as the thermal energy is below $E_{capture}$. The abscissa of the graph denotes the direction of the movement of the Si atom.

the Si atom stays exactly at the Ga site. This is a metastable configuration. The ground state is obtained by moving the Si atom away from one of As neighbors. A small vacancy is created which can trap two electrons. The microscopic picture and the configuration-coordinate diagram of the defect are shown in Figure 17. The DX configuration is normally occupied. Light illumination with energy of at least $E_{optical}$ shifts the Si atom to the substitutional position. As long as the thermal energy does not exceed $E_{capture}$, the

Reproduced with permission of the copyright owner. Further reproduction prohibited without permission.

defect remains in the metastable state. Raising the temperature above $E_{capture}$ shifts Si atom creating a small vacancy. Because in the relaxed configuration DX center captures two electrons from the conduction band, the transition between the states of the defect can be checked with Hall-effect measurements of the free-electron density.

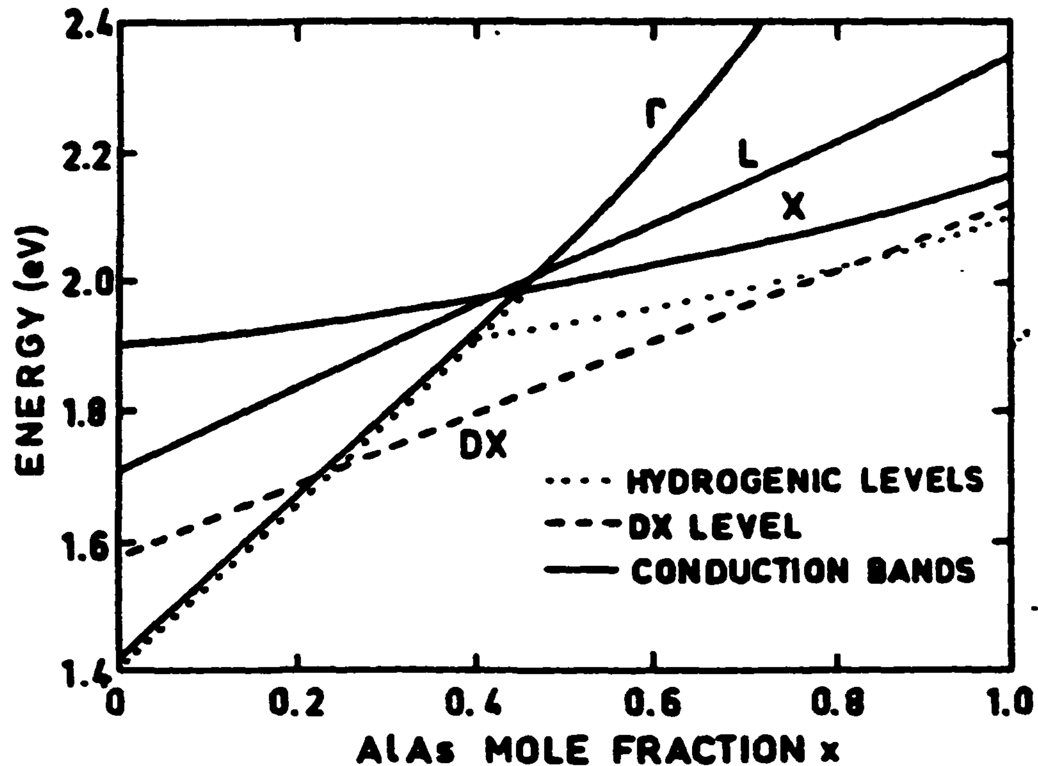

Figure 18. When Al concentration in Si-doped $Al_xGa_{1-x}As$ exceeds 0.22 mole fraction, DX level stays within the band gap. Γ, L and X conduction bands are shown together with shallow dopant levels. After Mooney.[44]

Persistent photoconductivity was indeed observed in Si-doped $Al_{.29}Ga_{.71}As$.[43] Ability to observe the DX center is determined by the energy level of the center with respect to the conduction band. For $Al_xGa_{1-x}As$ Mooney showed that the DX level is in the band gap when $x \geq 0.22$, see Figure 18.[44] At lower levels of Al in the alloy, the DX level steps into

Reproduced with permission of the copyright owner. Further reproduction prohibited without permission.

the conduction band and the transition between the ground and metastable configuration cannot be observed using most methods. Deep-level transient spectroscopy (DLTS) measurements proved that in $Al_xGa_{1-x}As$ the DX center exists in four distinct energy levels. This is explained by four nonequivalent substitutions of Al and Ga atoms at the defect.

Because a small vacancy is formed in the ground state of the defect and it is double-negatively charged, a DX center tends to trap positrons. Therefore, the methods of positron annihilation spectroscopy may be used to investigate the defect. Krause-Rehberg *et al* examined the changes in the lifetime of positrons upon the transition from DX to substitutional configuration during light illumination at low temperatures in $Al_{.5}Ga_{.5}Sb$.[45] A reduction of the vacancy concentration was found upon the excitation of the defect to the substitutional state. Such a change is consistent with the picture of a vacancy involved in the defect. Makinen *et al* investigated Doppler broadening of positron annihilation line due to the existence of DX centers in Si- and Sn-doped AlGaAs.[46] The authors observed a reduction of the core-electron annihilation in the DX configuration referenced to the substitutional one. They interpreted it as due to the presence of a vacancy in the DX center.

In spite of tremendous experimental effort of verifying the microscopic model of the defect proposed by Chadi and Chang, there have been no direct measurements proving the picture. Positron measurements mentioned above indicated the existence of a vacancy as an intrinsic part of the DX center in its relaxed configuration. However, the measurements did not establish the chemical surroundings of the vacancy. Using the analysis of the whole annihilation line shape, it is possible to do so. The next section

Reproduced with permission of the copyright owner. Further reproduction prohibited without permission.

describes the measurements of the chemical surrounding of the vacancy in DX center in Si-doped AlGaAs using reduced-background Doppler broadening spectroscopy of positron annihilation line.

2.5.3.2 Characterization

Si-doped $Al_xGa_{1-x}As$ alloy was selected for the analysis of the chemical surroundings of the vacancy in a DX center. The value of x equal .32 was selected. This alloy is known to contain DX centers.[43] Two samples were grown in a MBE chamber: undoped and doped with Si at the concentration of 4×10^{18} cm^{-3}. The first one was to be used for reference, as it was expected to contain no DX defects. The layers were 2 μm thick and were grown on GaAs substrate kept at the temperature of 580 ^{0}C. The transition from DX configuration to the metastable substitutional one was obtained through infrared light illumination. A GaAs light emitting diode (LED) was used as the source of light. During the illumination, the LED was kept at the temperature of –220 ^{0}C. The illumination lasted for 20 min at an LED current of 25 mA. At this temperature, the diode emits photons of the energy of about 1.3 eV, high enough to excite the DX defect in AlGaAs. The sample was kept at the temperature of 10 K during the illumination.

The effect of light illumination on the core-electron annihilation in Si-doped and undoped samples kept at the temperature of 10 K is shown in Figure 19. The ratio curves were constructed for positron implantation energies ranging between 10 and 20 keV. At positron energies this large, positrons were annihilating exclusively in the investigated layer extending up to 2 μm. The positrons were implanted far from the surface and could not diffuse back. Positron annihilation at the surface would have made data analysis more complicated. Both ratio curves were constructed as the ratio of the annihilation line shape

Reproduced with permission of the copyright owner. Further reproduction prohibited without permission.

in the given sample before and after light illumination. It should be stressed that

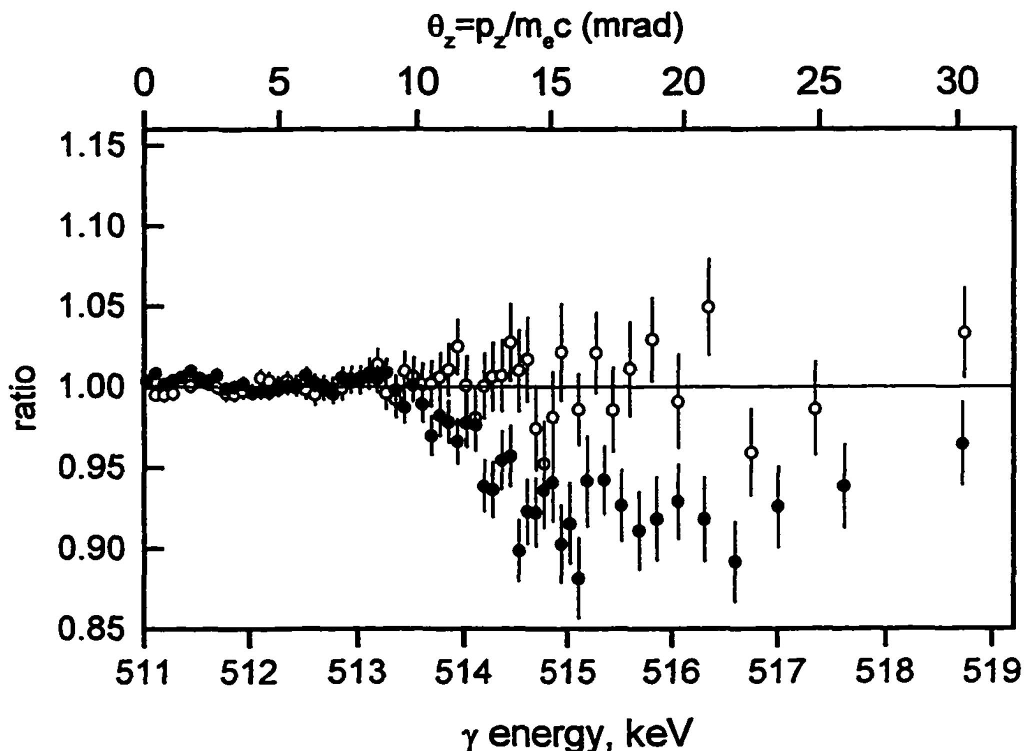

Figure 19. The ratio of before to after light illumination in Si-doped (solid circles) and undoped (open circles) $Al_{.32}Ga_{.68}As$. The measurements were done at the temperature of 10 ^{0}K, in dark.

different reference line shapes were used in the two plots. This presentation method emphasizes the changes due to light illumination and not doping with Si. The undoped sample remains unchanged upon light irradiation (the unity line denotes no change). The Si-doped sample exhibits a reduction of the core electron contribution to the annihilation. This behavior is consistent with the knowledge of the presence of DX centers only in the doped sample.

Reproduced with permission of the copyright owner. Further reproduction prohibited without permission.

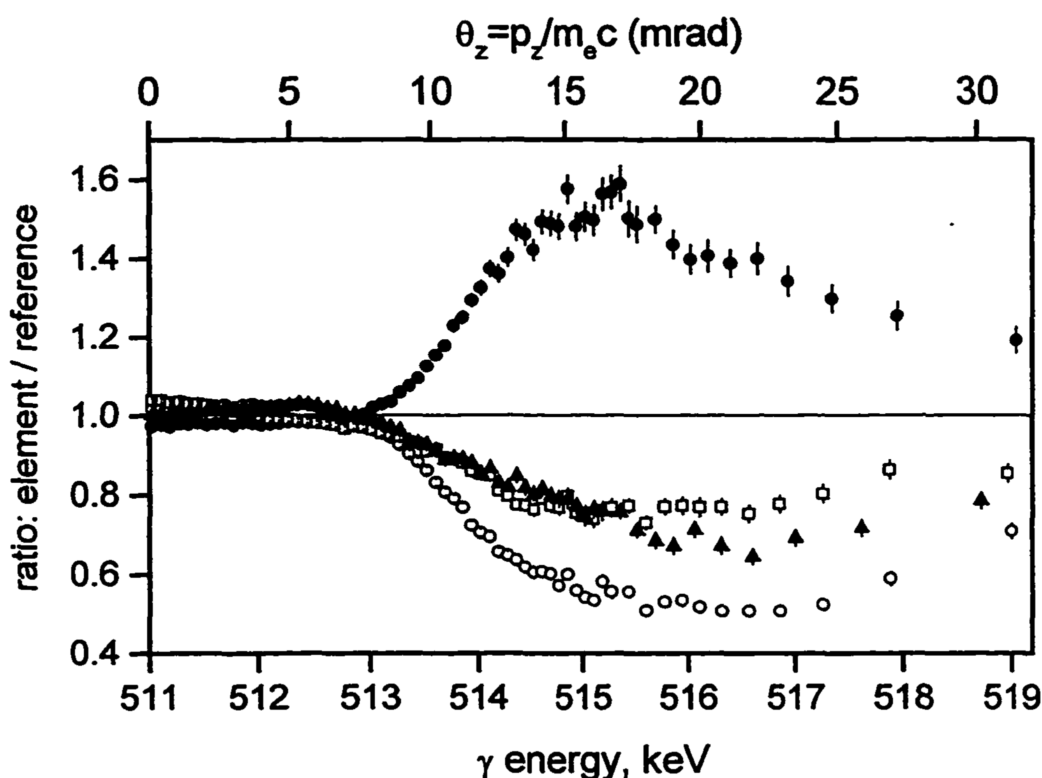

Figure 20. Chemical contributors to positron annihilation at the DX center in Si-doped AlGaAs: Si (open circles), Ga (solid circles), As (open squares) and Al (solid triangles). The annihilation line shape of Si-doped $Al_{.32}Ga_{.68}As$ after light excitation was used for reference.

Due to the larger number of different kinds of atoms possibly involved in the annihilation events, the interpretation of the ratio curve corresponding to the transition between the DX and the substitutional state cannot be done by visual inspection. It must be fitted numerically. The linear decomposition must include all elements present in the specimen, i.e. Si, Ga, As and Al. The line shapes of these elements were measured in separate calibration experiments. The corresponding ratio curves are plotted in Figure 20. The ratio curves are referenced to the line shape of Si-doped sample after light excitation, i.e. the same reference line shape as used in Figure 19 for the doped sample. Non-linear

Reproduced with permission of the copyright owner. Further reproduction prohibited without permission.

fitting was performed for gamma energies, E, between 511 keV and 520 keV to minimize χ^2 according to equation:

$$r(E) = a\,Si(E) + b\,Ga(E) + c\,As(E) + d\,Al(E) + e\,, \qquad (10)$$

where the fitted coefficients satisfy the normalization constraint $a + b + c + d + e = 1$. The results of the best fit are listed in Table II and the fitted ratio curve is plotted in Figure 21. Because the reference line shape, in principle, can be constructed out of all of the elements above, the coefficients should be interpreted as changes in the annihilation fractions, not as absolute values of the annihilation fractions. Therefore, it is meaningful to consider negative coefficients denoting a reduction of the annihilation fraction with the corresponding element.

Table II. Results of the fitting of the ratio curves of before to after light illumination of Si-doped AlGaAs.

Element	% change: (relaxed DX) / substitutional
Si	+8(4)
Ga	-2(3)
As	+7(3)
Al	0

In the relaxed DX state, more annihilation with Si and As is observed and less with Ga. No change in annihilation with Al was found. This is consistent with the

Reproduced with permission of the copyright owner. Further reproduction prohibited without permission.

microscopic model of the DX center in AlGaAs doped with Si, see Figure 17. In the relaxed DX state, the positron is trapped inside a small vacancy formed by outward relaxation of Si atom. Si and As are the nearest neighbors of the vacancy. The increased overlap of their wave functions with the wave function of the positron localized in the

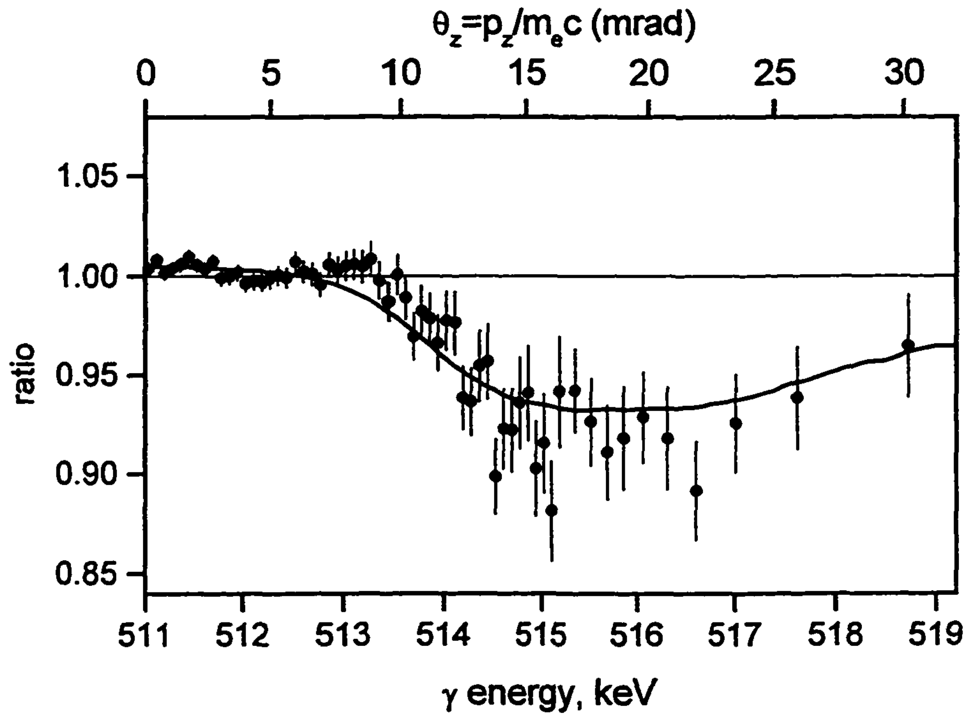

Figure 21. Experimental data (circles) and fit (line) of the ratio curve of the relaxed configuration of the DX center to the substitutional configuration.

vacancy is reflected in the positive values of coefficients "a" and "c".

It should be stressed here that the values of the fitted coefficients in equation have a qualitative, not quantitative character. The error bars are substantial. This is a consequence of the complexity of the alloy. Four distinct elements are present and the corresponding ratio curves might be slightly coupled. In addition, the linear decomposition into the contributions of pure elements may be slightly misleading. The

Reproduced with permission of the copyright owner. Further reproduction prohibited without permission.

line shapes of defect-free elements were used, where positrons annihilate from delocalized Bloch states. The overlap of the localized wave function of a positron trapped in the DX center differs from the case of the delocalized positron. Ratio curves of defective specimens could be used instead of "defect-free" ones. Unfortunately, the variety of the defects in the high-purity elements is tremendous, see section 2.3.1 for examples of defects in pure silicon. The large number of the corresponding ratio curves would make the analysis too complicated to make any conclusions. Nevertheless, it can be said that the core-electron contribution to the Doppler broadening of the annihilation line suggests the following interpretation: a DX center in its relaxed state consists of a vacancy with Si and As as the nearest neighbors. This is consistent with the microscopic model of the center proposed by Chadi and Chang.

2.6 Advantages and disadvantages of the method

Analysis of the core-electrons contribution to Doppler broadening of annihilation line is a very powerful technique. Unlike traditionally used analysis of the S parameter, it allows identification of chemical variations next to open volumes trapping positrons. Nevertheless, the technique has some difficulties. When the number of elements in the compound increases, the complexity of the analysis does the same. The chemical-composition characterization of DX center presented in section 2.5.3 was performed close to the limitations of the method. Four distinct elements were involved, hence, large uncertainties of the results were found. In the linear decomposition of a ratio curve, it is instrumental to know the ratio curves of the anticipated components. In the case of Sb-doped Si, the anticipated components were known fairly well. Analysis of DX center lacked the complete knowledge of the components. The assumption of using defect-free

Reproduced with permission of the copyright owner. Further reproduction prohibited without permission.

specimens for reference was a simplification. After all, wave functions of positrons trapped in DX centers are localized. To investigate the influence of the localization of positron wave functions in compound semiconductors, we applied the decomposition procedure to defect-free AlGaAs. Line shapes of defect-free Ga, As and Al were used and all ratio curves were referenced to defect-free AlGaAs. Naturally, the ratio curve of AlGaAs was a unity line. It was impossible to obtain a satisfactory fit. The fit was performed for electron-positron pair momentum ranging from 0 to about 35 mrad $\times$ m_e c. It means that the conduction and the valence electrons also contributed, not only the core electrons. The overlap of electron and positron wave functions is different in AlGaAs than in pure elemental specimens. This means that linear decomposition of ratio curves is not a proper procedure. The overlaps of the wave functions could be calculated theoretically. Currently, the reliability of theoretical data is not satisfactory in many cases. A comparison of theory to experiment for Si divacancy is shown in Figure 10. The discrepancy is substantial.

The analysis presented in section 2 assumes positrons annihilate exclusively with electrons from first Brillouin zone (umklapp processes). In the systems considered in that section umklapp processes are believed to be small. This is not always true. Mijnarends calculated the umklapp correction to the momentum density in copper.[47] The correction was measurable with PAS.[48]

The insensitivity of the method to small instabilities of the intrinsic resolution function of Ge detectors was observed. The instability is a common problem in standard Doppler broadening measurements. This is because in the case of conduction and valence electrons contribution, the variations of the line shapes are much smaller than the FWHM

Reproduced with permission of the copyright owner. Further reproduction prohibited without permission.

of the resolution of the detector. It is not so for the core-electron contribution. The phenomenon was tested experimentally. The FWHM of the detector was intentionally increased from 1.57 keV to 1.60 keV. The S parameter changed dramatically under such conditions but the core-electron contribution remained the same.

Although the level of background was substantially reduced as compared to the single-detector setup, it was still noticeable. It can be further decreased when two germanium detectors are employed and two-dimensional mapping of the momentum densities is done.[4]

To summarize, the analysis of the full function describing the line shape in Doppler broadening experiments is extremely powerful. Chemical composition of open-volume defects can be established. The technique was used in the analysis of acceptor-like defects in Sb-doped Si and DX centers in AlGaAs.

Reproduced with permission of the copyright owner. Further reproduction prohibited without permission.

3 Construction and applications of a prototype positron-lifetime spectrometer on a variable-energy positron beam

3.1 Motivation

A positron injected into a solid thermalizes within several picoseconds. Then it diffuses. During the diffusion it annihilates from delocalized Bloch state or becomes trapped at an open-volume defect and annihilates there. Under certain conditions, it may bond with an electron forming positronium (Ps) and annihilate from a bound state of Ps. Neglecting positron diffusion, the number of positrons in the system can be described by combined trapping-detrapping-annihilation equation. For *N*-decays system, the time evolution of the total population *n(t)* is given as a sum of the populations of the states:[49]

$$n(t)=\sum_{i}^{N} n_i(t), \tag{11}$$

where $n_i(t)$ satisfy a set of differential equations:

$$\frac{dn_i(t)}{dt}+\left(\lambda_i+\sum_{j}^{N} K_{ij}\right)n_i(t)=\sum_{j}^{N} K_{ji}n_j(t), \tag{12}$$

where λ_i denotes positron annihilation rate in state *i*, K_{ij} is the transition rate from state *i* to state *j*. The sum over *j* on the left side of the equation describes detrapping from state *i* and on the right side – trapping into state *i*. The counts vs. lifetime spectrum, proportional to the solution *I(t)* of equation 12, is of the form:

Reproduced with permission of the copyright owner. Further reproduction prohibited without permission.

$$I(t)=\sum_i I_i \exp(-t/\tau_i), \quad (13)$$

When $N = 2$, i.e. when there is only one kind of defects trapping positrons, and the detrapping process is not likely, equation 13 simplifies so that:

$$\begin{aligned} \tau_1 &= (\lambda_b+\kappa_d)^{-1} \\ \tau_2 &= \tau_d \\ I_2 &= \frac{\kappa_d}{\lambda_b-\lambda_d+\kappa_d} \end{aligned}, \quad (14)$$

where λ_b and λ_d are defect-free, and defect annihilation rates, respectively, $\tau_d = 1 / \lambda_d$ and κ_d is the trapping rate at the defect. It is possible to incorporate the diffusion of positrons into equation 12.[50] Such treatment is required when positrons diffuse between layers containing different defects.

The trapping rates in the equations above are a product of the defect concentration, c, and specific trapping rates, ν, i.e. $\kappa = c\ \nu$. Knowing the specific trapping rate, it is possible to obtain defect concentration, c. The specific trapping rate can be calculated using Fermi golden rule:

$$\nu = 4\pi\sum_{i,f} P_i P_f \left|M_{i,f}\right|^2 \delta(E_i - E_f), \quad (15)$$

where P_i and P_f denote occupation probability of initial and final electron-positron state, respectively. $M_{i,f}$ is the matrix element of the interaction process between initial and final states. To get the total specific trapping rate, ν needs to be summed over all possible initial and final states. Puska *et al* calculated the specific trapping rates in undecorated vacancies in silicon.[51]

Reproduced with permission of the copyright owner. Further reproduction prohibited without permission.

After becoming trapped at a defect, a positron is bound to annihilate or detrap from the defect. Annihilation may also occur from a delocalized positron state. In any case, the positron annihilation rate depends on the overlap of the electron and positron wave functions. The positron lifetime τ is the inverse of the annihilation rate λ. The annihilation rate can be expressed as:

$$\lambda = \sum_i \int \rho_i(\bar{p}) d\bar{p}\,, \tag{16}$$

The contributions of all electronic shells i are summed. The density of momentum of the combined positron-electron wave functions ρ_i is given by equation 4. According to equation 4, the annihilation rate increases with the increase of the overlap of electron and positron wave functions. Equation 16 is valid for both localized and delocalized positrons. The difference comes from the choice of the positron wave functions. The experimental values of positron lifetime in solids vary from about 90 ps (95 ps for defect-free nickel[52]) to about 500 ps (large vacancy clusters in silicon). Larger positron lifetimes are possible when the positron bonds with an electron forming positronium. Ps formation is known to occur at surfaces[53] and at voids in insulating materials, e.g. porous silicon.[54] The longest lifetime of Ps in vacuum is 142 ns. This is the lifetime of $^3S_1$ state called ortho-Ps. In solids, the lifetime of ortho-positronium may be shorter than 142 ns. The lifetime of positronium trapped in a void depends on the volume of the void. Reduction of the volume causes increased overlap of the wave function of the positron from Ps with the wave functions of electrons at the boundary of the void. The increase of the overlap translates into increased probability of positron annihilation with electrons at the boundary of the void. This process is called "pick off" annihilation. Annihilation with the electron bound in Ps is no longer the only possibility of the annihilation of the positron

Reproduced with permission of the copyright owner. Further reproduction prohibited without permission.

from Ps. The extra channel of reaction reduces the lifetime of Ps in voids. Nakanishi *et al*[55] found a theoretical expression for Ps lifetime τ (expressed in ns) in terms of the void radius, R:

$$\frac{1}{\tau} = 2\left(1 - \frac{R}{R+\Delta R} + \frac{1}{2\pi}\sin\left(\frac{2\pi R}{R+\Delta R}\right)\right), \tag{17}$$

where ΔR is the thickness of the of the electron layer at the edge of the bubble. ΔR is a fitted parameter and in molecular solids is equal 1.656 A.[55]

The strength of positron lifetime measurements comes from the dependence of the annihilation rate on the local density of the electrons. The distribution of the electron density constitutes a signature of a defect. Defects can be characterized based on their lifetime value. The analysis of temperature behavior of the specific trapping rate allows identifying the charge state of the defect.[51] The defect concentration can be extracted. The defect concentration may be also found from the analysis of the diffusion length found from Doppler broadening data. In practice, however, the effective diffusion length is modified by intrinsic electric fields in the sample. Extracting the diffusion length and defect concentration from Doppler broadening data is sometimes difficult. The positron lifetime analysis works especially well in the presence of only one or two kinds of defects in the sample. Even in complex systems, qualitative variations may be analyzed.

3.2 Positron lifetime spectrometers - introduction

The following sections are dedicated to the design, testing and applications of a prototype positron lifetime spectrometer mounted on a variable energy beam. The design of the spectrometer is based on a modified suggestion of Y. Kong.[56] Although the

Reproduced with permission of the copyright owner. Further reproduction prohibited without permission.

concept is well known, the system has never been built and tested. Existing positron lifetime spectrometers will be reviewed (section 3.3). Physical processes related to the design of the lifetime spectrometer will be considered (section 3.4). The new design will be described in detail in section 3.5.1.1. Results of computer simulations of the performance of the system will be compared to experimental data (sections 3.5.1.3 and 3.5.1.4). Application of the new spectrometer to the investigation of materials of low dielectric constant will be discussed in section 3.5.1.6. The successful system was my second design. The first one was based on my original idea. Unfortunately, it did not perform satisfactorily. Nevertheless, the work on the design allowed me to gain experience necessary in the construction of the second, fully operable apparatus.

3.3 Review of existing lifetime setups

Several systems for the measurement of the lifetime of positrons in solids have been developed. They differ in the method of providing the control signals for the measurement of the time interval corresponding to the lifetime of a positron. All of them utilize the annihilation gamma ray as the stop signal. The gamma ray is usually detected using a scintillator, e.g. plastic or BaF_2 coupled to a fast photomultiplier tube (PMT). The start signal can be provided in many ways. Lifetime spectrometers can be used to investigate the whole specimen on average or as a local probe. The former class of methods is usually referred as "bulk" setup. Local-probe spectrometers must be installed on a variable-energy positron beam. This is necessary to provide depth resolution. Positrons of specific energy probe the specimen in a layer placed at some distance from the surface. The details of the process are described in section 2.1. Some applications require localization of the investigated area in three dimensions. Transverse resolution is

Reproduced with permission of the copyright owner. Further reproduction prohibited without permission.

obtained by reducing the cross section of the positron beam. Microprobes of about 20 micron in diameter have been successfully constructed.

3.3.1 "Bulk" lifetime techniques

Two bulk-lifetime techniques have been described in literature: gamma-gamma coincidence and positron-gamma coincidence.

3.3.1.1 Gamma-gamma coincidence

The gamma-gamma coincidence method is based on the radioactive decay scheme of ^{22}Na isotope used as the positron source, see Figure 22. Emission of a positron leaves the isotope in an excited state. It decays with the decay time of 3 ps emitting a gamma ray of the energy of 1.2746 MeV. Detection of this gamma ray constitutes the start signal for

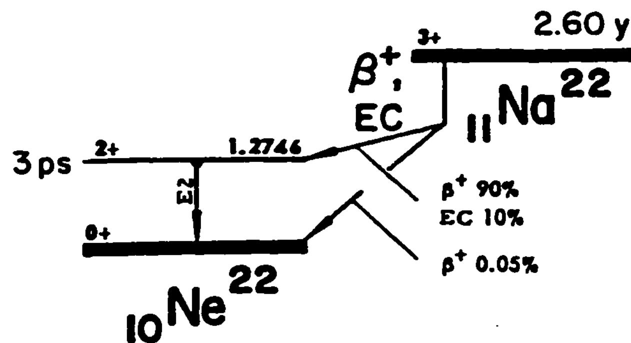

Figure 22. The decay scheme of ^{22}Na, from *Table of Isotopes.*[57]

the measurement of the positron lifetime. The decay time of 3 ps is small compared to usual positron lifetimes. The energy of the positrons emitted from ^{22}Na is a few hundred keV. Placing the radioactive source close to the sample makes the travel time of the positron from the source to the investigated specimen insignificant. The energy of the gamma ray, 1.2746 MeV, is much larger than 511 keV, the electron-positron annihilation

Reproduced with permission of the copyright owner. Further reproduction prohibited without permission.

energy. Therefore, it is possible to distinguish the two gamma rays and not to confuse the start and stop signal of the lifetime measurement. The schematic of a typical setup is shown in Figure 23.[58] A drop of ^{22}Na source is sandwiched between two pieces of the sample. Two sets of scintillator / PMTs are placed on the opposite sides of the source/sample sandwich. One detector detects the start signal, i.e. 1.27 MeV, while the

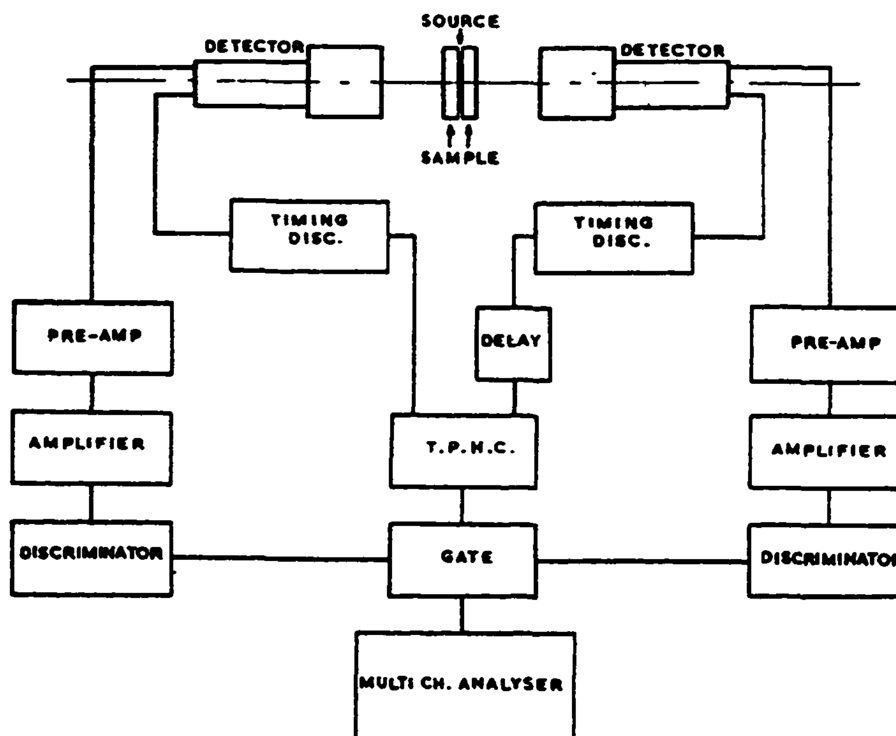

Figure 23. The schematic diagram of a typical "bulk" positron lifetime spectrometer. TPHC states for time to pulse height converter. From West.[49]

other is used for the detection of the stop signal, i.e. the annihilation gamma ray.

The described system is successfully used in hundreds of laboratories in the world. The gamma-gamma coincidence systems have the best timing resolution of all lifetime spectrometers. FWHM = 120 ps is a commonly achieved value. In addition, the ratio of the top value of the lifetime spectrum to the background value is large, usually four orders of magnitude. Such a large ratio makes the system useful in the analysis of

Reproduced with permission of the copyright owner. Further reproduction prohibited without permission.

samples with relatively low concentration of defects. It should be stressed, though, the system does not allow for depth resolution in the analysis of the defects.

3.3.1.2 Positron-gamma coincidence

Lifetime start signal can by provided by direct detection of a positron prior to its entrance into the sample. It can be accomplished by making the positrons fly through a thin scintillator sensitive to positrons, e.g. Pilot U plastic. A photomultiplier tube may be used to collect the light from the scintillator. This method, known as β+ gamma coincidence, was implemented by Weiler *et al.*[59] A respectable value of the timing resolution of 270 ps was reported. The described setup cannot be used with positrons of the energy of several keV, the value required in depth-resolved measurements. This is because a low energy positron passing through a scintillator looses all of its kinetic energy and annihilates in the scintillator, not in the sample.

Gidley *et al* used a similar setup to measure the lifetime of ortho-positronium in SiO_2 powders.[60] Positrons from Ge^{68} source were passing a .5 mm thick scintillator prior to striking the powdered target. At the target, the positrons formed Ps with the probability of 0.15. All three gamma rays of ortho-Ps annihilation were detected in three separate detectors. Three-event detection allowed distinguishing ortho-Ps decay from two-gamma decay of positrons not bound in Ps.

3.3.2 Variable-energy beams

The lifetime systems described above lack the depth resolution. This is because the positrons from radioactive sources are not monoenergetic. The energy varies from zero to 545 keV. The penetration depth of the injected positrons depends on their energy.

Reproduced with permission of the copyright owner. Further reproduction prohibited without permission.

Positrons of such a large energy penetrate solids tens of microns deep and are not sensitive to near surface defects. Many applications deal with defective layers spaced closely to the surface of the specimen. When the investigated layer is within 100 nm from the surface, monoenergetic positrons of the energy of a few keV must be employed. Several systems have been developed to address the task. They can be divided into two groups: pulsed positron beams and secondary electrons triggered beams. The following paragraphs outline the principle of operation these beams.

3.3.2.1 Secondary-electron triggered setup #1

The collection of secondary electrons generated upon positron entrance into the sample is used in the spectrometer described by Lynn *et al*, see Figure 24.[61] The incident

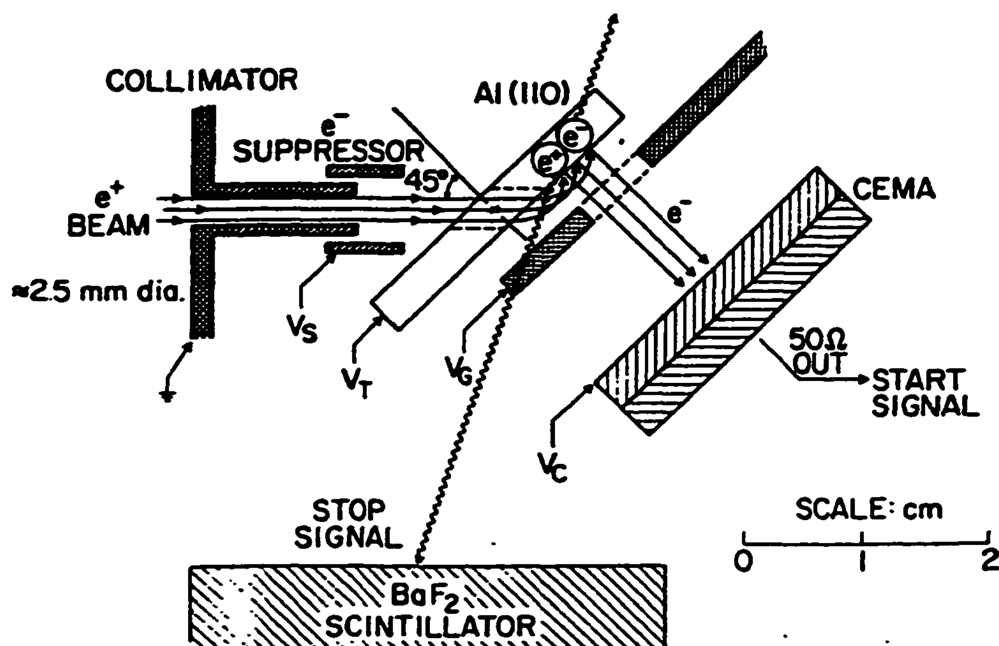

Figure 24. The positron lifetime spectrometer utilizing the detection of the secondary electrons to trigger the lifetime clock, see text. (from Lynn *et al.*[61])

Reproduced with permission of the copyright owner. Further reproduction prohibited without permission.

positrons of the electrostatically guided beam are transported through a hole in the sample tilted at 45 deg. Next, they are deflected back onto the sample in retarding electric field. Secondary electrons emitted after a positron hit the sample are accelerated in the same electric field, pass through a grid and are collected in a channel electron multiplier array. The signal from this detector starts the clock to measure the lifetime of the positrons. The clock is stopped by an annihilation gamma ray collected in a BaF_2 scintillator coupled to a photomultiplier tube. Because the electrons are accelerated in a strong electric field, about 8 kV/cm, their time of flight as well as its spread are rather short. The system was used to successfully measure the lifetime of positron surface-state in Al. Timing resolution FWHM of about 600 ps was reported. The value included not only the instrumental resolution but also the decay of the positron annihilation. Therefore, the value of the instrumental resolution itself was, presumably, much less than 600 ps. The ratio of peak to background of about 300 was obtained. It allowed resolving two distinct lifetime components of the surface state, in addition to fixed lifetimes of bulk Al, ortho- and para-positronium. The performance of the system was very good but no further experiments have been reported. The system cannot be implemented in a magnetically guided positron beam without major modifications. This is because the incident positrons would follow the lines of magnetic field and positrons would not annihilate at the sample.

3.3.2.2 Secondary-electron triggered setup #2

A conceptually similar system to the one described above was proposed by Kong,[56] see Figure 25. Similarly, secondary electrons are used to trigger the positron lifetime clock. The main difference lies in the method of guiding the positrons to the

Reproduced with permission of the copyright owner. Further reproduction prohibited without permission.

sample. Here, magnetically guided positrons hit the sample directly, without any reflections in electric field. The positrons pass through a hole in a micro-channel plate detector. This detector is used for the collection of the secondary electrons emitted when a positron strikes the sample. An electric field between the sample and the micro-channel plate is applied in order to accelerate the secondaries. The described system was tested briefly and the results were not satisfactory. In addition to the lifetime decay, several peaks were observed in the lifetime spectrum. They were caused by reflections of the positrons and the secondary electrons. The peaks were highly undesirable and their presence would make the analysis of real data difficult. Only preliminary results are available. I believe, the applicability of the system in positron-lifetime measurements is

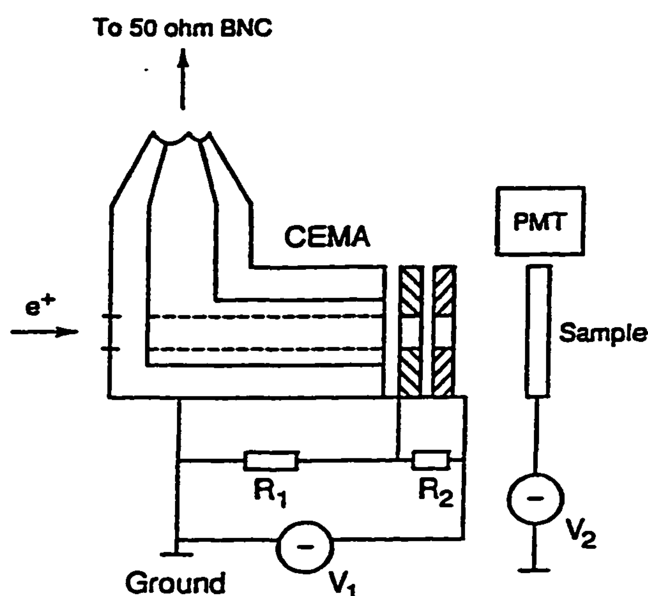

Figure 25. The lifetime spectrometer developed by Kong. After passing through a hole in the detector of the secondary electrons, the positrons generate the secondary electrons upon reaching the sample. The detection of the secondaries starts the lifetime clock.

Reproduced with permission of the copyright owner. Further reproduction prohibited without permission.

limited. This is because in order to obtain short time of flight of the secondary electrons, strong accelerating electric field needs to be applied between the sample and the channel electron multiplier array (CEMA). Application of this strong field would constrain the electrons to follow the lines of the electric field. This, in turn, would make the electrons follow the trajectories of the incidence positrons and go back to the positron source, not to the detector of the electrons.

3.3.2.3 Pulsed beams

In addition to triggering the positron lifetime clock using secondary electrons, pulsed beam techniques have been developed. In a pulsed beam, the clock starts at the instance when a positron is known to be available. This is accomplished by introducing time-dependent electric fields that control the position and speed of the positrons in the beam. The time-dependent fields are correlated with the electrical signal triggering the lifetime clock. Several methods of timing positron beams are known.[62]

One way to time-focus the beam of charged particles is to gate it with time-varying electric field. The positrons pass the gate unless a retarding electric field is applied. Such a system, commonly referred to as an electric chopper, cannot work as a stand-alone device. This is because the beam intensity drops linearly with the reduction of the open-gate time.

To increase the probability of having a positron available at a given instant, positrons can be bunched. A harmonic buncher may be used to make positrons arrive at some point simultaneously independent on the initial position. The input gate of the buncher remains open for a preselected time to let positrons in. Then the electrical gate closes and harmonic, position dependent, potential $V(z) = k z^2 / 2$ is applied. All positrons

Reproduced with permission of the copyright owner. Further reproduction prohibited without permission.

trapped within the buncher arrive at $z = 0$ at the same time as long as the initial speed of the positrons is low. This phenomenon of frequency independence on amplitude in a harmonic potential is well known. Its mechanical equivalent was employed in the construction of pendulum-based clocks. The instant when the harmonic potential is applied marks the triggering signal for the positron lifetime clock.

The beam of charged particles can be time focused with a time dependent longitudinal electric field. At the beginning of the cycle, the particles in the buncher are decelerated and at the end – accelerated.

Several pulsed beams using the principles outlined above have been built. The first one was built in Munich, Germany, in 1985.[63] The pulsed beam built in Japan has been described by Suzuki *et al.*[64] An excellent value of the timing resolution of FWHM = 240 ps was reported. A large ratio of peak to background equal 1000 was obtained and the timing events delayed up to about 30 ns could be analyzed. These numbers qualify the beam as a state of the art device. The performance is only slightly worse than of a bulk lifetime system but provides much greater versatility due to available depth resolution.

A similar beam with added transverse resolution of about 20 μm and the timing resolution of 350 ps at positron energies ranging from 2 keV to 10 keV was reported by Zecca *et al.*[65] Squeezing the beam in transverse direction was obtained with the aid of an electrostatic lens.

Reproduced with permission of the copyright owner. Further reproduction prohibited without permission.

3.4 Physical background of the design of the positron lifetime spectrometer

3.4.1 Processes stimulated by positrons hitting specimen

Several processes are stimulated by positron entrance into the specimen.[66] Collection of emitted secondary electrons is considered the most appropriate for triggering the positron-lifetime clock. This is because of relatively high efficiency of the production of the secondary electrons, close to unity, and prompt emission of the electrons within several picoseconds. Other processes include plasmon excitations, ionization of inner atomic shells leading to the emission of characteristic x-rays or Auger electrons, continuum x-rays called Bremsstrahlung and excitation of phonons. Positrons may also scatter elastically but an elastic process alone does not lead to the emission of any detectable particles other than positrons due to the conservation of energy. The calculations were performed for electrons hitting aluminum target but the result should be comparable to positron-induced processes.

The probability of plasmon excitations, i.e. collective oscillations of the conduction- and valence-band electrons, is second highest after the elastic scattering. The excitation of the plasmons is delayed by only several femtoseconds after the entrance of the plasmon-inducing particle into the specimen. Nevertheless, efficient collection of plasmons is difficult. For the same reason, phonons are not considered. The efficiency of the Auger process is only several percent. This is much lower than the efficiency of the generation of secondary electrons for the energy of incident positrons above 100 eV. Positron-induced ionization of the inner atomic shells leads to the emission of

Reproduced with permission of the copyright owner. Further reproduction prohibited without permission.

characteristic x-rays. It is a fast process with the lifetime dependent on the element but usually of the order of a picosecond. The efficiency of the process is low,[66] about 5×10^{-5} sr^{-1}. A spectrometer utilizing collection of the characteristic x-rays would be impractical.

Detection of the secondary electrons induced by the primary positrons seems to be the best choice. A conceptual diagram of a lifetime spectrometer using the secondary electrons to start the lifetime clock is shown in Figure 26. A beam of positrons is directed onto the sample. The secondary electrons are generated when a positron enters the

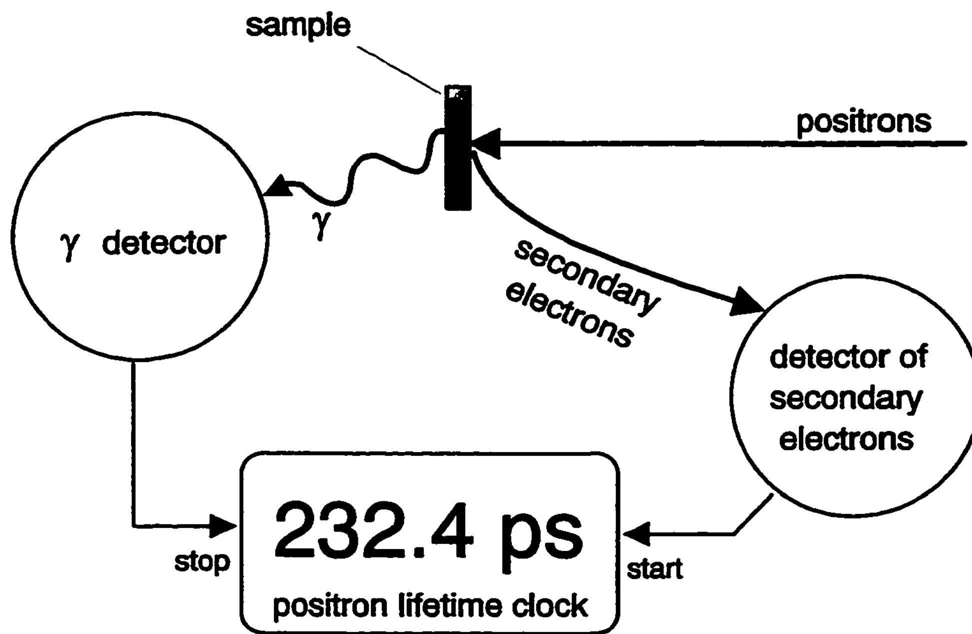

Figure 26. The conceptual diagram of a positron lifetime spectrometer using the signal of the secondary electrons to start the lifetime clock. The clock is stopped upon the detection of the annihilation radiation.

sample. The secondaries are detected in a dedicated detector. A pulse from this detector initiates the measurement of the lifetime of the positron. After a while, the positron annihilates in the sample and emits gamma rays. One of these rays is collected in the gamma-radiation detector. The pulse from the gamma detector stops the measurement of

Reproduced with permission of the copyright owner. Further reproduction prohibited without permission.

the lifetime of the positron. The scheme is being repeated until enough events have been collected to show the statistical distribution of the lifetime of the positrons in the sample.

Not all positrons induce emission of the secondary electrons. The transport of the secondary electrons from the sample to the detector takes a considerable amount of time. This time depends on the speed and the direction of emission of the electrons. The variations of the time of transporting the secondaries create an uncertainty in defining the instant when to start the clock. This translates into an error of the measurement of the positron lifetime. Therefore, it is important to consider physical properties of the secondary electrons. A review is presented in section 3.4.2. Occasionally, a positron directed onto the sample fails to remain there permanently. It may backscatter and annihilate at the second contact with a solid piece of apparatus. Multiple backscattering events are also possible. The positron that backscattered from the sample may generate some secondary electrons. These electrons start the lifetime clock. The clock stops when an annihilation gamma ray is detected. In the case of the backscattered positrons, the annihilation takes place at an uncontrolled position. Therefore, it is undesired. To estimate the magnitude of the problems related to the backscattered positrons, it is necessary to predict their behavior. The knowledge of physical properties of backscattered positrons is reviewed in section 3.4.3.

3.4.2 Secondary electron emission

3.4.2.1 Consequences of the nature of secondary electrons

Having decided to use secondary electrons to trigger the positron clock, it is necessary to understanding some details of the process of emission of the electrons. The

Reproduced with permission of the copyright owner. Further reproduction prohibited without permission.

total yield of the emission influences the coincidence count rate as well as the level of the systematic background in the lifetime spectrum. This is because most background counts are related to the backscattered positrons. An increase of the ratio of the yield of the secondary electrons to the yield of the backscattered positrons would improve the signal to background ratio. The initial energy of the secondary electrons influences the time of flight of the electrons from the sample to the detector. So does the emission angle. The distribution of the energy of secondary electrons as well as of the emission angles determines the uncertainty of the time of flight of the electrons. This translates into smearing of the timing resolution of the instrument. Information on the secondary electrons is provided in section 3.4.2.2.

3.4.2.2 Emission of secondary electrons induced by positrons - theory and experiment

In this section, I will review theory and experimental data pertaining the emission of secondary electrons. The process of emission of secondary electrons consists of electron-production stimulated by the primary particle, followed by transport to the surface and escape. The secondaries are created by collisions of the primary particles with the free gas of valence electrons. Due to limited penetration depth of low-energy secondaries, only electrons generated within several nanometers from the surface may escape. Baroody derived expressions for the total yield of secondaries as well as the energy and angular distribution.[67] The expressions were derived for electron-induced emission of secondaries. Nevertheless, approximately, they are applicable to positron-induced emission. The total yield of secondaries produced by primaries:

Reproduced with permission of the copyright owner. Further reproduction prohibited without permission.

$$\delta = const\, F\left(\sqrt{W_0^2 / aL}\right) Q(\mu_0), \tag{18}$$

μ_0 is defined in terms of the work function Φ and Fermi energy E_F as $\mu_0 = \sqrt{(E_F + \Phi) / E_F}$. W_0 is the initial kinetic energy of the primary particles and due to energy losses over distance z, it is reduced at the rate $dW / dz = -a\, z$. L is the diffusion length of secondaries. Functions F and Q are defined as follows:

$$F(x) = e^{-x^2} \int_0^x e^{t^2} dt, \tag{19}$$

$$Q(\mu_1) = \int_{\mu_1}^{\infty} \frac{\mu - \mu_0}{(\mu^2 - 1)^2} d\mu, \tag{20}$$

The quantity δ denotes the total yield of secondary electrons. The dependence of δ on the energy of incoming electrons, W_0, together with experimental data for selected materials is shown in Figure 27. Few secondaries are generated for very low values of the kinetic energy of the primaries. There is limited amount of data published on the secondary-electron yield induced by positrons. To get a rough estimate on the numbers, I am including the data for electron-induced emission. The yield is slightly lower for positron-induced process.[68] The experimental values of the maximum yield, δ_{max} , and the corresponding energy of the primary particles, W_{0max} , are shown in Table III for selected elements and compounds.

Reproduced with permission of the copyright owner. Further reproduction prohibited without permission.

Table III. The total yield of the secondary electrons reaches the maximum value of δ_{max} at the energy of the incident electron of $W_{0\,max}$ (from Dekker[69]).

Specimen	δ_{max}	W_{0max} *(eV)*
Be	.5	200
Al	.95	300
Cu	1.3	600
Ta	1.3	600
Si	1.1	250
Ge	1.15	400
BaF_2	4.5	-
NaCl	6.8	-

The total maximum yield is close to unity for metals and higher for insulators. The maximum yield occurs at several hundred volts. The significance of the data presented in Table III and in Figure 27 on the construction of the lifetime spectrometer manifests in the dependence of the count-rate of the spectrometer on the sample and the energy of primary positrons. The lifetime spectrometer described in section 3.5.1 operates at positron energies between 1.1 keV and 70 keV. Within this range of energies, the count rate is expected to decrease with the increase of the energy of the primaries.

The distribution of the energy E_s of the secondary electrons is:

$$\frac{dP}{dE_s} = -\frac{(\mu_0^2 - 1)(\mu_1 - \mu_0)}{2\Phi\mu_1(\mu_1^2 - 1)^2 Q(\mu_0)}, \tag{21}$$

Reproduced with permission of the copyright owner. Further reproduction prohibited without permission.

where $\mu_1 = \sqrt{\mu_0^2 + (\mu_0^2 - 1)^{E_s}/_{\Phi}}$. The energy distribution of the secondaries induced by primary electrons calculated from equation 21 and the experimental distribution for

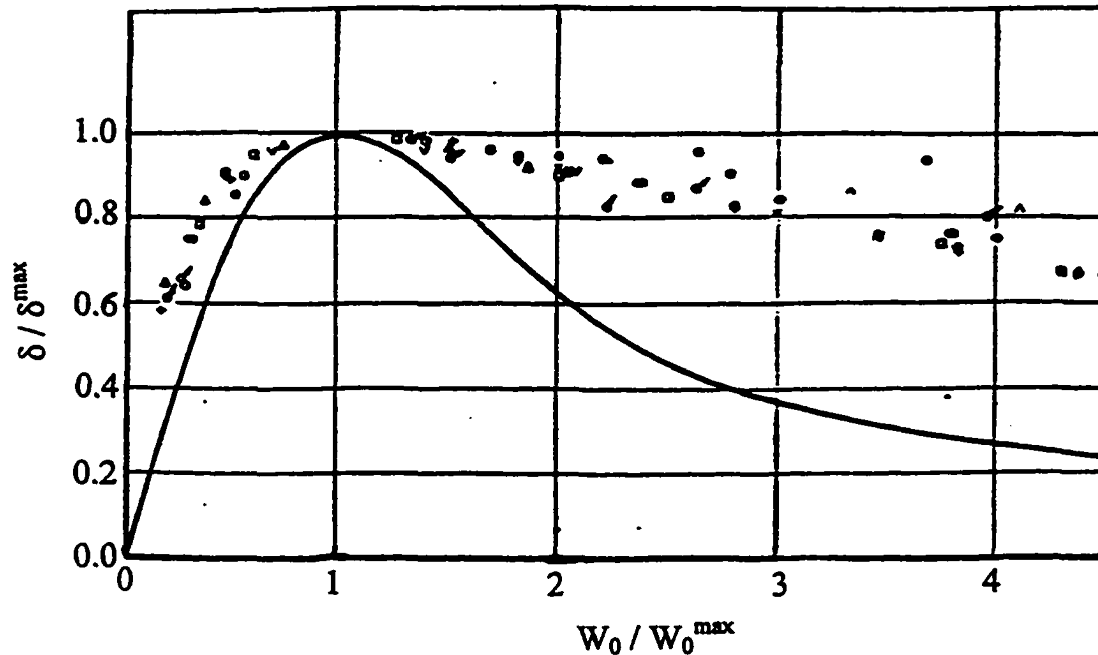

Figure 27. The theoretical (line) and experimental (symbols) dependence of the yield of the secondaries on the energy of the primary electrons in selected targets (Cu, Ni, Li, Ti, Mo, Pt, Al, Mg, Fe, Rb, B, Ge and Si). The yield is normalized to the maximum value and is expressed in terms of the energy normalized to the energy corresponding to the maximum yield. After Baroody.[67]

selected metals are plotted in Figure 28. The distribution is plotted in terms of the energy normalized to the material work function ($\varepsilon = E_s / \Phi$). No secondary electrons are emitted below the work function of the material, i.e. below $\varepsilon = 0$. There is an emission maximum at the energy close to the work function. At higher energies, the energy of the primary particle is distributed into the energy of the secondary electrons. The more secondaries, the less energy per electron is available. Hence, the reduction of the number of the emitted electrons with the increase of their kinetic energy. The distribution of the energy

Reproduced with permission of the copyright owner. Further reproduction prohibited without permission.

of the secondaries peaks between 1.5 to 5 eV and FWHM varies from 5 to 10 eV. The energy of the secondaries varies from zero to a few tens of eV. If the secondaries were to travel from the sample to the detector at the speeds corresponding to the emission

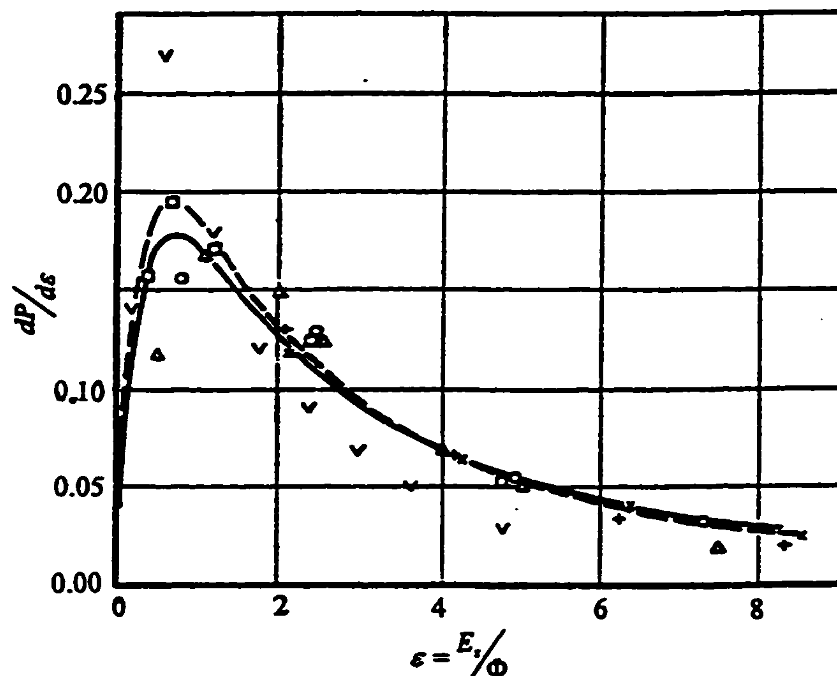

Figure 28. The energy distribution of the secondary electrons. The energy is normalized to the work function Φ of the material. The theoretical lines were calculated according to equation 21 using the values of μ_0^2 of 1.6 (solid) and 2.0 (dashed). The experimental values for selected metals (Au, Ag, Cu and Mo) are included. From Baroody.[67]

energy, the spread of the time of flight would be tens of nanoseconds wide. To reduce the spread, the secondaries are accelerated to higher energies in both designs of the lifetime spectrometer.

Little data for positron-induced emission are available. Yung *et al* found almost no difference between the energy distributions of 375 eV positron- and electron-induced secondaries emitted from Ge(100).[70]

Reproduced with permission of the copyright owner. Further reproduction prohibited without permission.

The angular distribution of secondary electrons is:

$$\delta(\theta) = \delta_0 \cos(\theta), \tag{22}$$

The angle of emission θ is measured from the normal to the surface. The cosine dependence comes from the increase of the path an electron needs to travel when the direction is not normal to the surface. Emission of secondaries into the whole half space means that the cross section of the beam of the secondaries is larger than of the primary beam of positron.

3.4.3 Backscattered positrons

A high level of the background limits the reliability of the data analysis, making it especially difficult to identify defects at low concentrations. The background is primarily caused by counts related to backscattered positrons. Although a positron that is backscattered from the sample does not annihilate there immediately, it may create secondary electrons. These electrons start the lifetime clock. The clock is stopped when the backscattered positron annihilates. The annihilation may take place at the sample if the positron comes back to the sample or at other parts of the chamber. In either case, such an annihilation event is delayed compared to the event of primary positron annihilating inside the sample. The delayed counts incorrectly mimic longer positron lifetimes in the sample.

A rough estimate of the background level can be obtained from the total number of backscattered positrons, η. It depends on the atomic number Z of the sample and the energy of incident positrons. The dependence for 35 keV incident positrons is plotted in Figure 29.[71] An increase in Z causes η to increase. This is because elastic scattering cross

Reproduced with permission of the copyright owner. Further reproduction prohibited without permission.

section of a positron increases with the increase of Z. Consequently, more positrons are forced to go back towards the surface and escape. Considering the design of the lifetime

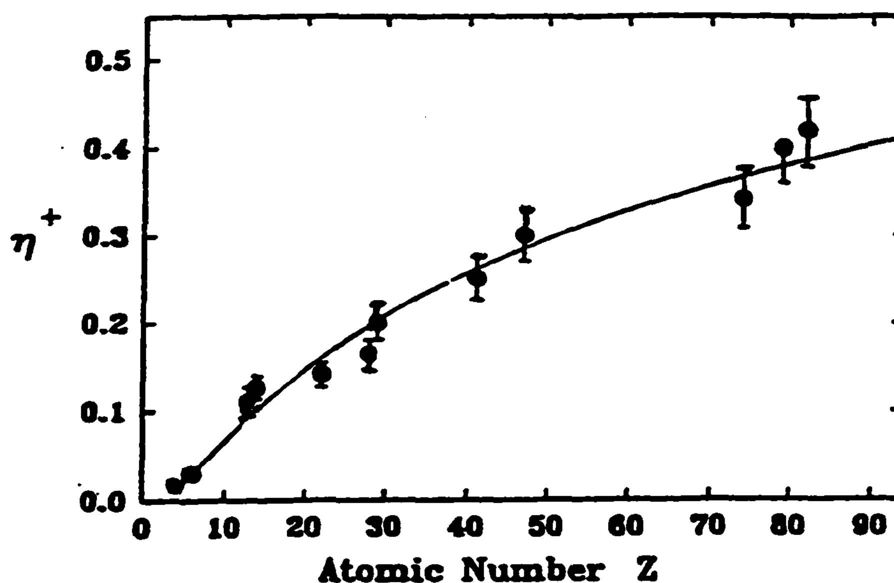

Figure 29. The total yield of the backscattered positrons increases with the atomic number of the target. Incident positrons of the energy of 35 keV were used. From Massoumi *et al.*[71]

spectrometer, one would be tempted to say that backscattered-positrons related background in the lifetime spectrum goes down with a reduction of Z. It is not necessarily true. The yield of secondary electrons is also reduced for low Z. The ratio of peak to background in a lifetime spectrum, proportional to δ/η, remains approximately independent on Z.

Baker and Coleman measured the relation between the energy of incident positrons, E_0, and η in Al, Cu, Ag and W targets.[72] η was found almost independent on E_0 between .5 keV and 30 keV. Although positrons of higher energy can penetrate the specimen much deeper, high-energy positrons directed back to the surface experience

Reproduced with permission of the copyright owner. Further reproduction prohibited without permission.

much less energy loss than low-energy ones. The variations in the energy-loss mechanism of the particles traveling back to the surface compensate the changes in the distance they need to cover. Therefore, the probability of reaching the surface and escaping as backscattered positrons is similar for both low- and high-energy primaries.

For normal incidence, the angular distribution of backscattered positrons follows the cosine law. This is not the case of a tilted sample and the distribution of the emission angles is peaked along the direction of the specular reflection.

The energy of the backscattered positrons influences their trajectories and, therefore, the landing position. The backscattered positron most likely annihilates at its landing spot. It may backscatter again, though. The probability of the detection of the annihilation event depends on the square of the inverse of the distance to the gamma detector. Therefore, the knowledge of the energy distribution of backscattered positrons is helpful in understanding the background function in the lifetime spectrum. Massoumi *et al* measured the energy of 35 keV positrons backscattered from Au target at various scattering angles,[71] see Figure 30. It is evident that majority of the positrons loose energy during the scattering process. The most probable energy of backscattered positrons is a function of the emission angle. Expecting similarities in the case of primary electrons and positrons, I am quoting some data for electrons. The distribution for several targets for 30 keV incident electrons at 45° take-off angle was published by Bishop[73], see Figure 31. The distribution for heavy elements, e.g. Au, exhibits strong elastic scattering peak while for low Z targets, e.g. C, inelastic scattering dominates. This behavior is a consequence of the variations of elastic scattering cross sections. For collisions with heavy elements, angles of elastic scattering close to 180° are likely. This is not the case of low-*Z* targets.

Reproduced with permission of the copyright owner. Further reproduction prohibited without permission.

Consequently, positrons in low-Z targets need to undergo much more elastic collisions than in low-Z materials. This increases the total path the positrons need to travel before escaping the specimen. When the path is long, the inelastic scattering begins to dominate. This is seen for low-Z materials. The data for electrons[73] and positrons[71]

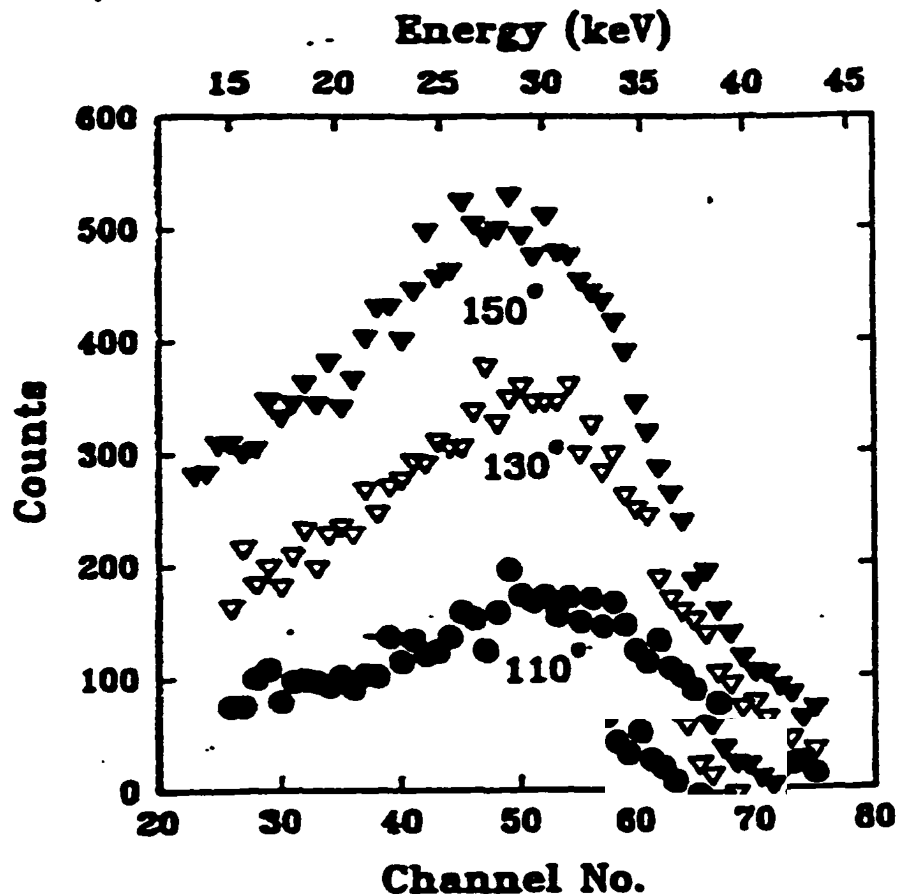

Figure 30. The energy distribution of positrons backscattered from gold (normal incidence, 35 keV primaries) at several take-off angles. After Massoumi *et al.*[71]

backscattered from gold can be compared. The distributions are similar, although the elastic peak is more pronounced in the case of electrons.

Reproduced with permission of the copyright owner. Further reproduction prohibited without permission.

The element-dependent distribution of the energy of backscattered positrons results in element-specific shape of the background function of the lifetime spectra. The broad distribution found for light elements implies increased values of the background level. This is because reduction of the energy of the backscattered positrons translated into their increased ability of being repelled back to the sample by the electric field in the lifetime spectrometer. The efficiency of the collection of annihilation radiation of the backscattered positrons annihilating at or near the sample is higher than in the case of the annihilation at a remote point of the chamber. This is reflected in a high level of background.

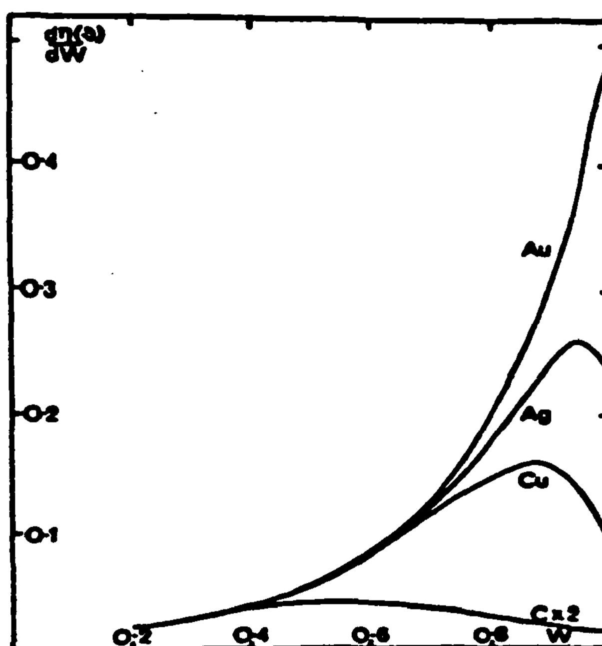

Figure 31. The energy distribution of the backscattered particles strongly depends on the target. For high-Z materials, the elastic-scattering peak is seen. The peak disappears for low-Z materials. The data was measured for 30 keV incident electrons at 45^0 take-off angles. From Bishop.[73]

Reproduced with permission of the copyright owner. Further reproduction prohibited without permission.

3.5 The designs of the present work

I designed and constructed two systems measuring positron lifetime on a variable-energy positron beam. Both systems were mounted on a magnetically-guide beam. Design #1 was more successful than #2. Design #2 was based on a newly developed idea. It was abandoned after extensive testing. Design #1 was applied to analyze films of low dielectric constant, intended for use in integrated circuits of the next generation.

3.5.1 Design #1, ExB deflector type

3.5.1.1 Description of the system

The schematic of the system is shown in Figure 32. The uniform magnetic field, 50 Gs, is applied antiparallel to the direction of the motion of the positrons in the beam. The field makes the positrons move in a spiral motion and prevents the beam from diverging. Positrons pass through the aperture biased at +600 V and through E×B filter.[74] Next, the positrons hit the sample and annihilate there. One of the annihilation gamma rays is detected in the BaF_2 scintillator coupled to a photomultiplier tube. The signal from the PMT stops the clock measuring the lifetime of positrons. Most positrons injected into the sample trigger emission of one or more secondary electrons. These electrons are accelerated to the energy of about 600 eV. In the E×B filter ($E_{\perp}$ = 80 V/cm, $B_{\parallel}$ = 50 Gs), the electrons are deflected from the trajectory of the positrons. A set of micro-channel plate detectors is placed to intersect the stream of secondary electrons. The pulse from this detector stops the positron-lifetime clock.

Reproduced with permission of the copyright owner. Further reproduction prohibited without permission.

The secondary electrons generated by positron entrance into the sample do not have a well-defined kinetic energy nor emission angle. The kinetic energy ranges from 0 to about 30 eV and all emission angles are possible. The time of flight of such electrons

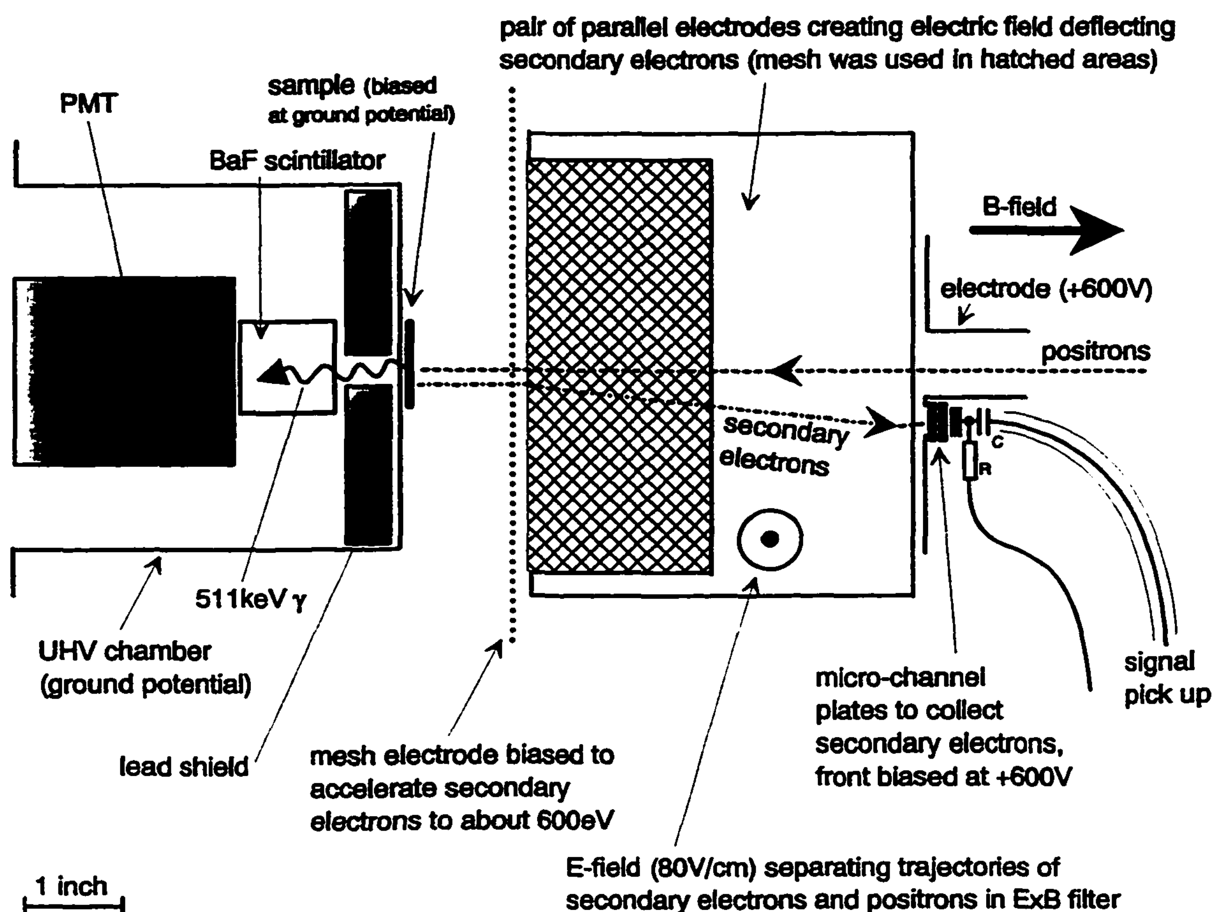

Figure 32. The schematic diagram of the variable-energy positron lifetime spectrometer using the secondary electrons to start the lifetime clock (design #1). The trajectories of the secondaries are separated from the trajectories of the incident positrons in the E×B filter, see text for details.

would vary by tens of nanoseconds. Depending on the sample, positron lifetimes vary from about 90 ps to 140 ns. The spread of the measured time intervals (tens of ns), caused by variations of the time of flight of the secondary electrons, would make the system

Reproduced with permission of the copyright owner. Further reproduction prohibited without permission.

useless. To reduce the spread of time, the secondaries are accelerated in electric field. The potential gradient of +600 V is applied between the sample (0 V) and the accelerating electrode (+600 V). When the electrons carry higher kinetic energy, their total time of flight and its spread are significantly reduced.

The annihilation rays pass through a small opening in the lead shield. The shield reduces the intensity of the annihilation radiation of the backscattered positrons. Some positrons, instead of promptly annihilating at the sample, backscatter from the sample. Due to the presence of retarding electric field, they may return to the sample or its vicinity. Gammas from some of these backscattering events are stopped in the shield.

The electrode accelerating the secondary electrons and the electrodes of E×B filter are partially made of a high-transmission mesh to reduce the possibility of the annihilation of the backscattered positrons at these electrodes. Due to the small spacing between the electrodes and the scintillator, many of the gammas from annihilation at the electrodes would reach the scintillator. Instead, most of them pass through the mesh and annihilate far away.

The system was tested for the incident positron energies between 1.1 keV and 50 keV. At these energies, the deflection of the positron trajectories in the E×B filter is small. Nevertheless, it is non-negligible below about 2.5 keV. The shift of the trajectory adds to the shift of the trajectory of the secondary electrons. This makes the separation between positron and electron paths bigger. To compensate for this effect and to make sure the beam spot at the sample does not move with the positron energy, the incident positron beam is steered with a set of magnetic deflection coils (not shown).

Reproduced with permission of the copyright owner. Further reproduction prohibited without permission.

The value of the electric potentials, the magnetic field and the geometrical dimensions of the system were optimized in a series of computer simulations. The simulations were performed using Simion 6.0 program[75] and are described in sections 3.5.1.3 and 3.5.1.4.

3.5.1.2 Experimental

BaF_2 scintillator coupled to a PMT was selected to detect annihilation gamma rays. BaF_2 cylindrically shaped (1"×1") scintillator was chosen. This is one of the fastest scintillators available and because it is made of high Z material ($Z_{Ba} = 56$) its efficiency to gamma collection is very high. Only plastic scintillators are faster but their efficiency is much lower. Light output of BaF_2 consists of two components: fast (600 ps decay constant) and slow (630 ns). The fast component emits light of the wavelength of about 220 nm, while the slow one – 310 nm. To allow transmission of the scintillating light to the photocathode of the PMT, UV-transparent optical grease (100,000 viscosity, manufactured by General Electric[76]) was used to couple the scintillator to PMT. The scintillator was wrapped with a Teflon tape to reflect the light at the walls. Such procedure is commonly used to increase the light output. Increased light output makes the gamma detector respond faster. This is because when the number of emitted photons is large, each pulse, considered as a histogram of counts vs. time, has a very well defined rising edge.

The Hamamatsu PMT, model R3386, was used.[77] It is a very fast PMT, 2.1 ns rise time and 0.4 ns transit time spread (TTS). It uses fine mesh dynodes, which make it insensitive to the magnetic field of up to several hundreds Gs. In the lifetime spectrometer, the PMT is required to operate in 50 Gs magnetic field and this is within

Reproduced with permission of the copyright owner. Further reproduction prohibited without permission.

the specifications of the R3386 PMT. The photocathode is made of synthetic silica and is sensitive to light wave lengths from about 180 nm up, i.e. it is capable of responding to the fast component of the BaF_2 scintillator.

The timing properties of the scintillator coupled to the PMT were measure using γ-γ coincidence from ^{60}Co source. A similar BaF_2 scintillator coupled to an XP2020Q PMT was used to detect the second gamma. The FWHM was found 300 ps. The ratio of peak to background was over 1000. Assuming similar timing resolutions of the two detectors, the FWHM of a single detector was $\sqrt{2}$ times lower, i.e. 212 ps. The gamma energy of ^{60}Co, 1.33 MeV, is higher than of the annihilation rays, 511 keV. Therefore, the FWHM is larger at 511 keV. Based on the comparison data published by Laval *et al*,[78] the FWHM of the detector at 511 keV is estimated as 290 ps.

A set of two micro-channel plates was used to detect secondary electrons. Micro-channel plates are very fast, have high gain and work well in magnetic fields. These features make them ideal for the system. Efficiency of the collection of electrons depends strongly on the energy of the particles. In the lifetime spectrometer, electrons of 600 eV energy hit the channel plates. At this energy, the efficiency is about 70 %.[79] Micro-channel plates are almost insensitive to gamma rays.

The channel-plates detector was custom made to reduce the dimensions to fit the geometric requirements of the system. AC coupling, not DC coupling was used in order to float the front of the channel-plates detector at +600 V, the potential required by the design. A small ceramic capacitor and an anode-biasing resistor (1 MΩ) were mounted directly at the anode to avoid signal reflections at a non-matching line impedance. The resistor was used to eliminate noise pickup by not-shielded connection to high-voltage

Reproduced with permission of the copyright owner. Further reproduction prohibited without permission.

power supply. A channel-plates pulse free of reflection, with 670 ps rise time, was obtained.

The time response of the detector of the secondary electrons was not measured. Nevertheless, the FWHM of the time-response function is believed to be much smaller than of other sources of the timing uncertainty. It is neglected hereafter.

The ground and AC-power connections were carefully custom-designed to minimize noise pick up.

The beam spot at the sample was checked with another set of micro-channel plates and a phosphor screen. For this test, the detector well with the PMT and the scintillator had been temporarily removed. The spot was teardrop-shaped with 5 mm × 7 mm dimensions. These dimensions determine the minimum size of a measurable sample. If a smaller sample were installed, some positrons would annihilate at the UHV chamber. The non-circular shape is believed to be due to the distortions of the beam cross-section in the E×B filter of the positron source chamber. It is, therefore, independent on the lifetime spectrometer.

The schematic of the electronic part of the time-interval measuring system is shown in Figure 33. The signal from the secondary electrons collected in the micro-channel plates detector is amplified in a modified preamplifier (Ortec 9306)[80]. The precise timing of the pulse is determined in the pico-timing discriminator (Ortec 9307). The pulse from the discriminator starts the measurement of the positron lifetime in the time to amplitude converter (TAC). The stop of the lifetime measurement comes from the PMT and is processed in the Ortec 583 constant fraction discriminator (CFD). The pulse

Reproduced with permission of the copyright owner. Further reproduction prohibited without permission.

of the amplitude proportional to the positron lifetime is converted to the digital form and stored in the multi channel analyzer (MCA) situated inside the computer.

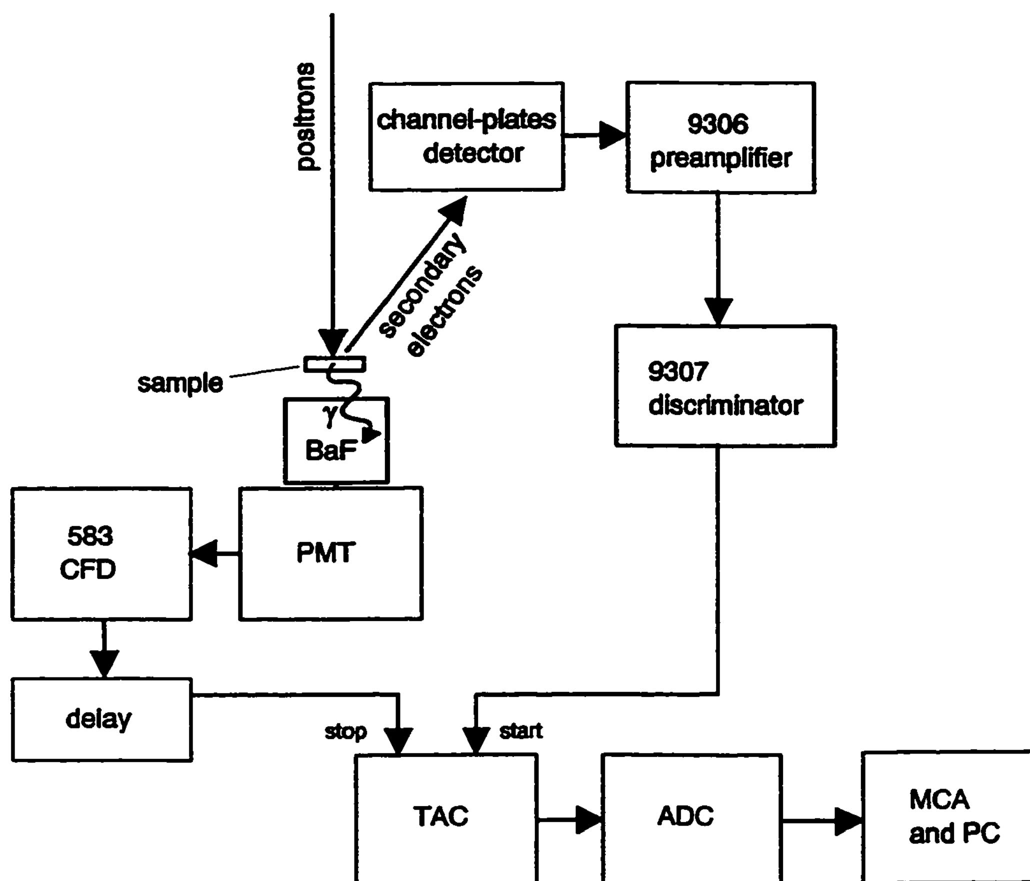

Figure 33. The schematic of the electronic part of the positron lifetime spectrometer.

3.5.1.3 Influence of the spread of the time of flight of secondary electrons on the time resolution: simulations and experiment

The motion of secondary electrons can be simulated provided the knowledge of the initial parameters (position, speed and emission direction) is accurate enough. A series of computer simulations were performed before building the system. Doing so allowed optimizing the geometry and fields for the best performance.

Reproduced with permission of the copyright owner. Further reproduction prohibited without permission.

First, it was confirmed that the primary beam of the positrons would reach the sample. The beam of circular cross section of 4 mm in diameter was transferred to the sample without noticeable distortions. Subsequently, the secondary electrons were randomly emitted out of a 4 mm in diameter spot at the sample. The initial energy was randomly selected with the aid of a random number generator obeying the probability distribution given by equations 21. The following parameters were used: the maximum initial energy = 30 eV, $\mu_0^2 = 2$ and $\Phi = 2$. These values mimic the experimental energy distribution of the secondary electrons emitted from a Si target. The emission angles were selected randomly to satisfy the cosine law (equation 22). 10000 trajectories were simulated.

The histogram of the time of flight of the secondary electrons is shown in Figure 34. Two time axes are used. The top one indicates absolute time of flight of the secondaries. The bottom one shows lifetime of positrons. The two axes are mirror-reflected because shorter time of flight of the electrons mimics longer positron lifetime. The position of the zero in the bottom axis is arbitrary. It was selected at the maximum of the plots. The plots are normalized to the maximum value of one. The average time of flight was about 10.4 ns and its spread was characterized by FWHM of 370 ps. The peak turned out to be slightly asymmetric. The perfect time of flight would be described by the Dirac delta function. The smearing of the left-side edge is mainly caused by the low-energy fraction of secondaries as well as by the angles of emission being far from normal to the sample surface, see Figure 28 and equations 21 and 22. High-energy secondaries shape the right-side edge of the timing resolution function. The spread of the time of flight is a major source of smearing of the timing resolution of the system, but not the

Reproduced with permission of the copyright owner. Further reproduction prohibited without permission.

only one. To incorporate the broadening of the timing resolution due to non-perfect time response of the gamma detector, the time of flight of the secondaries was convoluted with the timing resolution of the gamma detector. A Gaussian, FWHM of 290 ps, was used, see section 3.5.1.2. The convoluted computer-simulated timing resolution is plotted in Figure 34. Also shown is the experimentally found resolution function obtained from

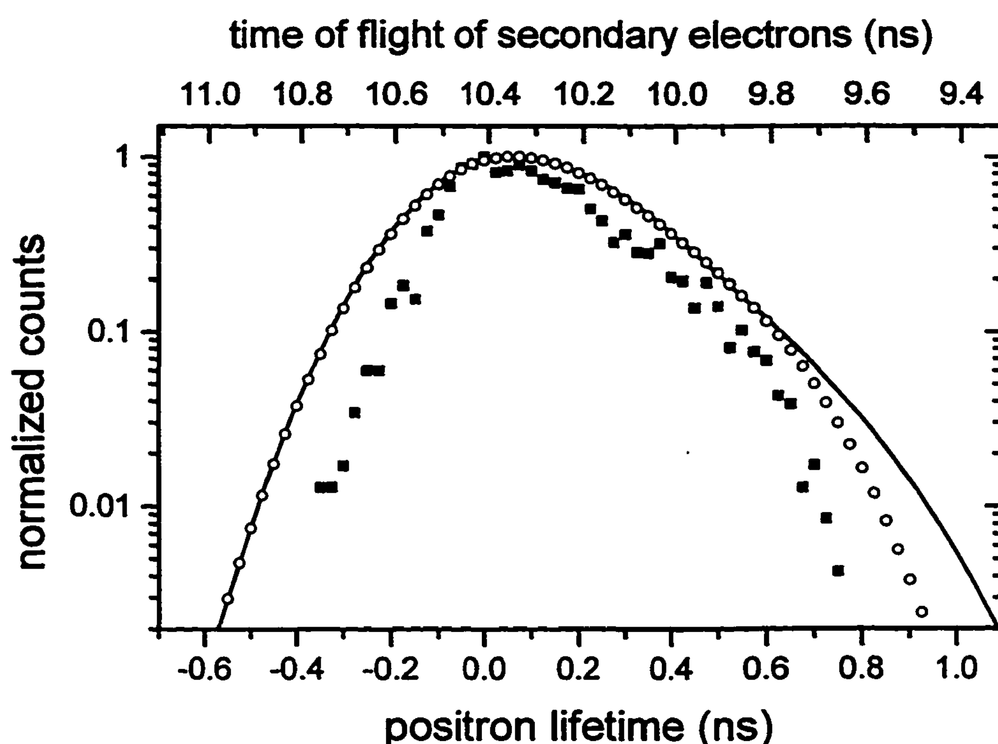

Figure 34. The comparison of the experimental and simulated resolution function of the lifetime spectrometer. The experimental resolution (line) was determined through the fitting of the spectrum of the Si divacancy, see section 3.5.1.5.2. The combined simulated resolution function (open circles) was obtained through the convolution of the time of flight of the secondary electrons (solid squares) with the time response of the gamma detector, see text. The two time axes are mirror-reflected because a shorter time of flight of the secondaries mimics a longer positron lifetime.

Reproduced with permission of the copyright owner. Further reproduction prohibited without permission.

the fit of the positron lifetime in Si divacancies. Two asymmetric Gaussian-like functions were used for the fit and the details will be described in section 3.5.1.5.2. The background level was not incorporated in the plots in Figure 34 because it is believed to be determined by the backscattered positrons, see section 3.5.1.4. The agreement between the computer-simulation and the fit to the experimental data is very good in the central and left-side part of the peak. For shorter times of flight of the secondaries, the computer simulation is an underestimate. Possibly, it is due to the 30 eV high-energy cutoff of the energy distribution of the secondaries, which was imposed in the computer simulations. It is interesting to note the asymmetry of the timing resolution predicted with the computer simulations and confirmed experimentally. A complete simulation of the resolution function should take into account the smearing of the timing response of the detector of the secondary electrons. It is believed to be small compared to the smearings already analyzed.

A slightly different shape of the timing resolution should be anticipated for samples made of a material other than Si. μ_0 and Φ are material-specific parameters which modify the energy distribution of the secondaries.

The landing spots of the secondaries on the plane normal to the primary beam (z-y) are shown in Figure 35. The emission spot is plotted, too. The landing points form a circle with smeared edges. The edges are smeared because of the random selection of the emission angles, which shift the trajectories in z-y plane. The center of the landing spot is shifted by about 11 mm from the center of the emission spot. This is an anticipated result of the shifting action of the E×B filter. The shift is large enough to completely separate the primary beam of positrons from the beam of secondary electrons. There is enough

Reproduced with permission of the copyright owner. Further reproduction prohibited without permission.

separation to accommodate a few-millimeters wide holder of the micro-channel plates detecting the electrons.

A few landing spots are visible around y = 14 mm and 26 mm. These are the secondary electrons landing on the thick edges of the electrodes of the ExB filter. These

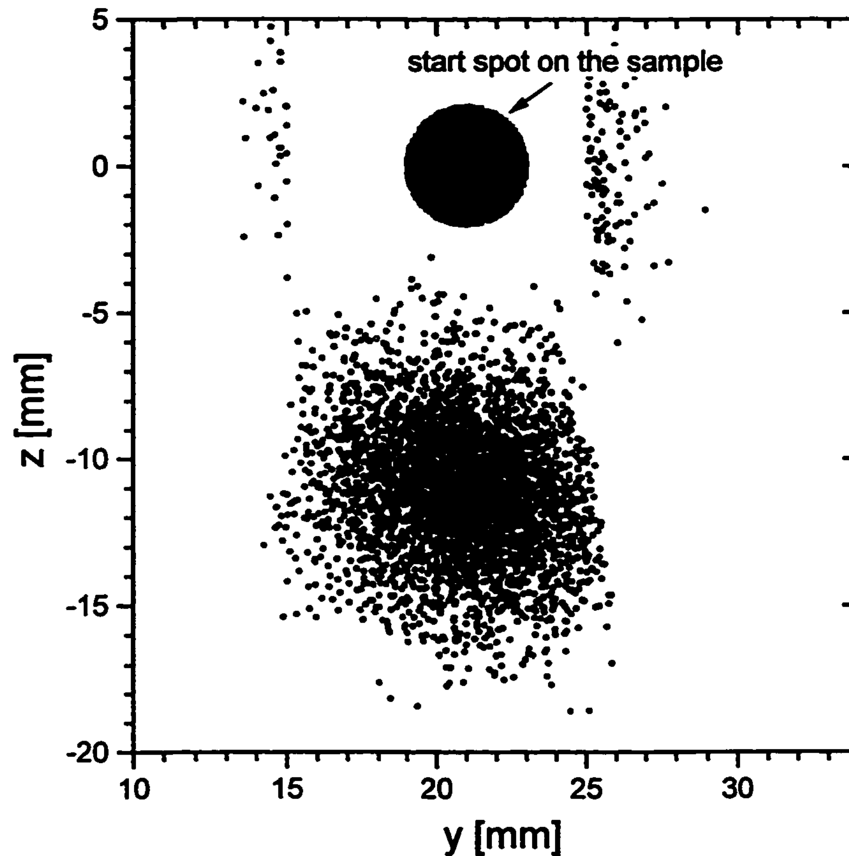

Figure 35. The simulation of the landing spot of the secondary electrons in the plane of the detector of the secondaries. The landing spot is shifted from the emission spot on the sample (shown at the top) due to the action of ExB filter. The shift of the two spots allows guiding the primary beam of the positrons to the sample without hitting the detector of the secondaries.

Reproduced with permission of the copyright owner. Further reproduction prohibited without permission.

electrons do not create pulses in the micro-channel plates detector and can be discarded. They constitute a very low percentage and they do not reduce the system count rate by a measurable amount.

3.5.1.4 Background effects due to backscattered positrons: simulation and experiment

Computer simulations were used to investigate problems related to positrons backscattered from the sample. Some of these backscattered positrons hit solid parts of the chamber. They can annihilate there or backscatter again. The electric field in the system may deflect the backscattered positrons back onto the sample. These scenarios need to be considered to estimate the background of the lifetime spectrometer. The "Simion" program was used to simulate the effect of the positrons backscattering from the sample and annihilating upon meeting a solid surface. The subsequent backscattering events were not simulated and were considered as second-order effects. The simulation was intended to be valid for Si samples. Just like in the simulation of the secondary electrons, a random number generator was employed to simulate the values of the emission angles and energies. The distribution of the emission angles was constrained to obey the cosine law. The energy distribution was approximated by function $P(E)$ defined as:

$$P(E) \propto \sin\left(\left(\frac{1.7E}{E_0}\right)^2\right), \tag{23}$$

where E_0 is the energy of positrons shot onto the sample. The efficiency of the backscattering process was assumed 30 %.[81] The probability of detection of a gamma ray

Reproduced with permission of the copyright owner. Further reproduction prohibited without permission.

from the annihilation of the backscattered positron depends on the distance between the scintillator and the annihilation spot. The reduction of the probability with the distance was included by applying the distance-dependent weight factor to each simulated event.

The histogram of the simulated time of flight of the backscattered positrons is shown in Figure 36(a). In this simulation, the lead shield between the scintillator and the sample was omitted (see Figure 32). The scintillator was placed directly behind the sample. The histogram of the time of flight of the secondary electrons is also plotted. The plots of the time of flight of secondaries and backscattered positrons were normalized to the same number of events. In addition, the plot describing the backcattered positrons was scaled down to include 30 % yield. The plot describing the secondary electrons was not scaled. This is because the secondary electrons need to be collected in order to detect both the direct positron annihilation and the annihilation of the backscattered positrons. Comparison of the plots allows estimating the magnitude of the problems related to backscattered positrons. The histograms corresponding to primary positrons of the energy of 2 keV and 4 keV are plotted. Majority of the simulated counts originates from the backscattered positrons, which are reflected in the electric field between the sample and the accelerating electrode (see Figure 32) and land at or near the sample. The accelerating electrode was assumed perfectly transparent in this simulation. The annihilation at the other electrodes and the walls of the chamber has little importance. This is because the probability of gamma detection goes down with the increase of the distance between the annihilation spot and the scintillator. The level of background is higher for 2 keV primary

Reproduced with permission of the copyright owner. Further reproduction prohibited without permission.

positrons than for 4 keV ones. This is because positrons of higher energy are more likely

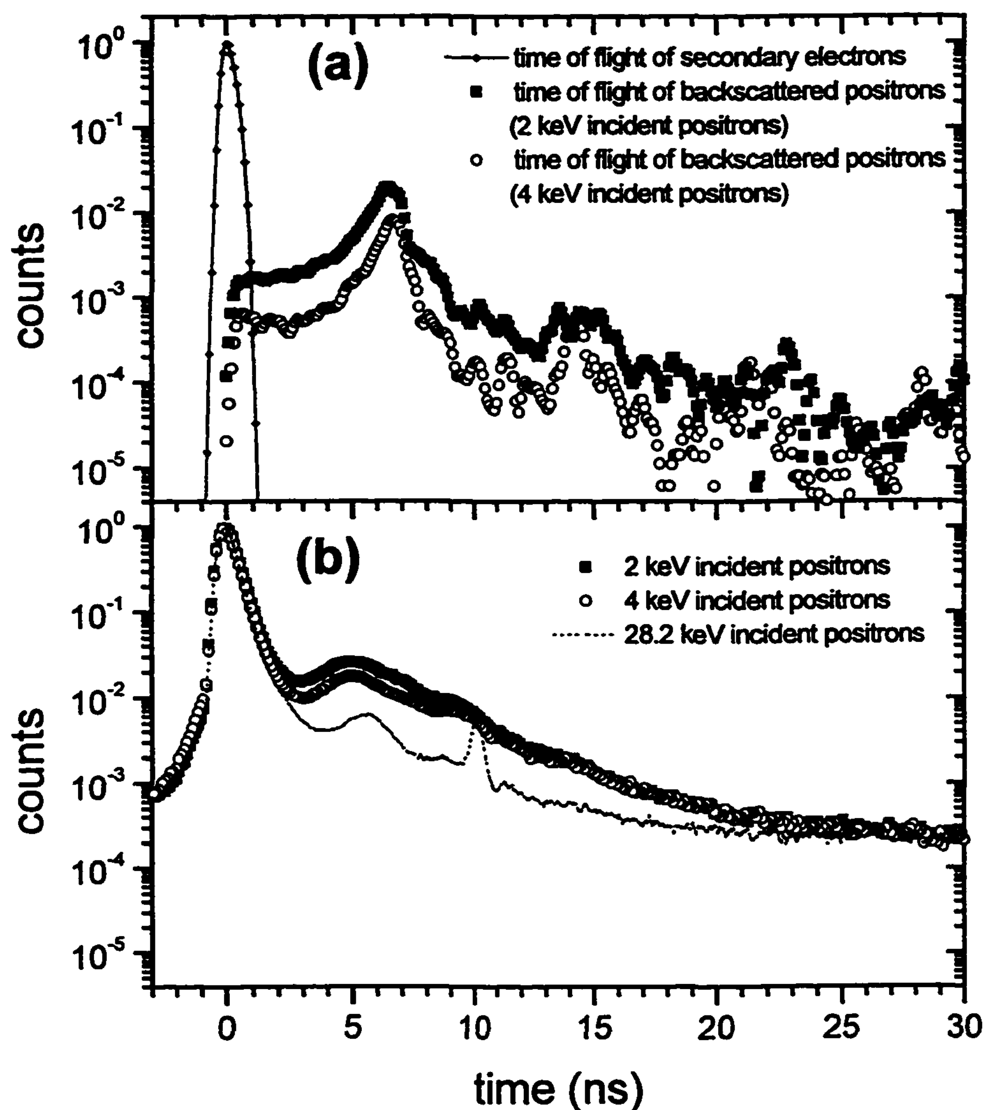

Figure 36. The simulated (a) and experimental (b) background due to the annihilation of the backscattered positrons, see text for the analysis. The simulations and the experimental data for various values of the energy of the incident positrons are shown.

to penetrate the retarding electric field, pass through the transparent accelerating electrode and annihilate far away.

Reproduced with permission of the copyright owner. Further reproduction prohibited without permission.

The backscattered positrons need to overcome only 600 V of retarding potential difference to escape from the sample permanently. In spite of higher initial energy (2 keV and 4 keV), many backscattered positrons do not escape. This is because of energy losses during the backscattering process. In addition, only the fraction of the kinetic energy corresponding to the momentum along the beam axis is used to overcome the retarding electric field. The level of background should dramatically go down when the energy of the primary positrons is large, i.e. tens of keV. 600 V of retarding field does not constitute a serious obstacle for particles of this high kinetic energy. Instead, they annihilate in more remote solid surfaces in the chamber. This was not simulated because of the difficulties in precision modeling of the potentials in a complicated chamber.

The simulated background function has an interesting structure. Several peaks can be distinguished: at about 6 ns, 15 ns, etc. Their origin can be understood when the background counts are plotted as a 3D histogram, as a function of both time of flight and the distance r between the annihilation spot and the center of the sample, see Figure 37. The peaks mentioned above are constrained to small values of r. It is proposed that these peaks reflect one or more full revolutions of the squeezed-spiral trajectory of the particles. Simulated shifts of the time occurrence of the peaks, due to variations of the magnetic field, support this hypothesis (not shown).

The experimental plots of positron lifetimes in Si are plotted in Figure 36(b). The data were collected without background-reducing lead shield, see Figure 32. The shape of the background in the experimental plots can be compared to the simulations (Figure 36(a)) for positron implantation energies of 2 keV and 4keV (the background-reducing lead shield was omitted in the simulations, too). The magnitude of the background is

Reproduced with permission of the copyright owner. Further reproduction prohibited without permission.

higher for the experimental data. The difference partially comes from the exponential decay of the annihilating positrons (positron lifetime decay) included only in the

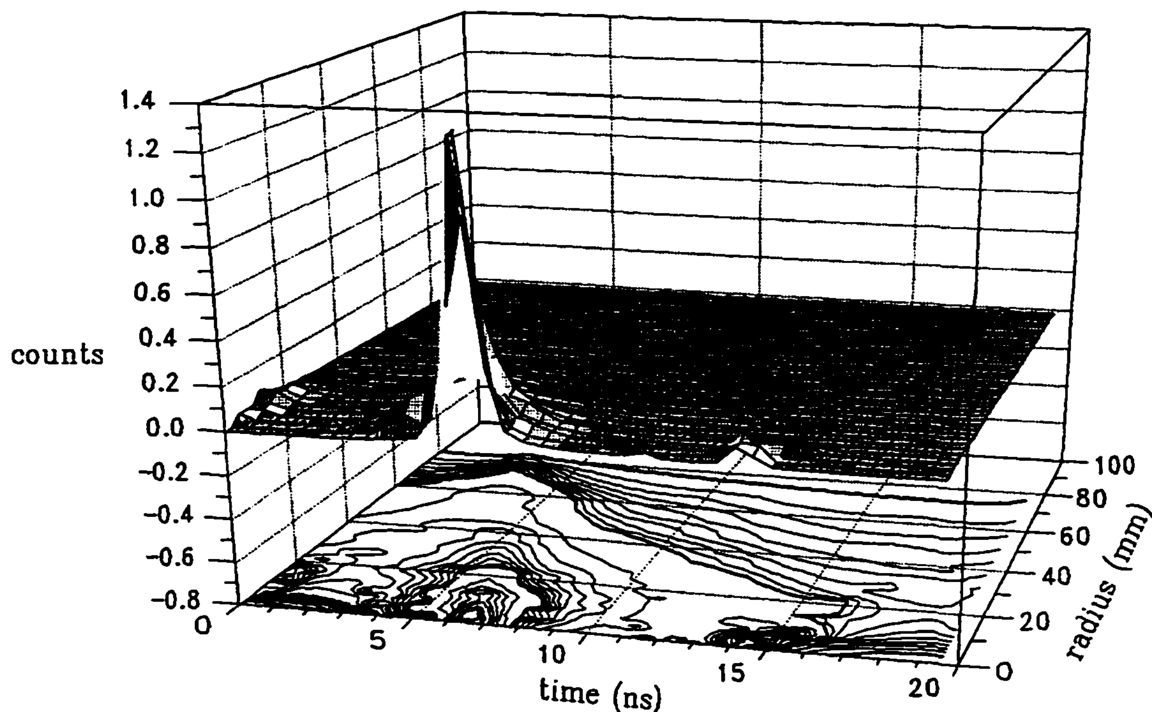

Figure 37. Many backscattered positrons return to the sample. The analysis of the simulated histogram of the counts vs. time and distance of the landing spot to the center of the sample allows to understand the structure of the background function in the lifetime spectra plotted in Figure 36, see text. The histogram was simulated for 4 keV incident positrons. The lines in the contour plot are arranged in the $\log_{10}$ order.

experimental data. Nevertheless, the envelope function of the background is similar. The background level goes down with the reduction of the positron implantation energy for both simulation and experiment. The experimental background for 28.2 keV positrons is much lower than for 2 keV and 4 keV positrons. This is because most 28.2 keV positrons

Reproduced with permission of the copyright owner. Further reproduction prohibited without permission.

have enough kinetic energy after the backscattering event to overcome 600 V of the retarding potential difference. Consequently, they annihilate far from the scintillator and few annihilation counts are observed.

Discrete peaks in the background are found in the simulation and the experiment. It might be possible to get rid of these undesired peaks: the secondary electron(s) created upon the second contact of the positron with the sample may be detected in the detector of the secondary electrons. Detection of the second pulse within a fixed interval of about 100 ns would discard the event from being analyzed. Double pulses were indeed observed on a digital oscilloscope. There is no standard nuclear NIM module capable of performing rejection of double-pulse events when the second pulse arrives only several ns after the first one. It is possible to custom-make such a system based on fast-ECL logic circuits manufactured by Motorola.[82] The system can be included in the lifetime spectrometer of the second generation.

Nevertheless, a careful inspection of Figure 37 reveals a way to reduce the background. Many of the backscattered positrons land far away from the center of the sample. Placement of a gamma-absorbing shield between the plane of the sample and the scintillator stops some of the annihilation rays. No event can be further processed unless a gamma ray is detected. Naturally, an aperture needs to be drilled in the shield to allow the annihilation rays from valid events to reach the scintillator. This shield was installed, see Figure 32. The experimentally found improvement of the ratio of peak to background for Si target is plotted in Figure 38. The discrete peaks in the background are still seen. This is consistent with the simulation. The discrete peaks originate form positrons returning to the center of the sample and annihilating there. There is no lead to stop them.

Reproduced with permission of the copyright owner. Further reproduction prohibited without permission.

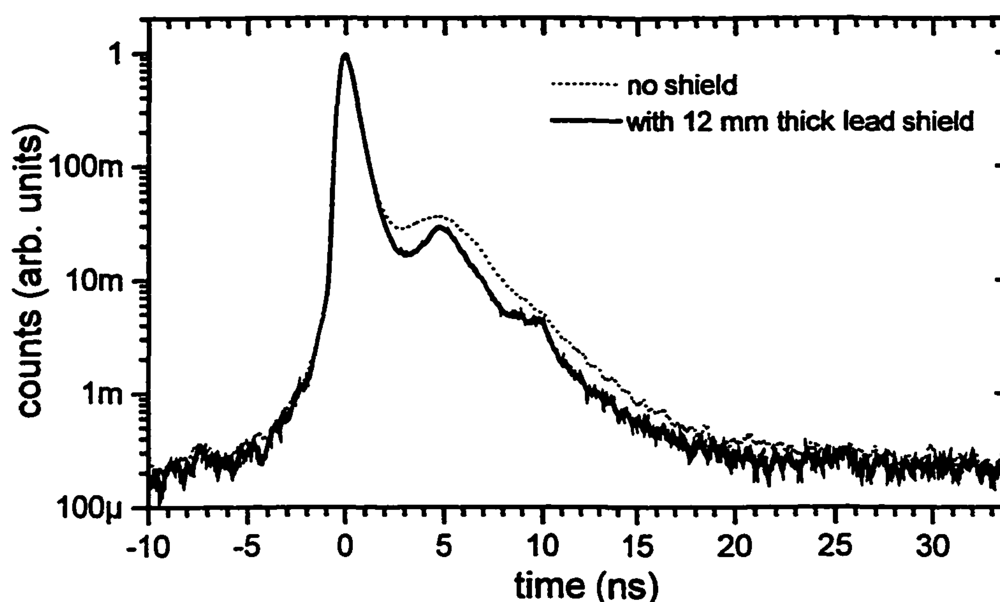

Figure 38. The background due to the annihilation of the positrons backscattered and returning to the vicinity of the sample can be reduced through the installation of a gamma-absorbing shield.

The mesh used in the construction of the electrodes is not 100 % transmitting. Some of the backscattered positrons may annihilate in the mesh. This scenario was simulated with the program. A broad peak in the background function appeared at times exceeding about 0.2 ns (not shown).

3.5.1.5 System test: positron lifetime in defect-free and defective Si

3.5.1.5.1 Brief review of selected published works on positron lifetime in Si

Many papers have been published on the lifetime of positrons in defect-free Si and in selected defects in Si. This is why Si specimens were selected to test the performance of the lifetime spectrometer. The positron lifetime in defect-free Si is well established as 220 ps.[83, 84] In undecorated Si monovacancy and divacancy positrons

Reproduced with permission of the copyright owner. Further reproduction prohibited without permission.

annihilate with the lifetimes of about 270 ps[85] and 320 ps[39], respectively. Variation between different charge states of the defects are typically less than 10 ps[39] and will be neglected hereafter. The theoretical values for undecorated Si vacancies were calculated by Puska and Corbel.[86] The theory agrees well with experiment. The lifetimes of selected foreign-atom decorated vacancies are known, too. Oxygen-monovacancy pair has the lifetime of 225 ps,[39] P-vacancy and Sb-vacancy complex: 250 ps and 270 ps, respectively.[33] There are some variations between the published values of the lifetimes at these defects but the variations do not exceed 10 ps.

3.5.1.5.2 Analysis

To test the reliability of the information extractable from the lifetime spectrometer described earlier, three samples were analyzed: defect-free Si, Si divacancy and large Si voids. Defect-free Si was measured in FZ Si(111), $\rho = 2$ kΩ cm, at positron implantation energy of 36.15 keV. Si divacancy was obtained from Si(111) irradiated with 150 keV ^{29}Si ions to the dose of 1×10^{15} cm^{-2}. S parameter in the layer was found about 1.035 consistent with the expected value of Si divacancy.[23] This is not the same sample containing divacancies used in the experiments described in section 2.3.1. The lifetime spectrum was measured at positron implantation energy of 4.0 keV. The positron diffusion to the surface can be neglected due to short positron diffusion length in the sample. The voids were obtained from LT-MBE Si sample analyzed in section 2.3.1 (void #1). Positron implantation energy was selected 3.6 keV.

The experimental lifetime spectra of the samples, together with the fits, are plotted in Figure 39. The position of the origin of the plotted time axis is arbitrary. It depends on the delay lines used in the system, response times, etc. All spectra have well

Reproduced with permission of the copyright owner. Further reproduction prohibited without permission.

defined lifetime peaks. The peaks are highly asymmetric because only the falling edge (i.e. positive lifetimes) contains the information about the positron decay. The background levels vary. The difference in the background between the spectrum of the

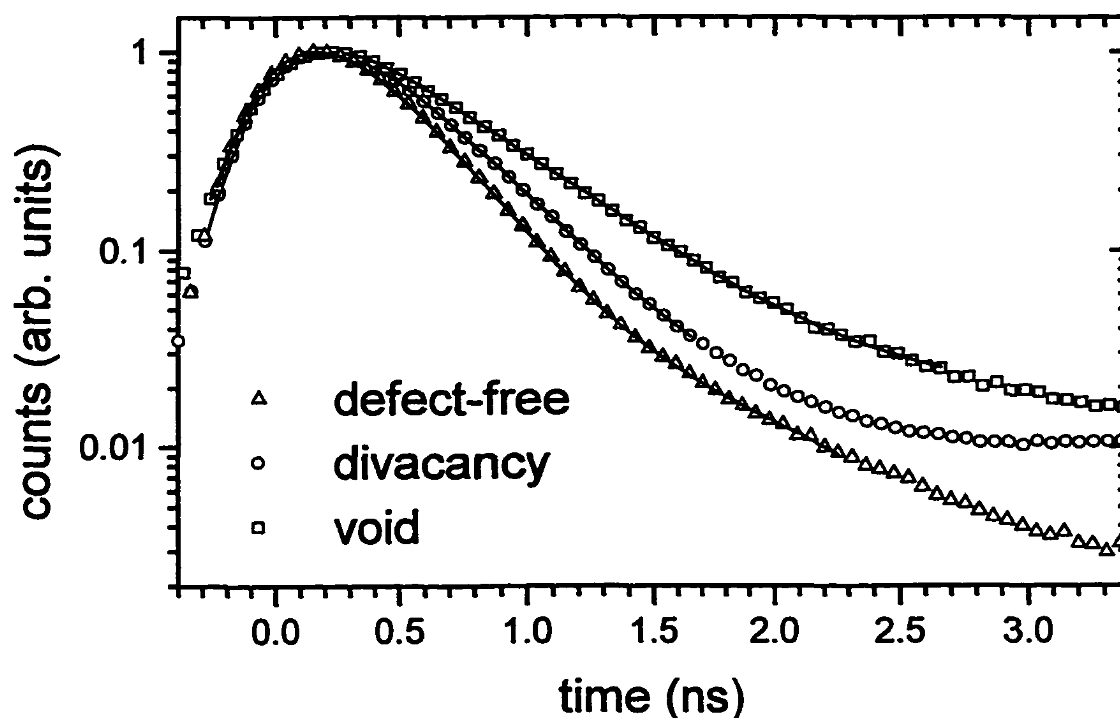

Figure 39. The experimental lifetime spectra of defect-free Si, Si divacancy and Si void (symbols) together with the fits (lines). The obtained lifetimes (235(16) ps for defect-free Si, 325(7) ps for Si divacancy and 500(70) ps for the void) are in agreement with the theoretical calculations and the experimental data found in literature. The spectra were normalized to the maximum value of 1 and shifted so that the dominating Gaussian of the resolution function is centered at 0 ns.

divacancies and the voids comes from system modifications. Only the former spectrum was collected with a background-reducing lead shield, see sections 3.5.1.2 and 3.5.1.4. The level of background of the defect-free Si spectrum is much lower than of the other two. This is because a much higher positron implantation energy was used (36.15 keV).

Reproduced with permission of the copyright owner. Further reproduction prohibited without permission.

At this high energy, few backscattered positrons come back to the vicinity of the sample and annihilate there. Influence of the annihilation at remote parts of the chamber is small due to decreased solid angle of radiation acceptance by the gamma detector.

The spectra were fitted using a custom-written dynamic link library (dll) executed from the nonlinear least square fitter provided in Origin 5.0 Professional graphic software.[87] The fitting function was written in C language and was a modification of the Fortran code supplied by Prof. Collins.[88] The fitting routine incorporates a sum of up to three exponential decays with the decay constant τ_i:

$$\sum_{i=1}^{3} \frac{f_i}{\tau_i} \exp\left(-t/\tau_i\right), \tag{24}$$

In one case, it was necessary to include an additional, shifted, exponential decay. The Physical justification will be discussed later.

This function is convoluted with the instrumental resolution. A sum of two asymmetric Gaussians was used, each defined as:

$$\frac{A_i}{w_i\sqrt{\pi/2}} \exp\left(\frac{-2(t-t_i)^2}{w_i^{\,2}}\right), \tag{25}$$

where:

$$w_i = \frac{w_l - w_r}{1+\exp\left((t-t_i)/s\right)} + w_r, \tag{26}$$

w_l and w_r are left- and right-side widths of the Gaussian, respectively, s was fixed as .01 ns. Constant background was added at the end.

The lifetimes fitted for the analyzed samples are listed in Table IV.

Reproduced with permission of the copyright owner. Further reproduction prohibited without permission.

Table IV. Lifetimes fitted from the experimental spectra for selected samples. The fitted parameters are defined in equation 24. NN entry denotes the parameter was not needed.

Sample	τ_1 (ps)	τ_2 (ps)	f_2
Defect-free Si	235(16)	NN	NN
Si divacancy	325(7)	NN	NN
Si void	200(500)	500(70)	0.85(25)

Only one lifetime component was needed to obtain a satisfactory fit of defect-free Si and Si divacancy. The lifetimes of 235(16) ps and 325(7) ps agree well with the values found in literature, i.e. 220 ps and 320 ps for defect-free and divacancy, respectively. The lifetime of the defect component of the sample with voids was 500(70) ps. This indicates at least 10 atoms were missing in the voids.[83] The lifetime of positrons in voids saturates at the maximum value of 500 ps, provided positronium does not form.[89] The lifetime found in the sample with void approaches the limiting value. For this reason, only the minimum size of the void can be estimated. The same sample with voids (void #1) was used in the Doppler broadening measurements. The lifetime and the corresponding size of the voids can be related to the ratio curve (see Figure 8) and the S parameter of 1.09. This is a useful result because the ratio curve of sample with void #1 can now be characterized with the size of the voids. 85(25) % of positrons in the sample with voids annihilate from voids, see coefficient f_2 in Table IV. The error bars are quite large, though. The value is consistent with the value found from 2D-ACAR analysis mentioned in section 2.3.1.2, i.e. 87(2) %.

Reproduced with permission of the copyright owner. Further reproduction prohibited without permission.

The fitted parameters of the resolution function are listed in Table V.

Table V. Parameters of the instrumental resolution fitted to the lifetime spectra of defect-free Si, Si divacancy and Si void. Some parameters should be considered in pairs, e.g. the ratio of the amplitudes of the two asymmetric Gaussians (A_1 / A_2) and their time shift ($t_2 - t_1$). The resolution function of defect-free Si contained an additional shifted decay, see text.

Sample	A_1	w_l^1 (ns)	w_r^1 (ns)	t_1 (ns)	A_2	w_l^2 (ns)	w_r^2 (ns)	t_2 (ns)	B
defect-free	5.8k (0.7k)	0.355 (.003)	0.47 (0.06)	21.02 (0.01)	0.6k (0.7k)	0.37 (0.15)	0.51 (0.14)	21.44 (0.18)	0
divacancy	11k (2k)	0.347 (.003)	0.45 (0.07)	21.07 (0.02)	1.3k (2k)	0.4 (0.4)	0.5 (0.3)	21.45 (0.3)	3.6k (0.4k)
void	2.9k (0.3k)	0.390 (.008)	0.41 (0.08)	10.03 (0.03)	0.38k (.28k)	0.27 (0.14)	0.47 (0.09)	10.37 (0.12)	1.00k (.15k)

The pair of asymmetric Gaussians fitted for each sample is almost independent on the sample. This indicates that the fitted lifetimes are meaningful. In the case of defect-free Si, an additional component of the resolution function was used. It was a decay (.15 ns time constant) shifted by 1.1(.2) ns from the origin of the primary lifetime decays and convoluted with another asymmetric Gaussian. This component mimics the annihilation of backscattered positrons on the copper mesh of the accelerating electrode, see Figure 32. The time shift of about 1 ns reflects the average time of flight of the backscattered

Reproduced with permission of the copyright owner. Further reproduction prohibited without permission.

positrons from the sample to the mesh. The component is needed only when the energy of incident positrons is high (36 keV here). At lower energies, due to retarding electric field, the majority of backscattered positrons return to the sample and its vicinity. This scenario can be modeled with flat background.

The system count rate turned out to be strongly dependent on the energy of the positrons. The dependence for positrons implanted into HF-etched Si(111) is presented in Table VI. The counts in the lifetime peak are listed. No lead shield was installed, see Figure 32. The count-rate with the lead shield installed is approximately 9 times lower. The reduction is caused by smaller efficiency of collection of annihilation gammas due to the increase of the distance between the sample and the scintillator. The reduction of the count rate with the increase of the energy of positrons is caused by a decrease of the yield of the secondary electrons generated at the sample. See section 3.4.2.2 for a review. The system count rate was found dependent on the sample. The count rate for Si covered with native oxide was about 40 % higher than for HF-etched Si. This is a consequence of increased yield of secondaries for oxides. Because secondaries are generated only in a layer extending from the surface up to several nanometers deep, it may be advantageous to coat selected samples with an insulating cap. The cap would have no significant effect on the lifetime spectrum. The increased yield of secondaries would increase the system count rate.

The positron beam count rate is about 80 kcps. The count rate of the lifetime spectrometer is much lower. Losses in the collection of the secondary electrons and non-perfect efficiency of the channel plates (about 70 %) are one reason. At the energy of incident positrons of about 1.1 keV, only 30 kcps are detected at the channel plate. About

Reproduced with permission of the copyright owner. Further reproduction prohibited without permission.

25 % of annihilation gamma rays are recorded. This reduces the count rate from 30 kcps to about 7 kcps. Further reduction to the value of 1.8 kcps can be explained by contribution of backscattered positrons to the counts at the channel plates and multiple counts in the channel plates due to scattering of the electrons in the system.

Table VI. The dependence of the count rate in the lifetime spectrometer on the energy of the implanted positrons. The data were collected for the sample made of HF-etched Si(111).

Positron energy (keV)	Peak count rate (cps)
1.1	1.8k
2.0	!.1k
3.0	660
4.0	520
28.0	130

3.5.1.6 Application to low-k dielectric films

3.5.1.6.1 Motivation

The switching speed of transistors in IC's depends on the *RC* time value of the circuit. The value can be reduced through a decrease of the intrinsic capacitance. The capacitance is proportional to the dielectric constant k of the insulator placed between the electrodes of the capacitor. Therefore, the industry of semiconductors is actively seeking for materials of low dielectric constant. For silicon dioxide, currently used in IC's, k is about 4.0. For vacuum and, approximately, for air, k is equal 1 and this is the lower limit

Reproduced with permission of the copyright owner. Further reproduction prohibited without permission.

of the search. The dielectric constant can be reduced by modifying the internal structure of the molecules or by incorporating large pores into the material. The first method was investigated by *Lim et al.*[90] Fluorine doping of SiO_2 allowed to reduce k to the value of 2.6. Examples of the later method include porous silicon and foamed methylsilsesquioxane (MSSQ). Foamed MSSQ is actively researched by IBM. MSSQ is a family of siloxanes $(XSiO_{1.5})_n$ with n = 4, 6, 8, ... X denotes the terminal substituent, methyl in the case of MSSQ. The compounds form highly symmetric cage-like structures. An example, for n = 10, is shown in Figure 40. The low value of the dielectric constant is a consequence of large open volumes created inside the cage-like structures. The results of the investigation of these materials with positron lifetime technique are presented next.

Figure 40. Example of the molecular structure of methylsilsequioxane. From Schneider.[91]

The films were about .6 μm thick, which necessitated the use of variable-energy positrons. Common bulk spectrometers would not be able to resolve defects in such shallow films.

Reproduced with permission of the copyright owner. Further reproduction prohibited without permission.

3.5.1.6.2 Characterization

Two MSSQ samples from IBM were investigated. The samples were identical except only one contained pores (sample 3C). The details of the foaming process have not been published and are a proprietary information of IBM. As expected, the dielectric constant of the sample containing pores was lower. It was found 2.05 and 3.63 for samples 3C and 3A, respectively.

The lifetime measurements of the two samples were done using the variable-energy positron lifetime spectrometer described in section 3.5.1. All measurements were done at room temperature and in dark - to eliminate the possibility of light excitation of the defects. The lifetime spectra are shown in Figure 41. Both spectra contain a short-lived (a few hundred ps) and a medium-long (several ns) component. In addition, in sample 3C, a very long-lived (tens of ns) component can be identified. The spectrum does not contain information on the events of positrons living longer than about 34 ns. Nevertheless, the almost-flat tail in the spectrum indicates the existence of a very long-lived component. This is not an artifact of the spectrometer. The counts in the tail of the spectrum of sample 3C are far above the background. The level of background can be extrapolated from the left side of the main peak. This level is the same for both samples and is 3×10^{-4} units. Both spectra suffer from small influence of undesired counts from backscattered positrons. The effect unveils as a broad hump between 4 ns and 10 ns. In spite of the presence of the hump, a medium-lived decay component can be identified. Without the medium-lived decay, the hump would be much lower. The magnitude of the hump can be estimated from the spectra of other samples, e.g. Si-based (not shown).

Reproduced with permission of the copyright owner. Further reproduction prohibited without permission.

The spectra of both samples were fitted using equations 24 through 26. The presence of the hump between 4 and 10 ns caused instability of the fitting algorithm.

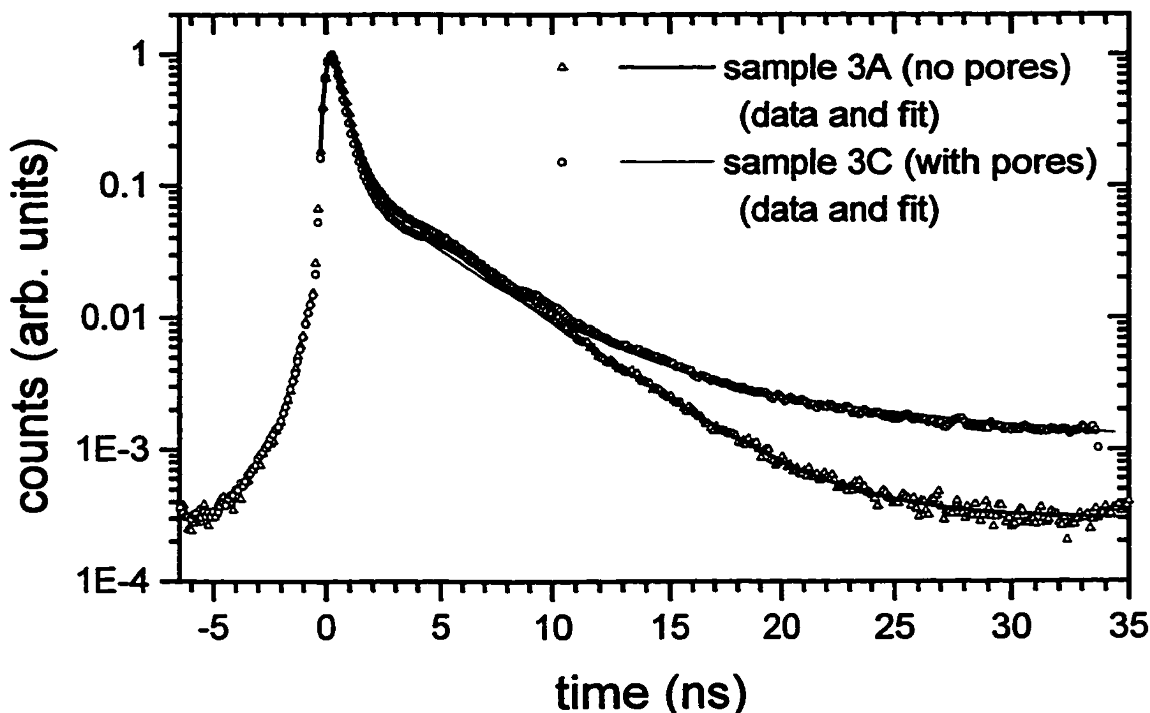

Figure 41. Experimental (symbols) and fitted (lines) spectra of methylsilsequioxane samples. The spectra of both samples contain 3.5 ns decay component in addition to about 0.4 ns decay. A 24 ns decay is found only in the foamed sample (3C).

Therefore, the "best fits" were obtained through a manual adjustment of the parameters. Visual inspection and monitoring of χ^2 were employed to get the best fit. The fitted spectra are shown in Figure 41. The best-fit parameters are listed in Table VII. The error bars were estimated by monitoring the visual quality of the fit. The fitted parameter was being changed until a noticeable worsening of the fit quality was observed. The critical value of the parameter determined the corresponding error bar. The instrumental

Reproduced with permission of the copyright owner. Further reproduction prohibited without permission.

resolution, i.e. a sum of two asymmetric Gaussians, was assumed identical to the one found in Si-based samples, see section 3.5.1.5.2. The spectrum of sample 3A was fitted as a sum of two exponential decays and three decays for sample 3C. The value of the longer lifetime found in sample 3A was fixed in the fit of the spectrum of sample 3C.

Table VII. Lifetime components found in low-k films. NN denotes not needed.

Sample	τ_1 **(ns)**	τ_2 **(ns)**	τ_3 **(ns)**	**f2**	**f3**
3A (no pores)	0.41(3)	3.5(4)	NN	0.42(4)	NN
3C (with pores)	0.39(3)	3.5	24(2)	0.32(4)	0.08(1)

The shortest lifetime, 0.41 ns and 0.39 ns for sample 3A and 3C, respectively, can be interpreted as due to the characteristic lifetime of the base material, i.e. MSSQ. This decay is believed to come from the annihilation of unbound positrons, i.e. not from Ps. This is because the reported values are below the upper limit of the annihilation of unbound positrons, about 500 ps. The lifetime of 3.5 ns is due to positronium formation in small voids. The radius of the voids can be estimated from equation 17 and is 0.65 nm. This decay is found in both samples. Therefore, it is concluded that voids of the average radius of 0.65 nm exist in both investigated MSSQ. The existence of two lifetime components has been observed in similar samples. Sun *et al* reported simultaneous observation of 1.5 ns and 2.25 – 3.0 ns lifetimes in poly-SSQs.[92] The longer lifetime was interpreted as due to positron annihilation between regions of SSQ cubes. Sample 3C contained another lifetime component (24 ns). The corresponding void radius is 1.4 nm.

Reproduced with permission of the copyright owner. Further reproduction prohibited without permission.

Equation 17 is believed to be applicable in the determination of the pore size. Nevertheless, the value of the parameter ΔR was fitted for the lifetimes shorter than 8 ns. ΔR equal 1.656 A might not be appropriate at longer lifetimes. Instead, experimentally found relation was used here.[93] Creation of the voids of the radius of 1.4 nm is attributed to the formation of the pores responsible for the reduction of the dielectric constant.

The observation of Ps formation in sample 3C is consistent with the analysis of Ps fraction based on energy distribution of annihilation gamma rays.[94] In this technique, formation of Ps can be identified from the extended analysis of the energy spectrum. Ortho-Ps annihilates into three gamma rays. Unlike in the case of two-gamma decay, the energy of the three quanta varies continuously from zero to 511 keV. Detection of gamma at energies within this range denotes formation of ortho-Ps. Quantitative information pertaining the fraction of Ps can be obtained but it requires performing a cumbersome calibration procedure.[95] No quantitative information was obtained with this technique. Nevertheless, sample 3C revealed measurable amount of Ps formation. No measurable amount of Ps formation was detected in sample 3A using the extended analysis of the energy distribution of annihilation radiation. Therefore, observation of 24 ns decay can be related to the detection of ortho-Ps with the analysis of the gamma-energy distribution.

The 3.5 ns decay was detected in the lifetime spectra of both samples. Apparently, it is inconsistent with the absence of Ps determined from the gamma-energy distribution. To explain this, one needs to consider Ps annihilation in more detail. Positronium in vacuum decays into two or three gamma rays. Ps trapped in a void also decays into two or three gamma, but the origin of the two-gamma decay may be two folds. It can be the

Reproduced with permission of the copyright owner. Further reproduction prohibited without permission.

consequence of the positron annihilation with an electron picked up from the edge of the void or with the electron bound in para-Ps. The smaller the size of the open volume, the less likely the three-gamma process is. This is because the overlap of the wave functions of the positron and the electron from the edge of the void increases. Consequently, the annihilation rate increases, too. When the annihilation rate (inverse of lifetime) is $(3.5\ ns)^{-1}$, the two-gamma decay dominates. In positronium detection technique based on the analysis of the distribution of gamma energy, the Ps fraction is calculated from the observed three-gamma decays. When few decays of this kind happen, the technique looses sensitivity. Therefore, Ps may form and not be detectable with this technique, i.e. for 3.5 ns decay.

Sample 3C turned out to be highly hygroscopic. The measurements were repeated 35 days later. The 24 ns decay disappeared completely and the spectrum of sample 3C was almost identical to the one of sample 3A (not shown). Annealing at 110 ^{0}C for 4 hours in air atmosphere did not restore the long-lived decay. Possibly, water reacted with MSSQ in a reaction called hydrolysis. In this kind of reaction, methyl termination of Si atoms of the cage-like molecule is replaced with oxygen bridges. The oxygen bridges cross-link Si atoms across the open volume, which would, otherwise, trap positronium. This scenario is very hypothetical and further investigation is advisable. Certainly, hygroscopic nature of the material is not desirable from technological point of view. It will require fast processing during manufacturing and sealing the material from air in the final product.

Reproduced with permission of the copyright owner. Further reproduction prohibited without permission.

3.5.1.7 Discussion

The measurements of low-k dielectric films demonstrate how powerful the new lifetime spectrometer is. Possible applications are as follows. The spectrometer can be used to further investigate low-k dielectrics. Defect analysis in compound semiconductors is possible. The spectrometer could be used to analyze the physics of electromigration known to be responsible for failures of interconnections in ICs.

The background caused by backscattered positrons may be reduced by incorporation of a double-pulse rejection system described in section 3.5.1.4.

3.5.2 Design #2, magnetic-dipole trap

3.5.2.1 Description of the system

The schematic of the system is shown in Figure 42. A uniform magnetic field guides positrons from the source to the shown system. The positrons enter the sample at the 45 deg angle. The secondary electrons emitted upon positron entrance into the sample are accelerated in an electric field to the energy of about 600 eV. Speeding up the electrons reduces the spread of their time of flight caused by the broad distribution of the initial energy. The electrons are collected in a micro-channel plates detector. To compensate the angular divergence of the emitted secondaries, guiding magnetic field is applied. The guiding field is formed by two permanent magnets: one behind the sample and the other behind the micro-channel plates. A BaF_2 scintillator connected to a PMT is placed along the "x" axis (not shown). This detector collects annihilation gamma rays.

Reproduced with permission of the copyright owner. Further reproduction prohibited without permission.

3.5.2.2 Testing

The system was pre-tuned with electrons instead of positrons. The current of electrons was measured with a micro-amp meter. Next, a micro-channel plates detector

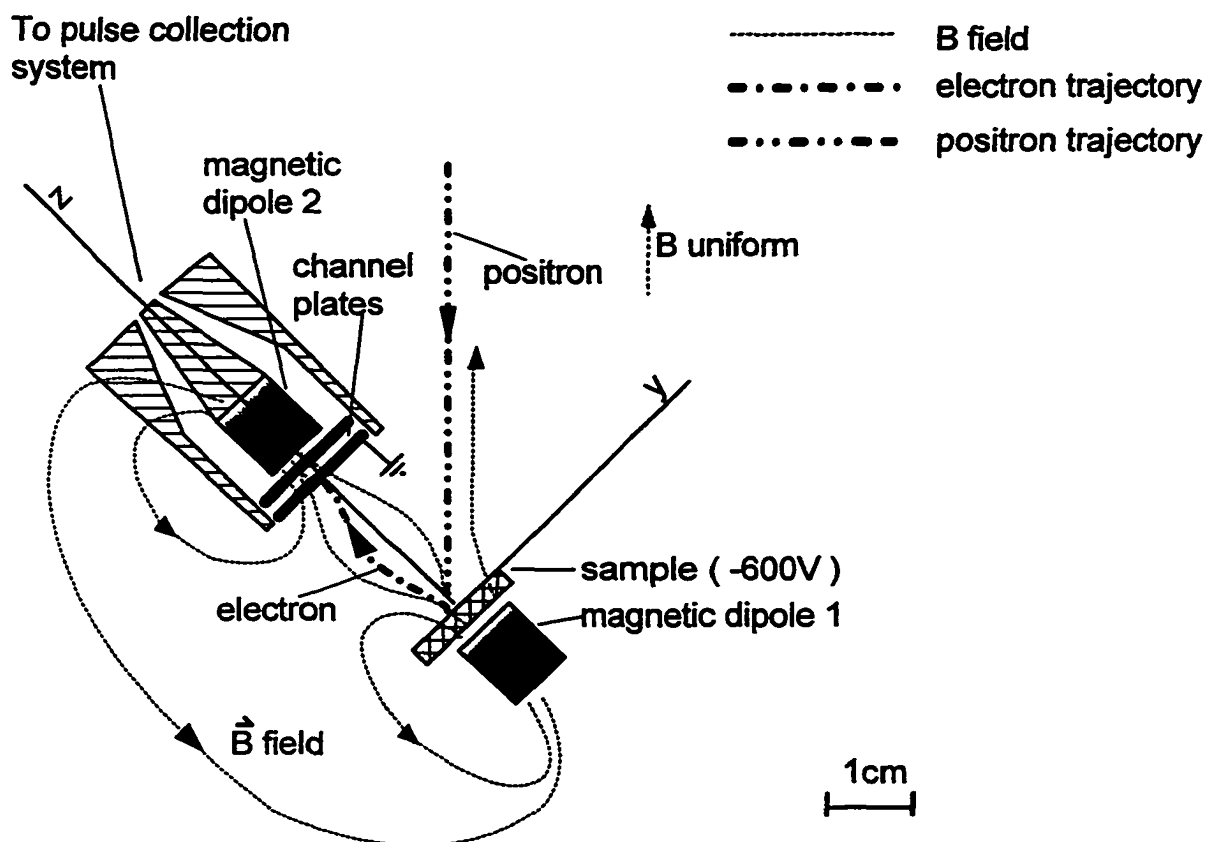

Figure 42. The schematic diagram of the magnetic-dipole-trap positron lifetime spectrometer. The positrons are injected into the sample placed in the strong fields of the permanent magnets. The magnetic fields guide the secondary electrons, which start the lifetime clock.

was placed instead of the sample. This detector was used to detect the entrance of a positron into the sample (which in this case was the micro-channel plates detector itself). Efficiency of micro-channel plates to positrons is much higher than the efficiency of a remotely located scintillator / PMT to gamma radiation. Therefore, a much higher count

Reproduced with permission of the copyright owner. Further reproduction prohibited without permission.

rate was observed which facilitated more accurate tuning. Eventually, a high-purity Si sample was installed and the lifetime of positrons in Si was measured.

Several problems were encountered during testing. Originally, a mesh electrode was placed about 2.5 mm from the sample (not shown in Figure 42). This mesh was intended to allow for faster acceleration of the secondaries to the energy of 600 eV. Faster acceleration was intended to reduce the smearing of the time of flight of the secondaries caused by the spread of the initial energies. Unfortunately, the secondary electrons could not reach the detector. The presence of the mesh created high electric fields. Together with the non-uniform magnetic field of the magnets, not parallel to the electric field, it created strong E×B shifts. These shifts prevented the secondaries from approaching the detector.

A small magnet behind the sample was replaced with a magnet of the same size as the one behind the micro-channel plates (shown in Figure 42). This reduced the reflection of secondaries in the strong field of the other magnet.

In order to improve the efficiency of the gamma collection, the scintillator should be placed as close to the sample as possible. Unfortunately, the presence of the detector well made of steel distorts the electric fields in the system. To prevent the distortion, a resistive plate made of silicon wafer was placed between the scintillator and the sample. Voltage was applied across the resistive plate in order to fix the boundary potential at required values.

The best lifetime spectrum obtained with this system is shown in Figure 43. The spectrum was collected for positron implantation energy of 10 keV. FWHM of the lifetime peak was found 890 ps. This number contains the contribution of the positron

Reproduced with permission of the copyright owner. Further reproduction prohibited without permission.

decay in Si (220 ps). The ratio of peak to background was about 50. The background on the lifetime edge is believed to be due to backscattered positrons. The hump on the non-

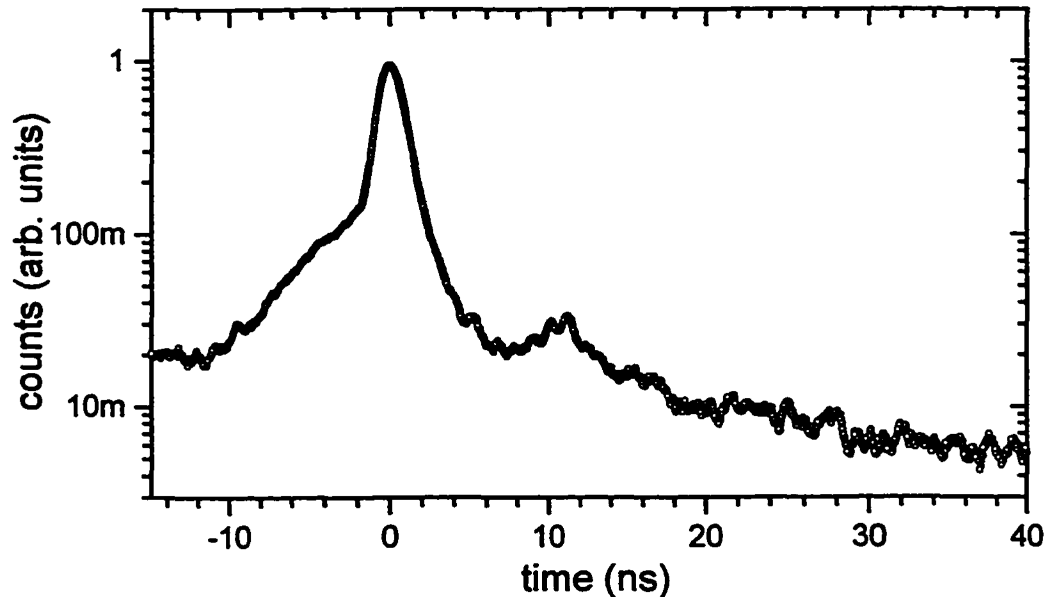

Figure 43. The best lifetime spectrum obtained with the magnetic-dipole trap setup. The spectrum was collected for 10 keV positrons injected into high-purity Si. The timing resolution of 890 ps at FWHM was obtained.

lifetime edge is believed to originate from secondary electrons backscattered from the micro-channel plates and returning there.

The performance of the lifetime spectrometer was found not satisfactory. At lower energies of positrons, the ratio of peak to background was even lower. In addition, the spot of the positron beam at the sample was large (about 3 cm in diameter). The main problem of the system was in proper guiding of the primary positrons to the sample. The system was optimized for the fast transport of secondaries to prevent degradation of the timing resolution. Unfortunately, few positrons were able to penetrate the strong field of

Reproduced with permission of the copyright owner. Further reproduction prohibited without permission.

the permanent magnets and reach the sample. In addition, only a small fraction of secondaries was reaching the detector. Many of them would follow the lines of the uniform magnetic field and fly towards the positron source.

The testing of the system was abandoned. Although the system turned out not to be successful, I gained valuable experience in the construction of charged-particle systems. This experience allowed me to redesign the system. The redesigned system, see section 3.5.1, turned out to be a very competitive lifetime spectrometer.

Reproduced with permission of the copyright owner. Further reproduction prohibited without permission.

4 Summary

In this research, measurements of the positron lifetime and of the Doppler broadening of the positron annihilation line were conducted to investigate selected defects in solids. The core electron contribution to the annihilation line was examined in detail. For the first time, the analysis of the line shape depending on the momentum distribution of the core-electrons was applied to foreign-atom decorated open-volume defects. The complex of Sb atom tied to a Si vacancy was identified as the acceptor-behaving defect causing the saturation of doping in LT-MBE Si doped with Sb. A technologically important DX center in Si-doped AlGaAs was examined. The ground state of the defect was for the first time directly shown to consist of a small vacancy tied to one Si and one As atom.

A prototype of a variable-energy positron lifetime spectrometer was designed and tested. The timing resolution of 470 ps at FWHM was obtained. The new spectrometer was used in the analysis of a low-dielectric-constant material intended to replace silicon dioxide in the integrated circuits of the next generation. A foamed material was shown to contain dielectric-constant reducing voids of the radius of 1.4 nm.

Reproduced with permission of the copyright owner. Further reproduction prohibited without permission.

Bibliography

[1] Cs. Szeles, P. Asoka-Kumar, K. G. Lynn, H,-J. Gossman, F. C. Unterwald and T. Bone, Appl. Phys. Lett. **66**, 2855 (1995).

[2] T. C. Leung, P. Asoka-Kumar, B. Nielsen and K. G. Lynn, J. Appl. Phys. **73**, 168 (1993).

[3] P. J. Schultz and K. G. Lynn, Rev. Mod. Phys. **60**, 701 (1988).

[4] K. G. Lynn, J. E. Dickman, W. L. Brown, M. F. Robbins and E. Bonderup, Phys. Rev. B **20**, 3566 (1979).

[5] M. Alatalo, H. Kauppinen, K. Saarinen, M. J. Puska, J. Makinen, P. Hautojarvi and R. M. Nieminen, Phys. Rev. B **51**, 4176 (1995).

[6] J. Kuriplach, A. L. Morales, C. Dauwe, D. Segers and M. Sob, Phys. Rev. B **58**, 10475 (1998).

[7] M. Hakala, M. J. Puska and R. M. Nieminen, Phys. Rev. B **57**, 7621 (1998).

[8] S. Szpala, P. Asoka-Kumar, B. Nielsen, J. P. Peng, S. Hayakawa, K. G. Lynn and H.-J. Gossmann, Phys. Rev. B **54**, 4722 (1996).

[9] J. R. MacDonald, K. G. Lynn, R. A. Boie and M. F. Robbins, Nucl. Inst. Meth. **153**, 189 (1978).

[10] P. Asoka-Kumar, M. Alatalo, V. J. Ghosh, A. C. Kruseman, B. Nielsen and K. G. Lynn, Phys. Rev. Lett. **77**, 2097 (1996).

[11] U. Myler and P. J. Simpson, Phys. Rev. B **56**, 14303 (1997).

[12] M. Alatalo, B. Barbiellini, M. Hakala, H. Kauppinen, T. Korhonen, M. Puska, K. Saarinen, P. Hautojarvi and R. M. Nieminen, Phys. Rev. B **54**, 2397 (1996).

[13] S. Dannefaer, W. Puff and D. Kerr, Phys. Rev. B **55**, 2182 (1997).

[14] A. P. Mills, Jr. and R. J. Wilson, Phys. Rev. A **26**, 490 (1982).

[15] V. J. Ghosh, D. O. Welch and K. G. Lynn, Proceedings of the 5th international workshop on slow positron beam techniques for solids and surfaces, ed. by E. H. Ottewitte and A. H. Weiss (AIP, NY, 1993) p37.

Reproduced with permission of the copyright owner. Further reproduction prohibited without permission.

[16] A. van Veen, H. Schut, J. de Vries, R. A. Hakvoort and M. R. Ijpma in Positron Beams for Solids and Surfaces, edited by P. J. Schultz, G. R. Massoumi and P. Simpson, AIP Conf. Proc. No 218 (American Institute of Physics, New York, 1990), p. 171.

[17] K. G. Lynn and A. N. Goland, Solid State Commun. **18**, 1549 (1976).

[18] P. Asoka-Kumar, K. G. Lynn and D. O. Welch, J. Appl. Phys. **76**, 4935 (1994).

[19] Y. C. Jean, K. G. Lynn and J. E. Dickman, Phys. Rev. B **21**, 2655 (1980).

[20] Y. Kong and K. G. Lynn, Nucl. Inst. Meth. Phys. Res. Sec. A **302**, 145 (1991).

[21] D. T. Britton, P. Bentvelsen, J. De Vries and A. van Veen, Nucl. Instr. Meth. Phys. Res. Sect. A **273**, 343 (1988).

[22] O. W. Holland, M. K. El-Ghor and C. W. White, Appl. Phys. Lett. **53**, 1636 (1988).

[23] B. Nielsen, O. W. Holland, T. C. Leung and K. G. Lynn, J. Appl. Phys. **74**, 1636 (1993).

[24] D. J. Eaglesham, H. –J. Gossmann and M. Cerullo, Phys. Rev. Lett. **65**, 1227 (1990).

[25] D. D. Perovic, G. C. Weatherly, P. J. Simpson, P. J. Schultz, T. E. Jackman, G. C. Aers, J. –P. Noel and D. C. Houghton, Phys. Rev. B **43**, 14257 (1991).

[26] Alfa Aesar, A Johnson Mathey Company, 30 Bond St., Ward Hill, MA 01835, USA.

[27] A. Weiss, R. Mayer, M. Jibaly, C. Lei, D. Mehl, K. G. Lynn, Phys. Rev. Lett. **61**, 2245 (1988).

[28] W. Kern and D. A. Puotinen, RCA Rev. **31**, 187 (1970).

[29] D. J. Monk and D. S. Soane, J. Electrochem. Soc. **140**, 2339 (1993).

[30] M. Nivano, J. Kageyama, K. Kurita, K. Kinashi, I. Takahashi and M. Miyamoto, J. Appl. Phys. **76**, 2157 (1994).

[31] M. Fujinami and N. B. Chilton, Appl. Phys. Lett. **63**, 3458 (1993).

[32] The wafers manufactured by Wacker were distributed by Si-Tech, Inc., 218 Boston St., Suite 105, Topsfield, MA 01983, USA.

[33] V. Avalos and S. Dannefaer, Phys. Rev. B **58**, 1331 (1998).

Reproduced with permission of the copyright owner. Further reproduction prohibited without permission.

[34] F. A. Trumbore, Bell Syst. Tech. J. **39**, 205 (1960).

[35] H.-J. Gossmann, F. C. Unterwald and H. S. Luftman, J. Appl. Phys. **73**, 8293 (1993).

[36] W. Walukiewicz, Phys. Rev. **B** 50, 5221 (1994).

[37] D. L. Adler, J. D. Chadi, M. A. Marcus, H.-J. Gossmann and P. H. Citrin, Bull. Am. Phys. Soc. **40**, 396 (1995).

[38] A. Kawasuso, M. Hasegawa, M, Suezawa, S. Yamaguchi and K. Sumino, Jpn. J. Appl. Phys. **34**, 2197 (1995).

[39] P. Mascher, S. Dannefaer and D. Kerr, Phys. Rev. B **17**, 11764 (1989).

[40] H. H. Radamson, M. R. Sardela, Jr. L. Hultman and G. V. Hansson, J. Appl. Phys. **76**, 763 (1994).

[41] N. –E. Lee and J. E. Greene, Appl. Phys. Lett. **67**, 2459 (1995).

[42] D. J. Chadi and K. J. Chang, Phys. Rev. B **39**, 10063 (1989).

[43] P. M. Mooney and T. N. Theis, Comments Cond. Mat. Phys. 1992, Vol. 16, No. 3, p167.

[44] P. M. Mooney, J. Appl. Phys. **67** (3), R1 (1990).

[45] R. Krause-Rehberg, Th. Drost, A. Polity, G. Roos, G. Pensl, D. Volm, B. K. Meyer, G. Bischopink and K. W. Bemz, Phys. Rev. B **48**, 11723 (1993).

[46] J. Makinen, T. Laine, K. Saarinen, P. Hautojarvi, C. Corbel, V. M. Airaksinen and P. Gibart, Phys. Rev. Lett. **71**, 3154 (1993).

[47] P. E. Mijnarends, Physica (Utrecht) **63**, 235 (1973).

[48] S. Berko, in Positron Solid State Physics, Proceedings of the International School of Physics "Enrico Fermi", Course LXXXIII, Varenna 1981, ed. by W. Brandt and A. Dupasquier, North Holland, Amsterdam, 1983, p64.

[49] R. N. West, Adv. Phys. **22**, 263 (1973).

[50] W. E. Frieze, K. G. Lynn and D. O. Welch, Phys. Rev. B **31**, 15 (1985).

[51] M. J. Puska, C. Corbel and R. M. Nieminen, Phys. Rev. B **41**, 9980 (1990).

Reproduced with permission of the copyright owner. Further reproduction prohibited without permission.

[52] A. Seeger and F. Banhart, Phys. Stat. Sol. A **102**, 171 (1987).

[53] K. G. Lynn and D. O. Welch, Phys. Rev. B **22**, 99 (1980).

[54] R. Suzuki, T. Mikado, H. Ohgaki, M. Chiwaki, T. Yamazaki and Y. Kobayashi, Phys. Rev. B **49**, 17484 (1994).

[55] H. Nakanishi, S. J. Wang and Y. C. Jean, "Positron Annihilation Studies of Fluids" ed. by S. C. Sharma, Word Science 1988, p.292.

[56] Y. Kong, Ph.D. dissertation, The City University of New York, 1991.

[57] C. M. Lededrer, J. M. Hollander, I. Perlman, Table of Isotopes, Sixth Edition, John Wiley & Sons, Inc., New York, London, Sydney 1967.

[58] A. Vahanen and K. Rytsola, Positron Solid State Physics, Proceedings of the International School of Physics "Enrico Fermi", Course LXXXIII, Varenna 1981, ed. by W. Brandt and A. Dupasquier, North Holland, Amsterdam, 1983.

[59] W. Weiler, H. E. Schaefer and K. Maier, Positron Annihilation, P. G. Coleman, S. C. Sharma and L. M. Diana, eds., North Holland 1982, p865.

[60] D. W. Gidley, K. A. Marko and A. Rich, Phys. Rev. Lett., **36**, 395 (1976).

[61] K. G. Lynn, W. E. Frieze and P. J. Schultz, Phys. Rev. Lett. **52**, 1137 (1984).

[62] A. P. Mills, Jr., Appl. Phys. Lett. **22**, 273 (1980).

[63] D. Schodlbauer, P. Sperr, G. Koegel and W. Triftshaeuser, Positron Annihilation, ed. by P. C. Jain, R. M. Singru and K. P. Gopinathan, Worls Scientific Publ. Co., Singapore 1985, p.957.

[64] R. Suzuki, Y. Kobayashi, T. Mikado, H. Ohgaki, M. Chiwaki, T. Yamazaki and T. Tomimasu, Mat. Sci. Forum **105-110**, 1993 (1992).

[65] A. Zecca, R. S. Brusa, M. P. Duarte-Naia, G. P. Karwasz, J. Paridaens, A. Piazza, G. Kogel, P. Sperr, D. T. Britton, K. Uhlmann, P. Willutzki and W. Triftshaeuser, Europhys. Lett. **29**, 617 (1995).

[66] J. I. Goldstein, D. E. Newburg, P. Echlin, D. C. Joy, C. Fiori and E. Lifshin, Scanning electron microscopy and x-ray microanalysis, a text for biologists, material scientists and geologists, Plenum Press, New York and London, p.53.

Reproduced with permission of the copyright owner. Further reproduction prohibited without permission.

[67] E. M. Baroody, Phys. Rev. **78**, 780 (1950).

[68] K. Ohya, Jpn. J. Appl. Phys. **33**, 4735 (1994).

[69] A. J. Dekker, Electrical engineering materials, Englewood Cliffs, N.J. Prentice-Hall (1959).

[70] E. Jung, R. Venkataraman, S. Starnes and A. H. Weiss, Mat. Sci. Forum **255-257**, 708 (1997).

[71] G. R. Massoumi, N. Hozhabri, W. N. Lennard and P. J. Schultz, Phys. Rev. B **44**, 3486 (1991).

[72] J. A. Baker and P. Coleman, J. Phys. C: Solid State Phys. **21**, L875 (1988).

[73] H. Bishop, in Proceedings of the Fourth International Congress on X-ray Optics and Microanalysis, ed. By R. Casataing, P. Deschamps and J. Philibert (Hermannn, Paris, 1966), p.153.

[74] A. P. Mills, Jr., Appl. Phys. Lett. **37**, 667 (1980).

[75] D. A. Dahl, Simion 3D, version 6.0 users manual, Idaho National Engineering Laboratory (1995).

[76] General Electric Company, Silicone Products Division, Waterford, NY 12188.

[77] Hamamatsu Photonics K. K., Electron Tube Center, 314-5, Shimokanzo, Toyooka-village, Ivata-gun, Shizuoka-ken, 438-01, Japan.

[78] M. Laval, M. Moszynski, R. Allemand, E. Cormoreche, P. Guinet, R. Odru and J. Vacher, Nucl. Instr. Meth. **206**, 169 (1983).

[79] M. Galanti, R. Gott and J. F. Renaud, Rev. Sci. Instr. **42**, 1818 (1971).

[80] EG&G Ortec, 100 Midland Road, Oak Ridge, TN 37831, USA.

[81] E. H. Darlington and V. E. Cosslett, J. Phys. D: Appl. Phys. **5**, 1969 (1972).

[82] Motorola, Inc., Motorola Literature Distribution, P.O. Box 20912, Phonix, AZ 85036, USA.

[83] Y. Itoh, H. Murakami, H. Takeno, S. Ushiro and T. Takenaka, Mat. Sci. Forum **255-257**, 545 (1997).

Reproduced with permission of the copyright owner. Further reproduction prohibited without permission.

---

[84] A. Kawasuso, M. Hasegawa, M. Suezawa, S. Yamaguchi and K. Sumini, Mat. Sci. Forum **175-178**, 423 (1995).

[85] S. Makinen and H. Rajainmaki, Phys. Rev. B **42**, 11166 (1990).

[86] M. Puska, C. Corbel, Phys. Rev. B **38**, 9874 (1988).

[87] Origin Professional v 5.0, Microcal Software, Inc., Northampton, MA.

[88] G. Collins, lifetime fitting code, Washington State University, Physics Dept., Pullman WA 99164, unpublished.

[89] A. Seeger and F. Banhart, Helvetica Physica Acta **63**, 403 (1990).

[90] S. W. Lim, Y. Shimogaki, Y. Nakano, K. Tada and H. Komiyama, Jpn. J. Appl. Phys. **35**, 1468 (1996).

[91] R. Schneider, http://www.uni-bielefeld.de/chemie/tc/Ralph/abstract_e.html

[92] J. Sun, T. L. Dull, A. F. Yee, W. E. Freeze, D. W. Gidley, C. Nguyen and D. Y. Yoon, March Meeting of the American Physical Society, 1999, session VC23.10.

[93] Y. Wakabayshi, H. –L. Li, Y. Ujihara, K. Kamitani, H. Inoue and A. Makishima, Mat. Sci. Forum **255-257**, 357 (1997).

[94] M. Petkov, M. Weber, K. G. Lynn, K. Rodbell, unpublished.

[95] K. G. Lynn, Positron Solid State Physics, Proceedings of the International School of Physics "Enrico Fermi", Course LXXXIII, Varenna 1981, ed. by W. Brandt and A. Dupasquier, North Holland, Amsterdam, 1983.

Reproduced with permission of the copyright owner. Further reproduction prohibited without permission.

IMAGE EVALUATION TEST TARGET (QA-3)

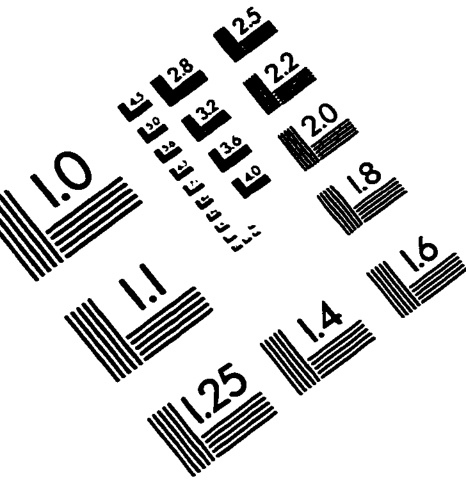
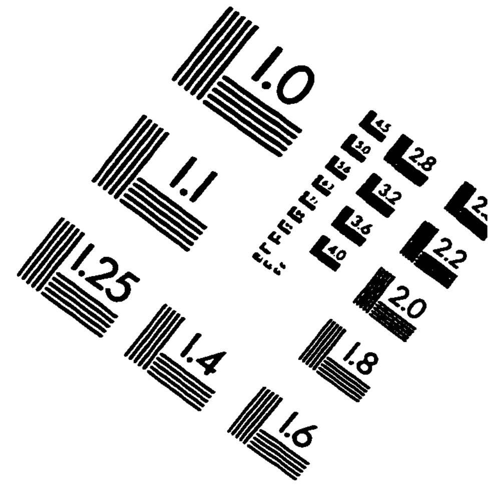
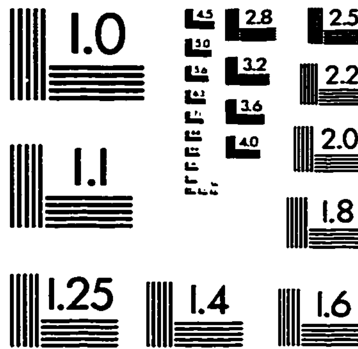
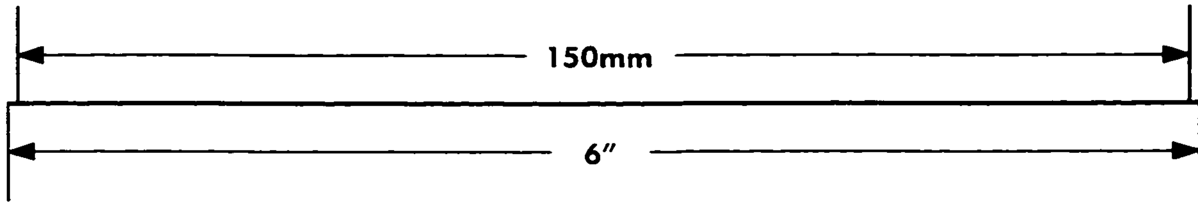

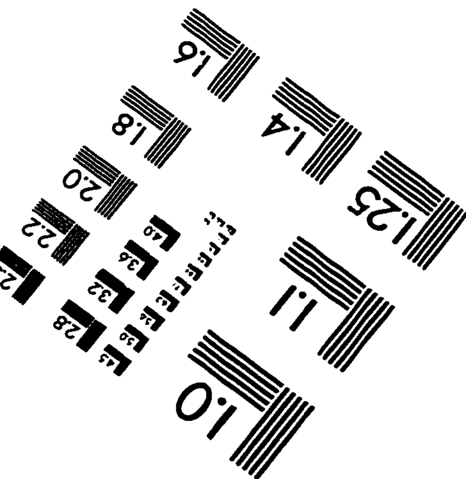

APPLIED IMAGE, Inc
1653 East Main Street
Rochester, NY 14609 USA
Phone: 716/482-0300
Fax: 716/288-5989

© 1993, Applied Image, Inc., All Rights Reserved

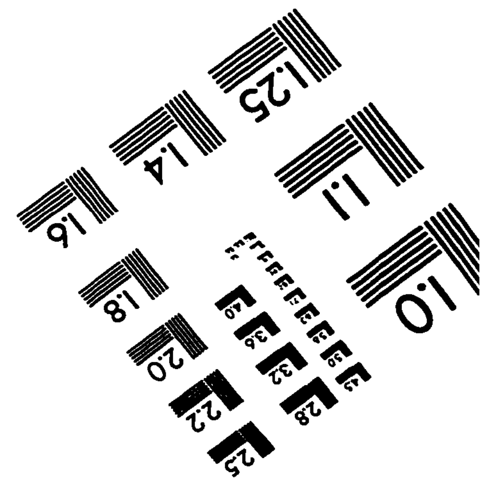

Reproduced with permission of the copyright owner. Further reproduction prohibited without permission.